AERODYNAMICS OF FLAPPING FLIGHT INTERACTING WITH ENVIRONMENTS

January 2014

MASATERU MAEDA

Graduate School of Engineering

CHIBA UNIVERSITY

（千葉大学審査学位論文）

AERODYNAMICS OF FLAPPING FLIGHT INTERACTING WITH ENVIRONMENTS

January 2014

MASATERU MAEDA

Graduate School of Engineering

CHIBA UNIVERSITY

Abstract

In previous studies of flapping flight aerodynamics, the interaction between the surrounding environment such as gust response or takeoff/landing, was not usually considered. Also, the knowledge on the wing deformation during flapping, which has recently been attracting attention for its potential benefit in the efficient generation of aerodynamic forces, is far from complete. In the present study, the integrated flapping flight simulator is utilized for elucidating the aerodynamic force generation mechanisms in such complex situations.

First, a rigid body dynamics (RBD) solver with six degrees-of-freedom (6 DoF) was developed. By the loose coupling of the solver with an existing computational fluid dynamics (CFD) solver for flapping flight, it can now be possible to see the position or attitude changes in response to the perturbation, or to achieve a controlled flight with a controller. A newly-proposed stabilization mechanism named flapping counter torque (FCT) was tested as an example, showed considerable coupling between the DoF. Secondly, to examine the effect of ground on the flapping flight, a fruit fly hovering was tested. It was shown the body is effectively on the high pressure air cushion on the ground, which is originally generated by the downwash due to flapping, and body is earning more than 7% of the total vertical force. Thirdly, the influence of ground and leg thrust in addition to the aerodynamic forces on the takeoff of a butterfly was investigated with the aid of three high speed cameras to the RBD & CFD solvers. As a result, it was understood that the leg thrust force has the largest impact, seconded by aerodynamic forces, whereas the ground has almost no effect in the specific case of the escape, quick takeoff. Finally, the wing deformation of a hummingbird during hovering in a natural situation was explored. The four high speed video cameras and the following examination showed for the first time that the hummingbird wings is indeed compliant at least as the same as or more than the insects wings. The numerical simulation to compare the performance of real deforming wing and an ideal flat-plate wing revealed that the real wing outperforms both in the magnitude of the aerodynamic force and the force-to-power ratio.

It can be concluded that the flyers in the natural world perform flapping flights efficiently and robustly, by making the most of the interactions between the surrounding environments.

Acknowledgements

My first and foremost thanks go to my advisor Professor Hao Liu. I would not have been able to finish my Masters and PhD studies without his direction and assistance in the research, as well as financial support. I owe so much to the professor. If it were not him, I would have never had given the freehand in the selection of research topic. I am so grateful that I finally had the change to pursue what Ive always wanted to do: aerodynamics of bird flight.

I sincerely thank Prof. Masahiro Takei, Prof. Kazuo Maeno, Prof. Ning Hu, and Prof. Ken-ichi Tsubota for serving as the committee members.

My research works have been true collaborations between many people.

I would like to express sincere thanks to the following people in the Liu laboratory. Dr. Hikaru Aono for his tremendous amount of legacy works. Nothing would have even started without his earlier works. Dr. Gao Na for her encouragement of and the direct support in the development of the Cartesian background grid with the moving flyer, as well as Chinese support in Shanghai and Singapore. Naoshi Nishihasi helped me in developing the Cartesian grid. Specifically, his assistance in the boundary conditions was critical in the development of ground effect simulation. Kazuhiro Yanaoka pioneered the butterfly takeoff simulation, and Shuhei Ozawa assisted me a lot in the butterfly takeoff. Yuuichi Nakatzato and Ren Tamura trail blazed the hummingbird simulation. Dr. Hiroto Tanaka supported (and is supporting) me a lot in the hummingbird project from experiment design to the manuscripts. Ryusuke Noda helped me in numerous things from everyday discussions to butterfly experiments, to software and hardware support. Gen Li helped (and will help) me in the improvement of the interpolation part of the source code. Takashi Fujiwara for his support in maintaining both Linux OS and workstations (which really takes time and should not be dispensed, indeed!). The colleagues of my ME years (Yusuke Osumi, Takashi Moriyama, and esp. Satoru Nagasawa) made my life full of fun. Finally but most importantly, Dr. Toshiyuki Nakata for just everything. From everyday research discussion to parallelizing the code; to generating the deforming wing mesh; and even to seeking for yoghurt (which is inevitable ingredients to me) with me in the -20 deg C Salt Lake City. Without his generous and continuous support, and especially his optimistic encouragements and attitude of enjoying the research, I would have fairly likely been unable to finish my PhD study.

I would like to acknowledge the following people outside the CU. First of all, Prof. Toshio Tagawa in TMU and the colleagues in Tagawa Lab at the time I spent my BE year there. They taught me the fun of CFD and fun of research in the lab. Without them, I am not here today. Prof. Ulrike Mller in Fresno State gave me several important lessons in the designing the presentation slides and research article manuscript when I was still in the early stage of the research carrier, which turned out to be quite useful later (She also gave me a nice umbrella when she left Japan, which helped me a lot, too). Prof. Yoshinobu Inada in Tokai Univ. gave me the opportunity of the first collaboration. The aeroacoustics is probably one of the most attractive issues for the public when I tell them Im working on insect flight. Prof. Makoto Iima in Hiroshima Univ. kindly invited me to a workshop where I received a huge stimulation from the scientists mainly from math or physics. Tony Horowitz, a retired mathematician in the US, kindly proofread one of my early English manuscripts and greatly helped improving my English skill. Joongkwan Kim in KAIST contacted me by finding my blog posts on biomechanics of flight, and by then let me know of their great works in stability & control of UAS, and encouraged our research works. Most recently, I got acquainted with Dr. Dmitry Kolomenskiy and he gave me a critical comment to my manuscript. I truly appreciate his help when I was really in need.

The high speed video recording of the hummingbird was the cooperative research between Chiba University and Tama Zoological Park. I thank Kuniei Tabata, Chieko Fujiwara, and other staffs in the Tama Zoological Park, and Yusuke Suzuki from Photron Limited, Japan for their support in video recordings. It was a very happy experience collaborating with the people who are outside of the academic but expressing real interests into the biomechanics of flight, or science in general.

Finally I thank my family for their continuous supports. Since when I was young, it has been felt quite natural for me to do the scientific research as a lifework, which maybe owing partly or mostly to my father Prof. Junji Maeda. It maybe that something started when he told me how to read the quadratic function.

This work was supported by the Grant-in-Aid for Scientific Research of No. 21360078 and 18100002; by the Grant-in-Aid for Scientific Research on Innovative Areas of No. 24120007, JSPS, Japan; and by the several Chiba University Research Support Programs during 2009-2013.

Contents

List of Figures

List of Tables

Chapter 1

General introduction

Similarly in the other research areas, numerical simulation has advantages and disadvantages as a tool of investigation of flapping flight. One of the most prominent features of using computational fluid dynamics (CFD) in flapping flight is the acquisition of the three-dimensional flow fields, from which one can directly obtain the aerodynamic forces and torques without any noises which usually contaminate the measured values in (physical) experiments. In experiments, obtaining the three-dimensional and/or time-resolved flow structure with particle image velocimetry (PIV) or other methods is still not quite easy, although there are several attempts (Liu et al., 2013, also see Bomphrey, 2011 for review). On the other hand, CFD strongly depends on the boundary conditions, i.e. wing kinematics, wing shape, etc.

The first three-dimensional CFD study was published in fifteen years ago (Liu et al., 1998). Since then, although there have been numbers studies using two-dimensional numerical simulation with either Naveir-Stokes or quasi-steady blade element methods, the number of researchers in 3D CFD has not been increased that much, probably partly due to the difficulties accompanied with treating a complex three-dimensional wing kinematics. Therefore, the flight conditions studied so far are mainly restricted to merely two: hovering or forward flight. The former includes hawkmoth (Liu et al., 1998; Aono et al., 2009; Nakata et al., 2011; Zheng et al., 2013*a*), fruit fly (Sun and Tang, 2002*b*,*a*; Ramamurti and Sandberg, 2007; Aono et al., 2008), honeybee (Liu and Aono, 2009), dragonfly (Sun and Lan, 2004; Young et al., 2008; Hamamoto et al., 2013), or thrips (Liu and Aono, 2009); the latter includes desert locust (Young et al., 2009), butterfly (Zheng et al., 2013*b*), dragonfly (Wang and Sun, 2005), or beetle (Le et al., 2013), among others. Most of these studies are tethered flight, i. e. no whole-body motion included. Also, most of them does not consider wing deformation or wing camber, rather, the wings have usually been treated as flat, rigid, non-deforming plate (although some of the aforementioned studies do treat the wing deformation).

One of the current trends being explored in the experimental flapping flight researchers is the expanding the flight envelope from just a hovering or simple forward flight to the other flight mode, such as takeoff (Tobalske, 2004), turning, or even backward flight (Sapir and Dudley, 2012). The environmental conditions are sometimes also not simple. For instance, flight in low (Chai and Dudley, 1996; Altshuler and Dudley, 2003; Altshuler et al., 2004) or high (Altshuler et al., 2001) density gases, flight with added weight (Chai, 1997; Chai and Millard, 1997; Dillon and Dudley, 2004; Mountcastle and Combes, 2013), or even flight in the rain (Ortega-Jiménez and Dudley, 2012) have been tested. This has a strong attraction to the biology community, whose main focuses are usually the animal behavior, ecology, or sometimes evolution (Hedrick, 2011).

Another direction being pursued is the detailed model design. It has been know that, quite roughly speaking, that when the Reynolds number is low, the angle of attack is large, and the flow is rather highly unsteady, there would very likely be the dominance of leading-edge vortex in terms of aerodynamic forces. Otherwise, conventional aerodynamics for fixed- or rotary-wing aerodynamics would be able to explain most of the lift generation. So the recent trends in the study of the aerodynamics of flapping flight has been departing from qualitative (why or how an animal can fly) to quantitative (how much energy is used or how well it can generate lift or thrust) ones. When tackling such issues, the simplified wing models do not always sufficient and usually requiring the consideration of wing deformation. These lines attract of particular interest from the aerospace engineering community, because people want to know the design criteria of how to build efficient and effective flapping-wing machines.

In the present paper, I ambitiously pursue the both trends. In Chapter 2, a recent concept in the flight stability problem, termed flapping counter torque (FCT, Hedrick et al., 2009) acting on a hovering fruit fly is tested via CFD with the aid of a newly-developed simplified flight dynamics solver. This is the one of the attempts to depart from the ordinary hovering. In Chapter 3, the same fruit fly model is placed close to the ground surface. Although the flight mode is a simple tethered hovering, an interference of the ground to the fly, so-called ground effect, is observed. In Chapter 4, in addition to ground effect, jumping off of the ground in takeoff is investigated. The ground reaction force at takeoff is commonly termed as leg thrust, and one of the objectives is to estimate this leg thrust via experiment and numerical simulation. Because a swallowtail butterfly is used as the specimen, the significant wing deformation is also needed to be considered. In Chapter 5, a hovering hummingbird is photo recorded and the flow field around the wing is numerically solved. The wing of hummingbird is usually referred to as rigid even by the biomechanics researchers. Although it is true that the wing is less compliant compared to the wings of larger birds which have well movable joints, I show the wing of hummingbird is not as rigid as it might seem, and the wing deformation cannot be neglected in the estimation of aerodynamic performance.

References

Altshuler, D. L., Chai, P. and Chen, J. S. (2001), 'Hovering performance of hummingbirds in hyperoxic gas mixtures', *J. Exp. Biol.* **204**, 2021–2027.

Altshuler, D. L. and Dudley, R. (2003), 'Kinematics of hovering hummingbird flight along simulated and natural elevational gradients', *J. Exp. Biol.* **206**(18), 3139–3147.

Altshuler, D. L., Dudley, R. and McGuire, J. A. (2004), 'Resolution of a paradox: hummingbird flight at high elevation does not come without a cost', *Proc. Natl. Acad. Sci. U. S. A.* **101**(51), 17731–17736.

Aono, H., Liang, F. and Liu, H. (2008), 'Near- and far-field aerodynamics in insect hovering flight: an integrated computational study.', *J. Exp. Biol.* **211**, 239–257.

Aono, H., Shyy, W. and Liu, H. (2009), 'Near wake vortex dynamics of a hovering hawkmoth', *Acta Mech. Sin.* **25**(1), 23–36.

Bomphrey, R. J. (2011), 'Advances in Animal Flight Aerodynamics Through Flow Measurement', *Evol. Biol.* **39**(1), 1–11.

Chai, P. (1997), 'Hummingbird hovering energetics during moult of primary flight feathers.', *J. Exp. Biol.* **200**, 1527–1536.

Chai, P. and Dudley, R. (1996), 'Limits to flight energetics of hummingbirds hovering in hypodense and hypoxic gas mixtures', *J. Exp. Biol.* **199**, 2285–2295.

Chai, P. and Millard, D. (1997), 'Flight and size constraints: hovering performance of large hummingbirds under maximal loading', *J. Exp. Biol.* **200**, 2757–2763.

Dillon, M. E. and Dudley, R. (2004), 'Allometry of maximum vertical force production during hovering flight of neotropical orchid bees (Apidae: Euglossini)', *J. Exp. Biol.* **207**(3), 417–425.

Hamamoto, M., Ohta, Y., Hara, K. and Hisada, T. (2013), 'Free-flight analysis of dragonfly hovering by fluidstructure interaction analysis based on an arbitrary LagrangianEulerian method', *Adv. Robot.* **27**(9), 657–666.

Hedrick, T. L. (2011), 'Damping in flapping flight and its implications for manoeuvring, scaling and evolution', *J. Exp. Biol.* **214**(24), 4073–4081.

Hedrick, T. L., Cheng, B. and Deng, X. (2009), 'Wingbeat Time and the Scaling of Passive Rotational Damping in Flapping Flight', *Science* **324**, 252–255.

Le, T. Q., Truong, T. V., Park, S. H., Truong, T. Q., Ko, J. H., Park, H. C. and Byun, D. (2013), ‘Improvement of the aerodynamic performance by wing flexibility and elytra-hind wing interaction of a beetle during forward flight’, *J. R. Soc. Interface* **10**(85), 20130312.

Liu, H. and Aono, H. (2009), ‘Size effects on insect hovering aerodynamics: an integrated computational study.’, *Bioinspir. Biomim.* **4**(1), 015002.

Liu, H., Ellington, C. P., Kawachi, K., van den Berg, C. and Willmott, A. P. (1998), ‘A computational fluid dynamic study of hawkmoth hovering’, *J. Exp. Biol.* **201**, 461–477.

Liu, Y., Cheng, B., Barbera, G., Troolin, D. R. and Deng, X. (2013), ‘Volumetric visualization of the near- and far-field wake in flapping wings.’, *Bioinspir. Biomim.* **8**(3), 036010.

Mountcastle, A. M. and Combes, S. A. (2013), ‘Wing flexibility enhances load-lifting capacity in bumblebees’, *Proc. R. Soc. B* **280**, 20130531.

Nakata, T., Liu, H., Tanaka, Y., Nishihashi, N., Wang, X. and Sato, A. (2011), ‘Aerodynamics of a bio-inspired flexible flapping-wing micro air vehicle.’, *Bioinspir. Biomim.* **6**(4), 045002.

Ortega-Jiménez, V. M. and Dudley, R. (2012), ‘Flying in the rain: hovering performance of Anna’s hummingbirds under varied precipitation’, *Proc. R. Soc. B* **279**(1744), 3996–4002.

Ramamurti, R. and Sandberg, W. C. (2007), ‘A computational investigation of the three-dimensional unsteady aerodynamics of Drosophila hovering and maneuvering.’, *J. Exp. Biol.* **210**(Pt 5), 881–96.

Sapir, N. and Dudley, R. (2012), ‘Backward flight in hummingbirds employs unique kinematic adjustments and entails low metabolic cost.’, *J. Exp. Biol.* **215**(Pt 20), 3603–11.

Sun, M. and Lan, S. L. (2004), ‘A computational study of the aerodynamic forces and power requirements of dragonfly (Aeschna juncea) hovering’, *J. Exp. Biol.* **207**, 1887–1901.

Sun, M. and Tang, J. (2002*a*), ‘Lift and power requirements of hovering flight in Drosophila virilis.’, *J. Exp. Biol.* **205**, 2413–2427.

Sun, M. and Tang, J. (2002*b*), ‘Unsteady aerodynamic force generation by a model fruit fly wing in flapping motion.’, *J. Exp. Biol.* **205**, 55–70.

Tobalske, B. W. (2004), ‘Take-off mechanics in hummingbirds (Trochilidae)’, *J. Exp. Biol.* **207**(8), 1345–1352.

Wang, J. K. and Sun, M. (2005), ‘A computational study of the aerodynamics and forewing-hindwing interaction of a model dragonfly in forward flight.’, *J. Exp. Biol.* **208**, 3785–3804.

Young, J., Lai, J. C. S. and Germain, C. (2008), 'Simulation and Parameter Variation of Flapping-Wing Motion Based on Dragonfly Hovering', *AIAA J.* **46**(4), 918–924.

Young, J., Walker, S. M., Bomphrey, R. J., Taylor, G. K. and Thomas, A. L. R. (2009), 'Details of insect wing design and deformation enhance aerodynamic function and flight efficiency', *Science* **325**(5947), 1549–1552.

Zheng, L., Hedrick, T. L. and Mittal, R. (2013*a*), 'A multi-fidelity modelling approach for evaluation and optimization of wing stroke aerodynamics in flapping flight', *J. Fluid Mech.* **721**, 118–154.

Zheng, L., Hedrick, T. L. and Mittal, R. (2013*b*), 'Time-varying wing-twist improves aerodynamic efficiency of forward flight in butterflies', *PLoS One* **8**(1), e53060.

Chapter 2

Flapping flight with whole-body motion: flapping counter torque

2.1 Introduction

To date, in order to obtain time course of the aerodynamic forces, stable hovering or steady forward flight has been the main subjects, where either a robotic flapper or numerical simulation was used. Sometimes the inverse dynamics is also used for a real insect in such flight conditions. It does not seem to be there is a large number of aerodynamic force measurement or computation on the other flight sequences such as takeoff or turning, where there is a translational and/or a rotational acceleration of the body, which would significantly affect the generation of aerodynamic forces or torques. There exists at least one set of experimental (Fry et al., 2003) and numerical (Ramamurti and Sandberg, 2007) efforts for turning flight where both the wing kinematics and body motion are prescribed. For stability or control analysis, however, equations of motion must be solved (Wu et al., 2009). For this purpose, we have developed a coupled solver of fluid dynamics and simplified flight dynamics for a rigid body (Maeda et al., 2010).

In this chapter I show the free flight simulation of a fruit fly with initial yawing angular velocity. It has been reported there is an auto-stabilizing mechanism against rotational motion of a flapping flyer termed as flapping counter torque (FCT), which is summarized in a Commentary by Hedrick (Hedrick, 2011). The objectives of the current chapter are twofold. One is the confirmation of the flapping counter torque with a Navier-Stokes solver instead of simple blade-element model. So far there has been no report of such a numerical simulation. The high-accuracy numerical simulation of FCT would promote deeper understanding of the phenomena, together with the experimental simulations (Cheng et al., 2010; Dickson et al., 2010). Another aim is to test the effect of 6 degrees of freedom (6 DoF) to the yaw dynamics. The previous studies treated only 1 DoF turning but there could be coupling between other axes, consideration of which would be necessary for the realistic situations.

I carried out an FCT simulation with similar setup to the previous experimental study (Hedrick et al., 2009) using a coupled solver of computational fluid dynamics (CFD) and simplified rigid body dynamics (sRBD) solver. The results of the computation are rather surprising. The deceleration due to flapping counter torque is clearly confirmed, but the decay of angular velocity is faster than either blade-element estimation or experimental observation. The 6 DoF simulation also resulted in quicker halt but with roll and pitch disturbance. One explanation for this situation is the inclusion of active control during the voluntary turning in order to stabilize roll and pitch.

2.2 Methods

The numerical simulation was carried out with coupling two solvers, fluid dynamics solver and simplified flight dynamics solver. The details of these solvers are described in the appendices A and B, respectively.

2.2.1 Modeling the fruit fly with flapping counter torque (FCT)

A fruit fly model is used for the FCT computation. The parameters for the model are presented in Table 2.1. The fruit fly (Drosophila melanogaster) model is basically the same as that used in Aono et al. (Aono et al., 2008). A body and two wings are assumed to be rigid and no deformation is considered. In order to see the effect of the deceleration due to the symmetric flapping motion combined with the rotational motion, or Flapping Counter Torque (FCT), we applied an initial angular velocity to the fruit fly. To exclude the effect of impulsive large aerodynamic forces/torques at the beginning of the flow field computation, the fruit fly is given the constant angular velocity of 1,600 deg/s around z-axis (vertical axis) in the inertial frame during the initial one wingbeat cycle ($-1 \leq t/T \leq 0$, Fig. blue solid line in 2.2C). During this forced rotation period, only the fluid dynamics is solved and flight dynamics solver is disabled. At $t/T = 0.0$, the fly is released, when the flight dynamics is activated. The computation is run until $t/T = 4.0$. Note the z-axis of inertial frame coincides with the z-axis of stroke plane frame in Hedrick et al. since the stroke plane angle is zero in the both studies.

2.2.2 Effect of wing kinematics

Four simulation cases are performed. In the first case, a 1 degrees-of-freedom (DoF) computation is done where only the rotational motion around z-axis of inertial frame is allowed after the release. The hovering wing kinematics is shown in the Fig. 2.1 and is the same as that used in Aono et al. (Aono et al., 2008). Therefore, this story behind this simulation is such as: a fly in a stable hover is affected by an idealized

Table 2.1. Model parameters. Moment of inertia is the wingbeat cycle-averaged value in the body frame.

Reynolds number, Re	139
Reduced frequency, k	0.210
Wing length, R (mm)	2.39 [a]
Mean chord length, c_{m} (mm)	0.80 [a]
Reference velocity, U_{ref} (m/s)	2.61
Wingbeat frequency, f (Hz)	218
Wingbeat amplitude, Φ (deg)	143
Density of air, ρ (kg/m^3)	1.225
Kinematic viscosity of air, ν (m^2/s)	1.5×10^{-5}
Stroke plane angle, χ (deg)	0
Body angle, β (deg)	50 [a]
Total mass, M (mg)	0.96
Body mass, m_{b} (mg)	0.9504
Wing mass (two wings), m_{w} (mg)	0.0096
Moment of inertia (x'-direction), $J'_{x'}$ (N·ms^2)	$1.11{\times}10^{-13}$
Moment of inertia (y'-direction), $J'_{y'}$ (N·ms^2)	$5.12{\times}10^{-13}$
Moment of inertia (z'-direction), $J'_{z'}$ (N·ms^2)	$5.11{\times}10^{-13}$

[a] Hedrick et al., 2009.

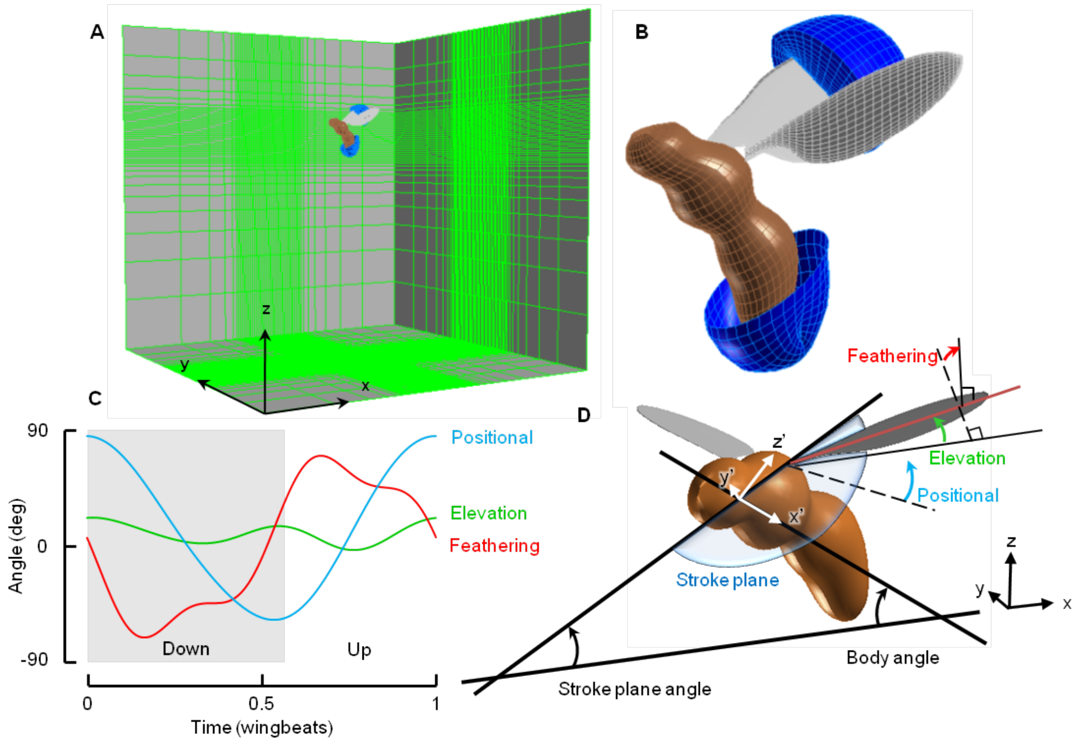

Figure 2.1. Fruit fly model. Grid system (A). Close up view of fruit fly grid (B) where blue spheres indicate outer boundaries of each block. Wing kinematics (C) and the definitions of the wing and body angles, as well as the illustration of the body frame (D). Note the feathering angle is defined so that it corresponds to (90 - α_{geo}) when the elevation angle is zero, where α_{geo} is geometrical angle of attack.

gust so that it obtains a pure yawing rotation, but it still does not notice it is rotating because of the sensory delay, and continuing the same symmetric kinematics as hovering. According to Hedrick and colleagues, the fly must stop its rotation without actively changing the wing kinematics asymmetrically. In another case, a 6 DoF flight dynamics is allowed after the release, instead of 1 DoF. The other two cases are 1 DoF computations but the wings do not flap: in one case the feathering angle is 0 deg (i.e. geometrical angle of attack is 90 deg) and in the other the feathering angle is -90 deg (i.e. geometrical angle of attack is 0 deg). The overall conditions of the simulations are similar to those in Hedrick et al. Major differences in our computation are twofold. One is that the full 3D Navier-Stokes equations are solved in my study, compared to the quasi-steady blade element method in theirs. Therefore more precise aerodynamic forces and torques are expected. The other is that in one case 6 DoF rigid body dynamics is computed with fully coupled with the flow solver, from which coupling effect could be observed.

2.3 Results

The result of fruit fly simulation is summarized in Figs. 2.2 and 2.3. Note in Fig 2.3 the dotted lines correspond to the 1 DoF simulation results and the solid lines to the 6 DoF simulation results. History of aerodynamic torque around z-axis of inertial frame (N_{az}) is shown in Fig. 2.2A and B. Note when the aerodynamic torque is negative, it acts to retard the rotation. Clearly the flapping motion enhances the counter torque, as shown in the previous studies. The effect of the FCT is further clearer in the history of normalized angular yaw velocity in inertial frame (Fig 2.2C). However, in our simulation the time to reach the half the maximum (initial) angular velocity is approximately one wingbeat cycle in the 1 DoF flapping case (blue line), which is about half the value in Hedricks observation and modeling. At this stage of the research, the reason of the discrepancy is unknown. One possible reason had been the phase of wing kinematics, i.e. at which state do we start the flapping simulation: downstroke, upstroke or in between. Therefore, we tested four different flapping phases including current one (starting from downstroke), but the overall decay slope was not affected (results not shown).

In the 6 DoF case (red lines), the aerodynamic torque looks diverging (Fig. 2.2B), so is the angular velocity (Fig. 2.2C). The angular velocity oscillates around zero, which is not observed in the 1 DoF case. Therefore this phenomenon is likely to be arisen from the coupling effect from the other degrees of freedom. One prominent difference between 1 DoF and 6 DoF cases is the pitching oscillation (Figs 2.3D, E). This is the natural consequence of the large pitching aerodynamic torque (Fig 2.3B); there is a quite similar trend in the case of 1 DoF, but any motions except for the yaw is magically canceled and do not appear (Fig. 2.3D). Another feature of the 6 DoF simulation is the presence of the translational body motion (Fig 2.3A). Therefore it can be presumed the strong pitching torque together with translational

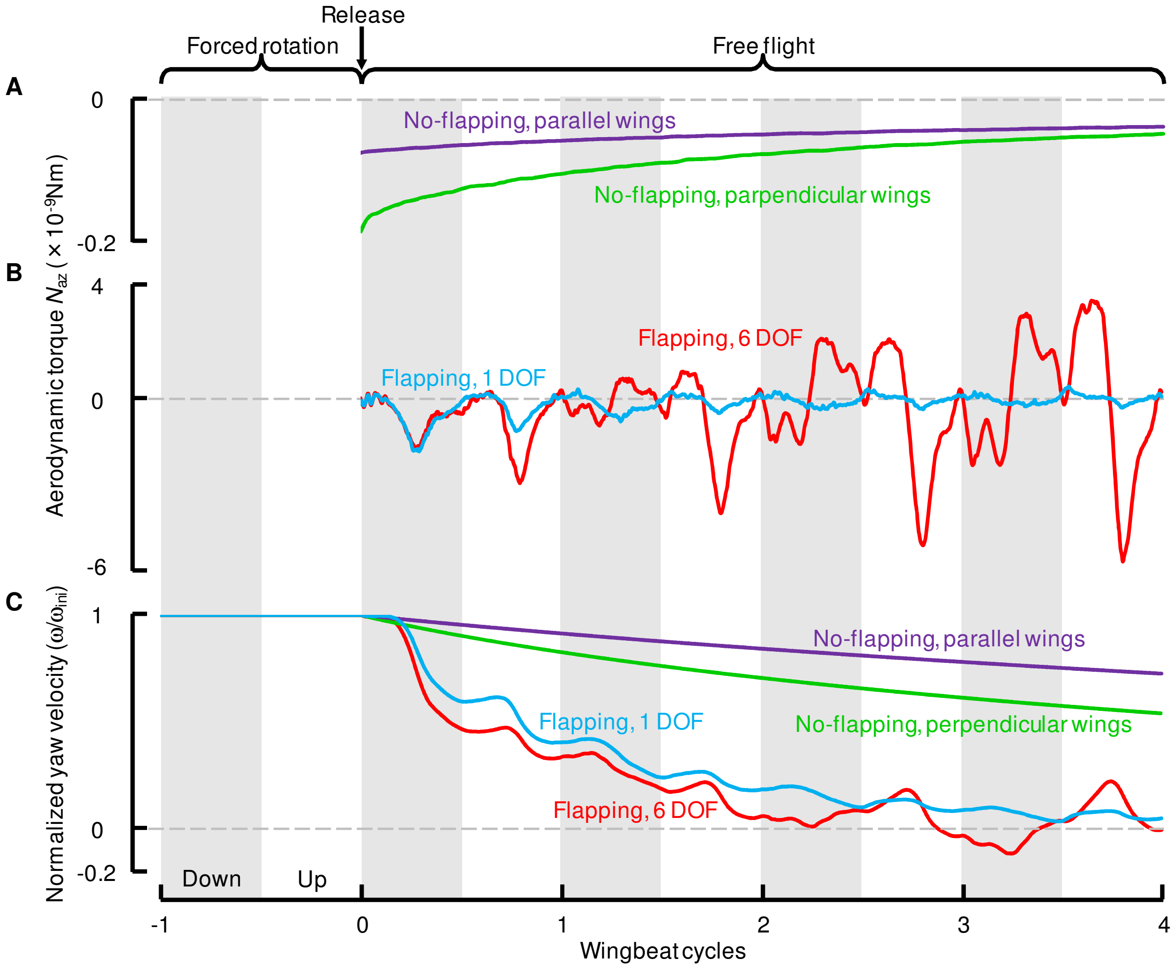

Figure 2.2. Instantaneous aerodynamic torques (A, B) and normalized yaw velocities (C). Blue, 1 DoF simulation with wings flapping; red, 6 DoF simulation with wings flapping; green, 1 DoF simulation with wings are fixed as perpendicular to the stroke plane (feathering angle = 0); and purple, 1 DoF simulation with are fixed as parallel to the stroke plane (feathering angle = -90 deg).

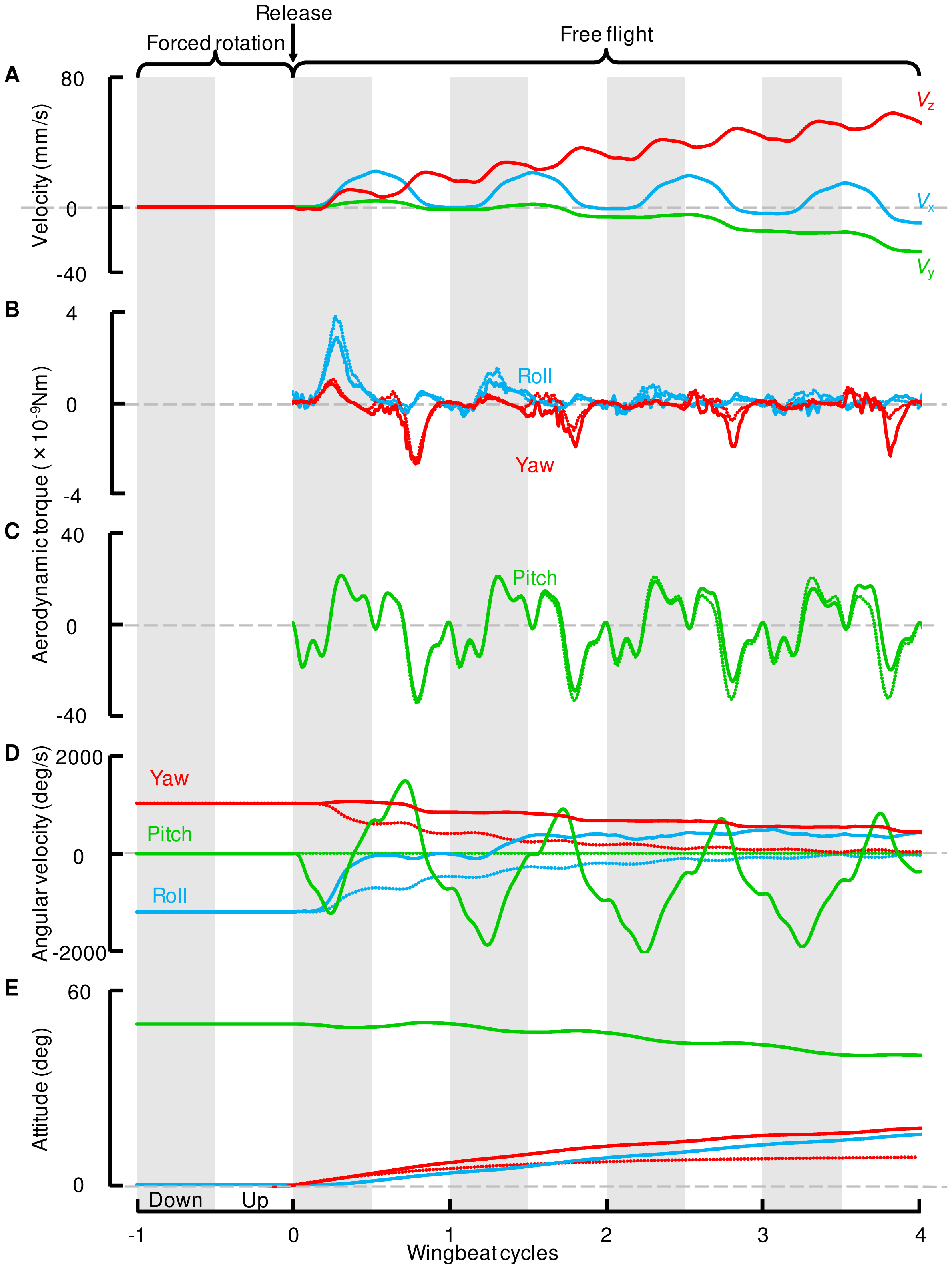

Figure 2.3. Histories for 6 DoF (solid lines) and 1 DoF (dotted lines) simulation of a fruit fly. Velocity (A), aerodynamic torque in the body frame (B, C), angular velocity in the body frame (D), and body attitude (E) are shown.

motion is likely to be responsible for the slower reduction in the body frame yaw angular velocity and increasing trend in the body frame rolling angular velocity.

The yaw torque and yaw angular velocity

2.3.1 Visualization of flow-field and body attitude

The visualization of the flow field and body motion at the beginning of each wingbeat period is presented in Fig. 2.4. The white and yellow smoke-like objects are the Q-criterion iso-surface which is commonly used for visualizing vortex.

The surface pressure contours of the 1 DoF flapping model at the first mid-downstroke after release ($t/T = 1.3$) is shown in Fig. 2.5. This timing was selected because the strongest counter torque is observed (Fig. 2.2B, blue line). The low pressure regions near the leading edges corresponds to the leading-edge vortices (LEVs). It is evident the right wing exhibit slightly lower pressure.

2.4 Discussion

2.4.1 Flapping counter torque mechanism

Flapping counter torque was confirmed. But the surface pressure difference between right wing and left wing surfaces in the 1 DoF computation looks very small. This is logical, however, considering the contribution of the initial yaw angular velocity for the wing angular velocity. Fig. 2.6 shows the angular velocities of right wing in terms of positional angle with or without FCT. The peak angular velocity exceeds 80000 deg/s, and the absolute angular velocity is more than 16000 deg/s (ten times the initial angular velocity of 1600 deg/s) for around 90 % of the wingbeat period.

The small aerodynamic forces in the non-flapping computations are evident from the vortices in the flow field visualization (Fig. 2.4) because the yellow iso-surfaces in non-flapping cases are two orders of magnitude smaller than the white iso-surfaces in the flapping cases (0.001 compared to 0.1, in dimensionless form). Therefore, it is further clarified that flapping is the better way than the simple aero-breaking for fruit flies.

2.4.2 Effect of phase

Three different phases of wing kinematics were tested (Fig. 2.7). The conditions are the same as the 1 DoF computation but the wing kinematics were shifted by $\pi/2$, π, and $3\pi/4$ from the original kinematics. However, the general decay trends are quite similar to the one in the original phase.

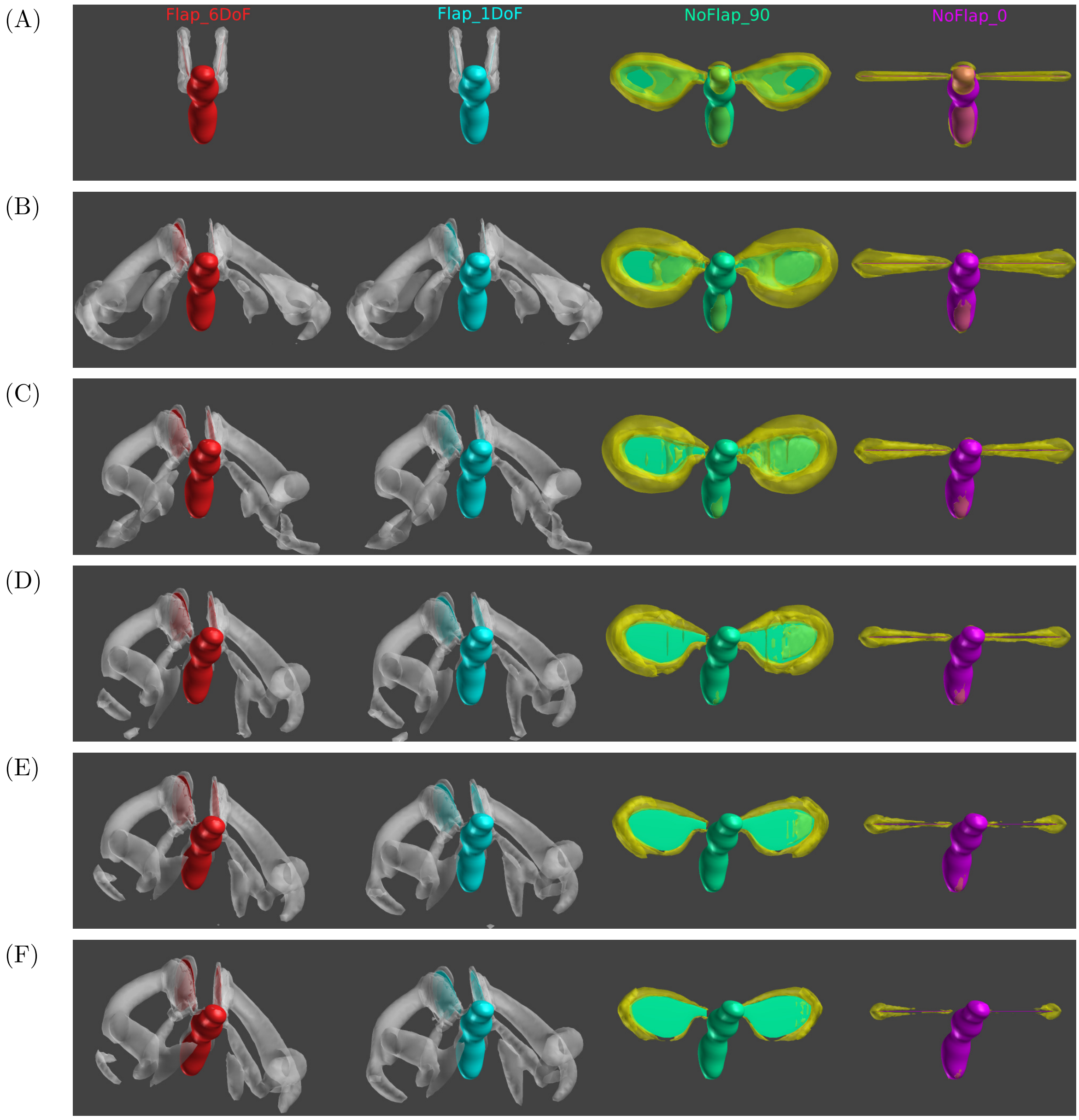

Figure 2.4. Visualization of the motion and flow around the wings. (Left to right) red model, flapping with 6 DoF dynamics; blue model, flapping with 1 DoF dynamics; green model, no flapping and wings are perpendicular to the stroke plane; and purple model, no flapping and wings are parallel to the stroke plane. White transparent smoke-like objects in the left two models are the iso-surfaces of Q-criterion at 0.1; the yellow ones in the right two models are those at 0.001. (A) to (F) correspond to t/T = -0.075, 0.0, 1.0, 2.0, 3.0, and 4.0, respectively. Note that in each model, insect is under forced yaw rotation to its left during $t/T \leq 1.0$ (i.e. zero degrees of freedom until B).

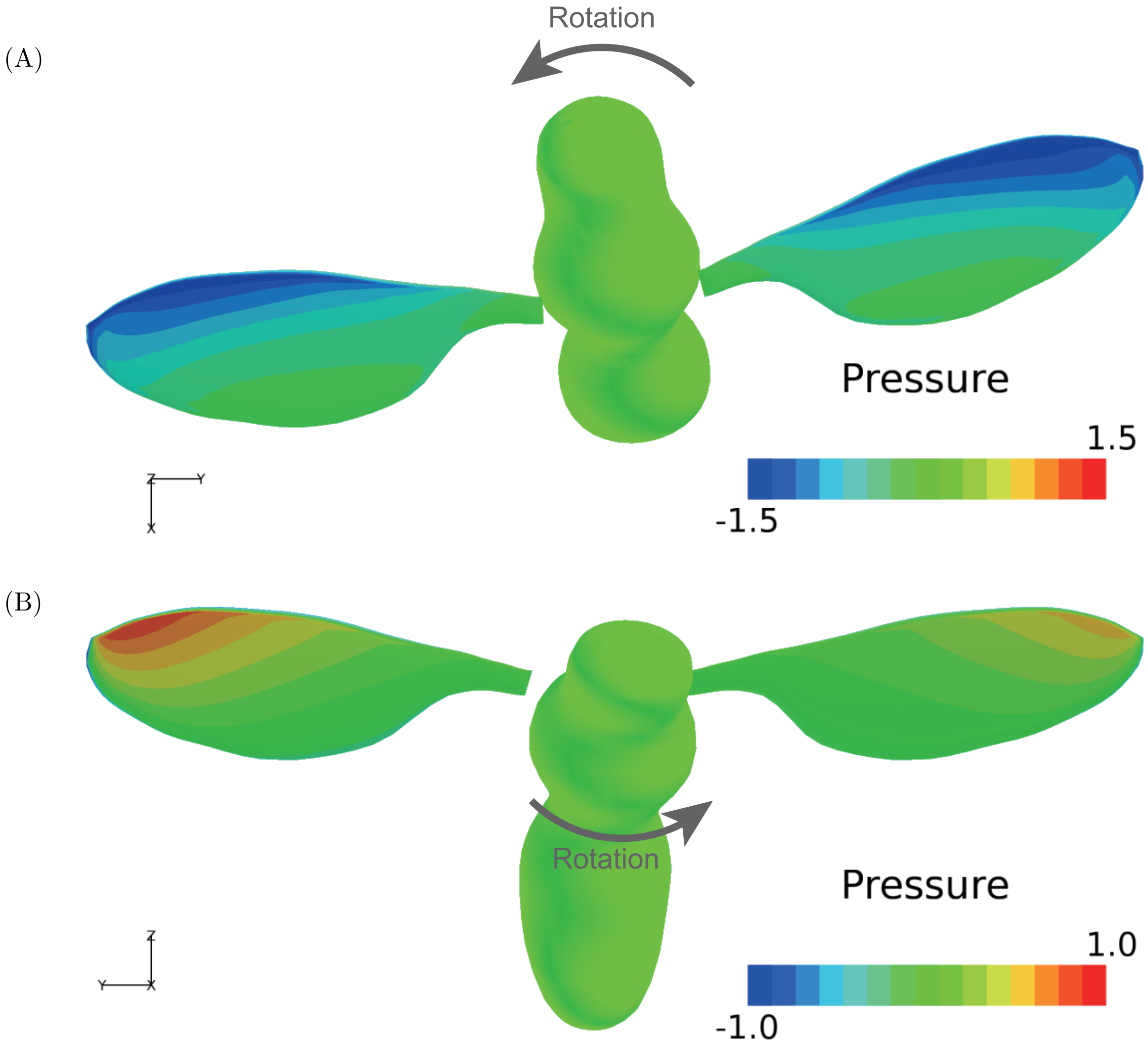

Figure 2.5. Dorsal (A) and ventral (B) views of 1 DoF flapping model at $t/T = 0.3$ (first mid-downstroke in free rotation periods), showing surface pressure contours. Note the pressure is normalized gauge pressure and the range is different for (A) and (B).

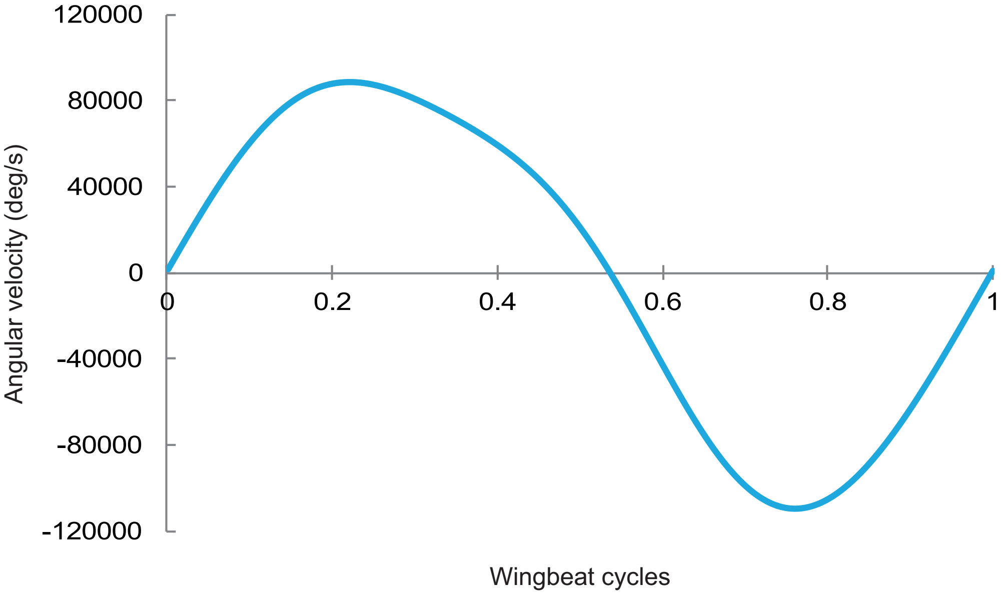

Figure 2.6. Angular velocity as the derivative of positional angle for right wing. Positive value corresponds to the downstroke.

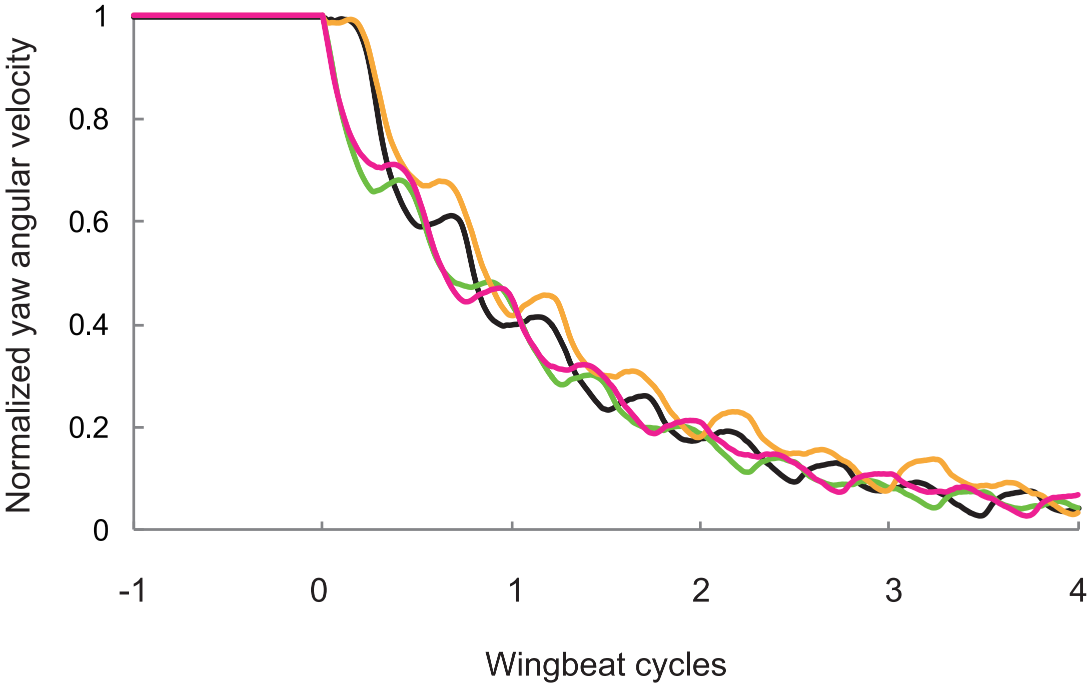

Figure 2.7. Effect of initial wing phase on the angular velocity decay. Black, original wing phase (same as blue line in Fig. 2.2); green, phase shifted by $\pi/2$; orange, phase shifted by π; and magenta, phase shifted by $3\pi/4$.

2.4.3 Comparison between blade element calculation

The non-dimensional decay half-life ($t_{1/2}$) is the time taken for a decelerating fly to reach half the initial angular velocity, divided by wingbeat period. The prediction of this value by my computation was slightly less than one (Figs. 2.2 and 2.7). This is more than twice faster compared to the 2.00 ± 0.32 wingbeats in Hedrick et al. (Table 1 in Hedrick et al., 2009). There could be several possible reasons for this discrepancy.

Moment of inertia

Moment of inertia plays the significant role in the rotational dynamics. If the yawing moment of inertia is smaller in my computation, the deceleration would be quicker because the angular momentum the insect has at the time of release would be smaller. For comparison, the z-component of moment of inertia in the stroke plane frame J_z is calculated from the values in the body frame (Table 2.1) as (eq. S37 in Supporting Online Material for Hedrick et al., 2009):

$$J_z = J'_{z'} \cos^2 \beta + J'_{x'} \sin^2 \beta = 2.76 \times 10^{-13} \ (\mathrm{N \cdot m\, s^2}) \tag{2.1}$$

where $J'_{x'}$ and $J'_{z'}$ are x'- and z'- components of the moment of inertia in the body frame, and β is body angle (50 deg). This is very close to the value used in the blade element calculation ($I'zz = 2.72 \times 10^{-13}$ $\mathrm{N \cdot m\, s^2}$, Table 1 in Hedrick et al., 2009). Thus, this should not be the reason of the discrepancy.

Morphological, kinematical, or environmental parameters other than moment of inertia

The other morphological and kinematics parameters directly comparable are wing length R, mean chord length c_m ($\bar{c}$ in Hedrick et al., 2009), wingbeat frequency f (n in Hedrick et al., 2009), wingbeat amplitude Φ, and mass M. However, I have chosen the same values as Hedrick et al. Wingbeat amplitude is slightly larger but it is just around 2 percent greater (143 deg compared to 140 deg in Hedrick et al.) thus would not explain the difference in the decay. Air density is not explicitly written in the literature but it would probably be 1.23 kg/m^3 or close.

In terms of morphology, non-dimensional third moment of area $\hat{r}_3(S)$, which is dependent upon the wing planform shape, may be slightly different as well, and since this variable is cubed in the blade-element model (eq. S23 in Supporting Online Material for Hedrick et al., 2009), even the slight difference could be amplified and potentially results in a substantial difference in the resultant decay speed. According to Table 1 in Hedrick et al. or Table 1 in Ellington (Ellington, 1984)), the variation of $\hat{r}_3(S)$ across the species is roughly from 0.54 to 0.64, i.e. 0.59 ± 0.5, where 0.59 is the value for fruit fly in Hedrick et

Figure 2.8. Comparison of aerodynamic yawing torques acting on body (magenta solid line) and two wings combined (gray dashed line).

al. This results in $\hat{r}_3^3(S)$ from 0.157 to 0.262, which correspond to 23 % decrease and +28 % increase. However, since my wing model is also based on the real fruit fly planform (Aono et al., 2008), it is not very likely that the $\hat{r}_3(S)$ (and hence $\hat{r}_3^3(S)$) in my model falls in to these extremes. Therefore, the influence of planform difference would be, if any, limited. Probably of the order of ten percent or so.

Aerodynamic torque on body

The force acting on the body is considered in my computation but neglected in Hedrick et al. However, as mention by them, this value is quite low (Fig. 2.8) and should not cause the large discrepancy.

Wing kinematics

Wing kinematics is quite different between the studies. I have employed the realistic wing kinematics (Aono et al., 2008) original from Fry et al. (Fry et al., 2003, 2005). Contrastingly, simple harmonic motion and lower amplitude of feathering angle (± 45 deg compared to my $\pm 60^+$ deg). This difference in wing kinematics seems to have a quite large impact on the result.

Actually, the selection of feathering amplitude affect the FCT model. I re-calculate the FCT model and found that their approximation of $K \simeq 6.0$ is underestimation by itself. First, obviously $\hat{\phi}$ in the eq. S25 must be a typographical error and should be replaced with $\hat{t}$, i.e.,

$$\alpha(\hat{t}) = \frac{\pi}{4} |\tanh\left(2.2 \sin\left(2\pi\hat{t}\right)\right)| \tag{2.2}$$

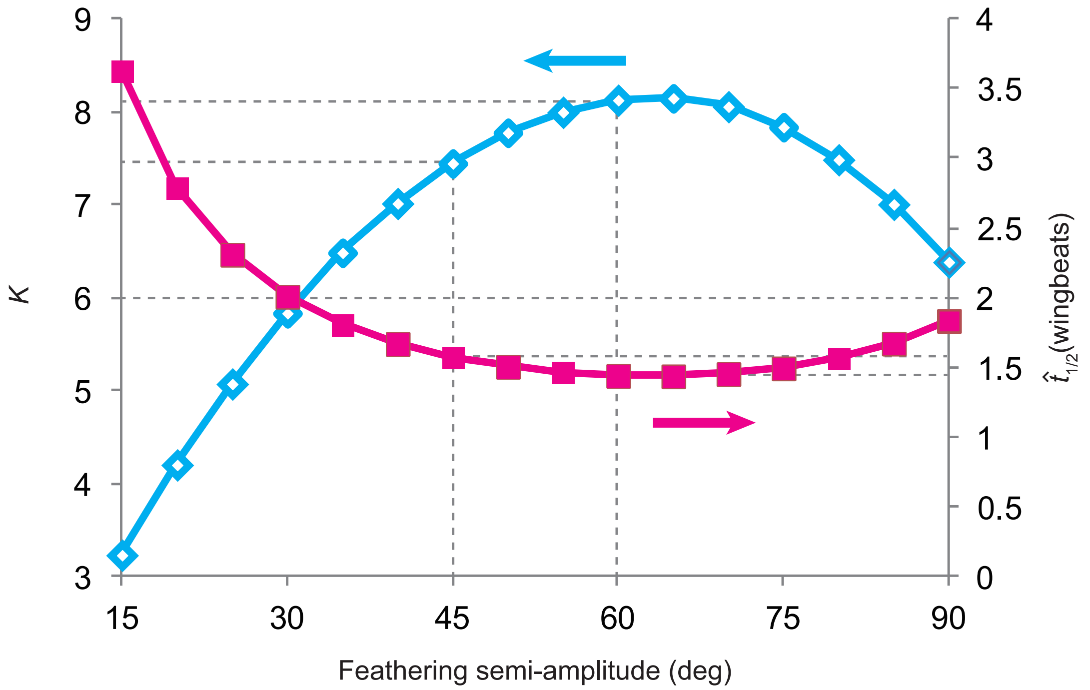

Figure 2.9. The relationship between feathering semi-amplitude and K (blue open diamonds) or $\hat{t}_{1/2}$ (magenta filled squares).

otherwise the history of $\alpha(\hat{t})$ looks unrealistic. Although the curve from eq. 2.2 does not actually reaches 45 deg, it looks to be true.

Then, simple calculations using Excel with time step $\mathrm{d}\hat{t} = 0.001$ and assuming mean positional angle being zero, I obtained $K \simeq 7.45$ (or -7.45, depending on the selection of positive direction of positional angle), which is fairly larger than 6. The greater K means stronger aerodynamic damping. In fact, calculating with $K = 7.45$ obtains non-dimensional half life $\hat{t}_{1/2} \simeq 1.58$ (Fig. 2.9). Furthermore, the kinematics in my computation is different and the feathering semi-amplitude for my model was around 60 deg. This yields slightly lower value of $K \simeq 8.13$ and $\hat{t}_{1/2} = 1.45$ (Fig. 2.9). Hedrick et al. selected $K = 6$ presumably because they wanted to use the same value for all the species other than fruit fly, whose drag coefficients C_D would possibly lower than that of fruit fly. However, this selection makes the effectively lower the feathering semi-amplitude (around 30 deg. See Fig. 2.9) which resulted in the increase in the angular velocity half-life by around half the wingbeat cycle from 1.5 to 2.0.

Other considerations

The selection of accurate parameter K makes the discrepancy smaller. However, there is still around half the wingbeat difference. The possible causes include different wing kinematics (esp. feathering angle and elevation angle), insufficient grid density, three dimensional effect, or nonlinear coupling effect in my numerical simulation. All of them may alter the aerodynamic forces and hence torque, which corresponds to the alteration of C_F (force coefficient) in the model of Hedrick et al. For example, spanwise flow and LEV (leading-edge vortex) formation and stabilization could be affected by the whole-body rotation Lentink and Dickinson (2009), which might not have captured well in the blade-element model. Another possible error arises from the assumption of constant location of center of pressure in the blade-element model. It is not very clear which location they chose from Hedrick et al., 2009 but in an accompanying paper it is the 70% wing length (Cheng et al., 2010). From the pressure contour of the current study (Fig. 2.5) the center of pressure in my fruit fly may locate slightly nearer to the wingtip, which must be calculated for further investigation.

2.4.4 Comparison between observation

The difference between blade-element model and the current CFD-sRDB coupled computation has partly been explained. However, there still remains a notable difference between experimental results and my computation. The real fruit fly takes slightly longer than 2 wingbeats to reach half the initial yaw angular velocity (Fig. 2A of Fry et al., 2003, dark blue line in Fig. 3B of Hedrick et al., 2009). This is more than twice the time of my computation and around 30 % longer than the blade-element calculation with more realistic K value, therefore need some explanations.

One such explanation is the real fruit fly *in a voluntary turning* is not actually use the truly symmetrical flapping. Consider a real fruit fly in a voluntary turning, or, saccade. During the course of flight, the fly must be keep controlling its body orientation not only yaw but roll and pitch, as well as translational motions. Then it is not quite reasonable to suddenly stop active control and change the wing kinematics to perfect symmetrical one, totally relying on the passive damping due to FCT. Specifically, my 6 DoF computation shows the symmetrical wingbeat induces roll, pitch, and translational deviations. In the real observation, however, the deviation in pitch seems to be negligible and roll is also small, but slight changes in vertical and horizontal velocities are observed (Fig. 2A of Fry et al., 2003), whereas the wing kinematics, especially elevation angle and feathering angle are slightly but notably different between right and left wings, even at the onset of the yaw deceleration ('deviation' and 'angle of attack' in Fig. 2B of Fry et al., 2003. Look at just after the 'Saccade' period). The partial contribution from active control has also been suggested from robotic fly experiment (Cheng et al., 2010), although the conclusion is opposite with my current study: they concluded FCT is insufficient for the termination of yaw turning and requires additional active counter torque. Therefore, it may be safer to state it requires further examinations in terms of voluntary turning. My impression is that the fly need to actively stabilize mainly the translational motion, because flapping counter force (FCF) due to whole-body translational motion (Cheng et al., 2010).

What I want to emphasize here is the distinction between voluntary turnings and the response to external disturbance, e.g. gust or visual stimuli. If the animal is in a symmetric hovering and then exposed to a disturbance then at least during the duration of the latency, there is no way of executing active control and the fly must rely on the passive, flapping counter torque. Then the fly react to the disturbance by actively changing the wing kinematics Ristroph et al. (2010). This include two differences against voluntary turning. One is that the insect had not been in the active yaw control. Another is that the disturbance would very likely not a pure yaw rotation but a translational movement or combination of translational and rotational. Therefore, we should be careful to the situation the flapping flyers are in when discussing active/passive discussion.

2.5 Conclusion

Flapping counter torque is for the first time confirmed in the coupling of a Navier-Stokes solver and a simplified rigid dynamics solver. The results of both 1 DoF and 6 DoF computations show substantially faster decay in the yaw angular velocity compared to either blade-element model or observation. The cause of the discrepancy between blade element model is partially resolved but slight deviation remains for further study. The discrepancy against observation implies the inclusion of active control at the end of the voluntary turning, and the distinction between a voluntary turning and the gust response was underscored.

Future works may include the FCT simulation on the other flapping flyers such as hawkmoth (observation and robotic experiment have been done, see Hedrick and Robinson, 2010; Cheng et al., 2011), hummingbird (Altshuler et al., 2012), or a micro air vehicle (MAV. See Sunada et al., 2010).

References

Altshuler, D. L., Quicazán-Rubio, E. M., Segre, P. S. and Middleton, K. M. (2012), 'Wingbeat kinematics and motor control of yaw turns in Anna's hummingbirds (Calypte anna).', *J. Exp. Biol.* **215**, 4070–4084.

Aono, H., Liang, F. and Liu, H. (2008), 'Near- and far-field aerodynamics in insect hovering flight: an integrated computational study.', *J. Exp. Biol.* **211**, 239–257.

Cheng, B., Deng, X. and Hedrick, T. L. (2011), 'The mechanics and control of pitching manoeuvres in a freely flying hawkmoth (Manduca sexta)', *J. Exp. Biol.* **214**(Pt 24), 4092–106.

Cheng, B., Fry, S. N., Huang, Q. and Deng, X. (2010), 'Aerodynamic damping during rapid flight maneuvers in the fruit fly Drosophila', *J. Exp. Biol.* **213**, 602–612.

Dickson, W. B., Polidoro, P., Tanner, M. M. and Dickinson, M. H. (2010), 'A linear systems analysis of the yaw dynamics of a dynamically scaled insect model', *J. Exp. Biol.* **213**, 3047–3061.

Ellington, C. P. (1984), 'The Aerodynamics of Hovering Insect Flight. II. Morphological Parameters', *Philos. Trans. R. Soc. B* **305**(1122), 17–40.

Fry, S. N., Sayaman, R. and Dickinson, M. H. (2003), 'The aerodynamics of free-flight maneuvers in Drosophila.', *Science* **300**(5618), 495–8.

Fry, S. N., Sayaman, R. and Dickinson, M. H. (2005), 'The aerodynamics of hovering flight in Drosophila', *J. Exp. Biol.* **208**, 2303–2318.

Hedrick, T. L. (2011), 'Damping in flapping flight and its implications for manoeuvring, scaling and evolution', *J. Exp. Biol.* **214**(24), 4073–4081.

Hedrick, T. L., Cheng, B. and Deng, X. (2009), 'Wingbeat Time and the Scaling of Passive Rotational Damping in Flapping Flight', *Science* **324**, 252–255.

Hedrick, T. L. and Robinson, A. K. (2010), 'Within-wingbeat damping: dynamics of continuous free-flight yaw turns in Manduca sexta.', *Biol. Lett.* **6**(3), 422–5.

Lentink, D. and Dickinson, M. H. (2009), 'Rotational accelerations stabilize leading edge vortices on revolving fly wings', *J. Exp. Biol.* **212**, 2705–2719.

Maeda, M., Gao, N., Nishihashi, N. and Liu, H. (2010), 'A Free-Flight Simulation of Insect Flapping Flight', *J. Aero Aqua Bio-mechanisms* **1**(1), 71–79.

Ramamurti, R. and Sandberg, W. C. (2007), 'A computational investigation of the three-dimensional unsteady aerodynamics of Drosophila hovering and maneuvering.', *J. Exp. Biol.* **210**(Pt 5), 881–96.

Ristroph, L., Bergou, A. J., Ristroph, G., Coumes, K., Berman, G. J., Guckenheimer, J., Wang, Z. J. and Cohen, I. (2010), 'Discovering the flight autostabilizer of fruit flies by inducing aerial stumbles', *Proc. Natl. Acad. Sci. U. S. A.* **107**(11), 4820–4824.

Sunada, S., Hatayama, Y. and Tokutake, H. (2010), 'Pitch, Roll, and Yaw Damping of a Flapping Wing', *AIAA J.* **48**(6), 1261–1265.

Wu, J. H., Zhang, Y. L. and Sun, M. (2009), 'Hovering of model insects: simulation by coupling equations of motion with Navier-Stokes equations.', *J. Exp. Biol.* **212**, 3313–3329.

Chapter 3

Flapping flight with ground effect: fruit fly hovering

3.1 Introduction

Hovering is a miracle of insects that is observed for all sizes of flying insects. Insects fly by flapping their wings to create lift and thrust forces simultaneously. Flapping-wing aerodynamics associated with insect flight prominently features unsteady motions at an intermediate Reynolds number, which is normally characterized by large-scale vortex structures, complicated flapping-wing kinematics, and flexible wing structures (Shyy et al., 2013). One of the challenging problems in uncovering aerodynamic mechanisms in insect flight is to answer a central question of how the complicated wake topology is generated and how it correlates with the aerodynamic force generation.

Studies on unsteady flapping-wing aerodynamics of a single or a paired wing model in hovering and/or forward flight have been the main subject until recently, which have been done either experimentally with robotic insect wing models or real insect or bird wings, or computationally with numerical wing models (Shyy et al., 2013). However, there has been little focus on the aerodynamic characteristics when an animal is flying close to the ground, i.e. takeoff, landing, or hovering just above the ground or leaves e.g. for feeding nectar. In the previous studies of flapping wing in ground effect, Gao & Lu used two-dimensional numerical simulation for low Reynolds number regime ($\mathrm{Re} = 100$, Gao et al., 2008; Gao and Lu, 2008) and Truong et al. used robotic flapper for a beetles wing (Truong, Byun, Kim, Yoon and Park, 2013; Truong, Kim, Kim, Park, Yoon and Byun, 2013). Both of the studies reported increase in vertical force. Also, Dickinson et al. reported the augmentation of force in robotic flapper (See ref. 25 of Dickinson et al., 1999). In these works, however, bodies of the insects were neglected.

In a rotorcraft in ground effect, there is a high-pressure region on the lower side of fuselage which somewhat compensates the vertical drag or so-called download6,7). We therefore hypothesized that in hovering flights in ground effect by flapping wings, bodies may play some role in the vertical force production. To investigate the body effect, we have carried out a three-dimensional computational fluid dynamic study on the hovering of a model fruit fly (Drosophila melanogaster) in ground effect (IGE) and out of ground effect (OGE) where the model insect is composed of a body and two wings. Comparison between IGE and OGE results revealed that a specific positive pressure region observed on the lower side of the body is responsible for a pronounced increase in the vertical force in the IGE hovering.

3.2 Methods

3.2.1 Numerical model and computational conditions

The computational fluid dynamic method used in this chapter is essentially the same as that found in the previous chapter, with marked difference that the whole body is now fixed in space. Also, the bottom boundary condition has changed to introduce the virtual ground in the case of IGE computation.

For this this study $P_{\text{body}} = 0$ because body is tethered and $v_{\text{surf,body}} = 0$. Also note that the force and power are given in dimensional forms. Details of the flow solver can be found elsewhere (Liu, 2009).

The computational conditions are taken almost the same as those by Aono et al. (Aono et al., 2008) but with some modifications with consideration of the ground. Instead of an O-O type spherical grid, in this study we employed a Cartesian grid as the background grid, in which a body grid and two wing grids are immersed in, as depicted in Fig. 3.1. Note that the outer boundary of the wing grid blocks are taken closer to the wing surfaces compared to the grid in Fig. 1B in Aono et al. (Aono et al., 2008) to ensure more accurate wing-wing interaction particularly when the wings are getting close to each other in pronation or supination. The outer boundary of the body grid block is also taken closer to the body surface than before, so as to avoid contacting or protruding from the ground surface. In the global grid block, the grids are clustered to the flyer blocks (Fig. 3.1A and B). For the IGE computation, the grids close to the bottom boundary are further clustered to the ground surface to better resolve the boundary layer (Fig. 3.1B).

Two computations were performed: in ground effect (IGE) and out of ground effect (OGE). The model parameters are summarized in Table 3.1. The height h of the model fly measured at wingbase from the bottom boundary is normalized by the wing length R as h/R, which is set to 5.2 for OGE while 0.8 for IGE. For the bottom boundary in the OGE computation, zero gradient conditions are taken for velocities and pressure to avoid any possible influence from the ground. For IGE, the bottom boundary is treated as a solid wall with zero pressure gradient condition. For all the other outer boundaries of

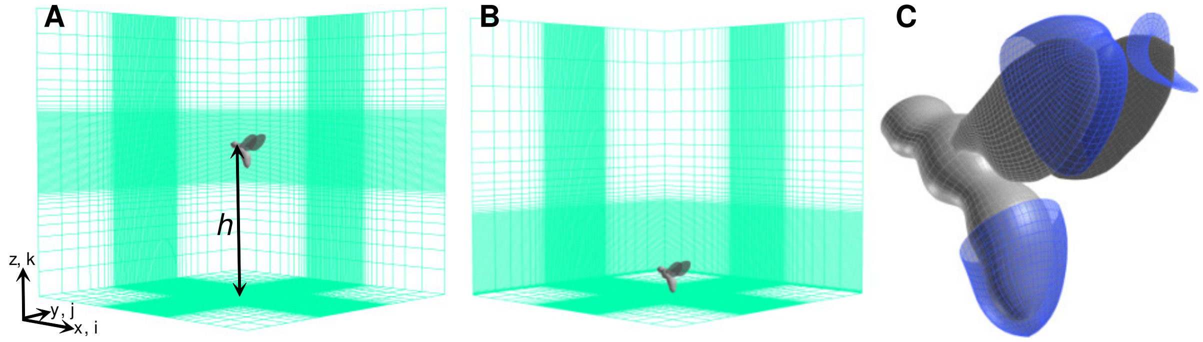

Figure 3.1. Grid systems. Global grid blocks for (A) OGE and (B) IGE computations, where h is the height from bottom outer boundary to the wing root of a fruit fly model. Grids of a fruit fly body and wings (C), where some portions of the outer boundaries for the body and left wing as well as a cross section for the right wing are colored in blue.

Table 3.1. Model parameters for both OGE and IGE computations.

Reynolds number, Re	136 ($= U_{\mathrm{ref}} c_{\mathrm{m}} / \nu$)
Reduced frequency, k	0.215
Wing length, R (mm)	2.39 [a]
Mean chord length, c_{m} (mm)	0.80 [b]
Reference velocity, U_{ref} (m/s)	2.55 ($= 2\Phi R f$)
Wingbeat frequency, f (Hz)	218 [a]
Wingbeat amplitude, Φ (rad)	2.44 [a]
Density of air, ρ (kg/m^3)	1.225
Kinematic viscosity of air, ν (m^2/s)	1.5×10^{-5} [a]
Stroke plane angle, χ (deg)	0 [a]
Body angle, β (deg)	45 [a]

[a] Aono et al., 2008.
[b] Hedrick et al., 2009.

the global grid, pressures are set to be initial (ambient) value and the zero velocity gradient conditions are taken. At the interfaces of the local and global grid blocks, velocities and pressures are interpolated and transferred each other (Liu, 2009). The body angle, the stroke plane angle (Table 3.1) and the wing kinematics (Aono et al., 2008) were set to be the same in the two cases. Note that the height ($h/R = 0.8$) chosen for the IGE computation is the lower limit to ensure the sufficient clearance between the body grid outer boundary and the ground. Any further reduction in height requires a manipulation in body angle or body shape.

The pressures p shown in the following sections are all the dimensionless gauge pressure. A gauge pressure is the deviation from ambient pressure and this is further normalized with $\rho_{\mathrm{air}} U_{\mathrm{ref}}^2 (= 7.94\mathrm{Pa})$. For example, $p = 0$ in the pressure contour is the same value as the ambient pressure, and $p = -1.0$ is the 7.94 Pa lower than the ambient.

3.2.2 Validation

The grid size and the number of grid points were carefully selected after a test to ensure sufficiently qualified grids as well as a reasonable computational time. The global grid block is a cube with a side 10 times the wing length (10R). The number of grid points in $i \times j \times k$ directions are: global grid, $89 \times 97 \times 93$; body grid, $45 \times 45 \times 9$; and right and left wing grids, $49 \times 49 \times 11$ each.

The influence of the grid resolution on the computational results were investigated by further introducing a fine grid system with a global grid of $161 \times 141 \times 127$, a body grid of $61 \times 61 \times 9$, and wing grids of $65 \times 65 \times 11$ each. The computations with the fine grids for both OGE and IGE conditions were carried out up to five wingbeat cycles. While the fine grid (Fig. 3.2A, open symbols) shows slightly greater values in vertical force compared to the coarse grid (Fig. 3.2A, filled symbols), it seems that the values in the two grid resolutions are converging. Also the vertical force ratios between IGE and OGE defined as ($F_{\mathrm{z,ave,IGE}}/F_{\mathrm{z,ave,OGE}}$) is almost the same (Fig. 3.2B: red filled triangles, coarse grids; green open triangles, fine grids). From the results of the coarse grids, it is seen that achieving the minimum stroke to stroke variation in vertical force takes a long time (ten to twenty wingbeat cycles, see the next section). Since the finer grids are computationally more expensive, the coarse grid system was therefore chosen for the following investigation of the forces, powers, and flow visualizations.

3.3 Results and discussion

3.3.1 Mean aerodynamic forces and power

Wingbeat cycle-averaged vertical forces are plotted in Fig. 3.2 Blue filled squares and black filled circles represent IGE and OGE, respectively. It is seen that the vertical force in the IGE case shows larger magnitude than the OGE case in any wingbeat cycles. Also, in both cases it is observed that the vertical force has a strong peak in the first wingbeat cycle due to the unsteady effect. It is also seen that the time-averaged vertical force reached a plateau by around 10 wingbeat cycles in the case of OGE. In contrast, it took approximately twice the time in the case of IGE. Note that the vertical forces in both OGE and IGE cases are always greater than the body weight of the model fruit fly (= 9.41 μNAono et al. (2008)).

As shown in Table 3.2, for the 20th wingbeat cycle, the IGE case shows an 8.5% increase in the vertical force ($F_{\mathrm{z,ave}}$) but a slight (1.6%) decrease in the aerodynamic power (P_{ave}) compared to the OGE case, which results in an approximately 10% improvement in the vertical force-to-power ratio ($F_{\mathrm{z,ave}}/P_{\mathrm{ave}}$). On the other hand, the horizontal forces are more than three orders magnitude smaller than the vertical forces in both OGE and IGE. It may be presumed that the real fruit fly likely take the advantage of

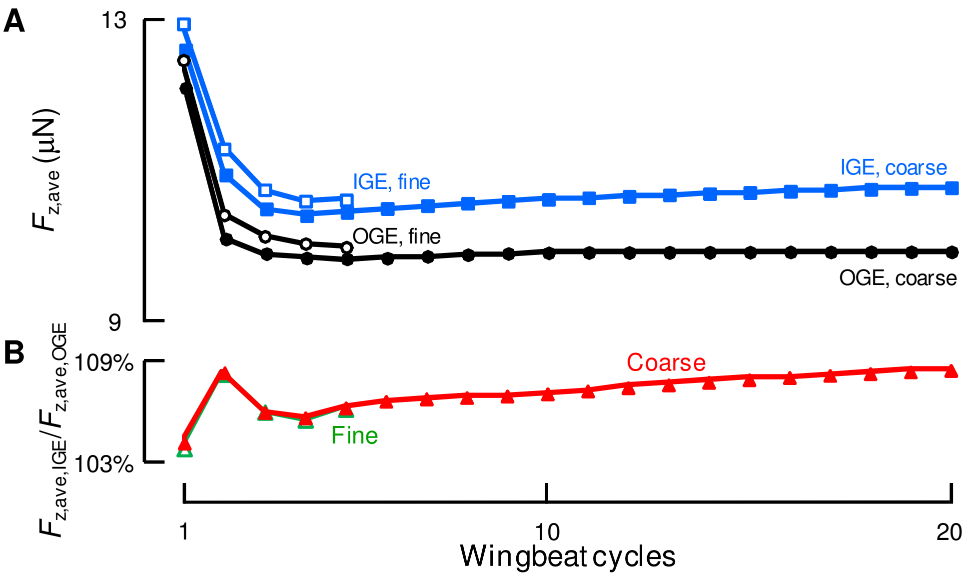

Figure 3.2. History of wingbeat-cycle averaged vertical forces including the comparison between fine and coarse grids. In A, open symbols are for fine grids and filled symbols are coarse grids; black circles and blue squares are for OGE and IGE, respectively. In B, the relative vertical force ratios between IGE and OGE are illustrated for coarse grids (red filled triangles) and fine grids (green open triangles).

this bonus in the $F_{\mathrm{z,ave}}/P_{\mathrm{ave}}$ in ground effect for e.g. a reduction in metabolic rate during hovering by adjusting the wing kinematics, or an augmentation of the force during the early phases of takeoff.

It is seen that the vertical force generated by wings in the IGE condition was merely 6.7810-8 N larger than in the OGE (Table 3.3), which is less than one percent improvement from OGE. This indicates that the wings are essentially out of ground effect. In fact, in the flapping wing experiment (single wing, without body) by Truong et al. Truong, Byun, Kim, Yoon and Park (2013), the vertical force exhibited a prominent increase when the wing is at $h/R = 0.5$ or 0.6 but no significant increase at $h/R = 0.72$ or above. Even though the wing shape, the wing kinematics and the Reynolds number are different from our current study, this is very much consistent with our results at h/R = 0.8.

In the OGE case, obviously the body shows negligible influence on the overall vertical force (Table 3.4, $F_{\mathrm{z,ave,wings}}$). In the IGE case, however, the body generates 7.79×10^{-7} N more vertical force compared to the OGE case (Table 3.4, $F_{\mathrm{z,ave,body}}$), one order of magnitude greater than the increase found in the wings. Thus, it is obvious that the pronounced increase in the overall vertical force is mainly due to the body rather than the wings.

Similarly to the total horizontal forces, the horizontal forces on the body or on the wings do not show substantial differences between OGE and IGE. Although the drag variation on each wing when in ground effect is of some interest, it is beyond the scope of the present study. Instead, in the following sections we will pay our attention mainly to the issues associated with the vertical forces on the body.

Table 3.2. Comparison of aerodynamic force components and power between OGE and IGE, each averaged for the 20th wingbeat cycle ($19.0 < t/T < 20.0$). The ratio of vertical force to power is also compared.

Model	$F_{\mathrm{x,ave}}$ (N)	$F_{\mathrm{y,ave}}$ (N)	$F_{\mathrm{z,ave}}$ (N)	P_{ave} (W)	$F_{\mathrm{z,ave}}/P_{\mathrm{ave}}$ (N/W)
OGE	-9.53×10^{-9}	-9.70×10^{-12}	9.91×10^{-6}	2.39×10^{-5}	0.415
IGE	9.50×10^{-8}	2.27×10^{-10}	1.08×10^{-5} (8.5%)	2.35×10^{-5} (-1.6%)	0.458 (+10%)

The values in the parentheses are the relative increases in the IGE compared to the results in the OGE.

Table 3.3. Comparison of force components generated by wings between OGE and IGE, each averaged for the 20th wingbeat cycle. The increases in the IGE from OGE are also shown.

Model	$F_{\mathrm{x,ave,wings}}$ (N)	$F_{\mathrm{y,ave,wings}}$ (N)	$F_{\mathrm{z,ave,wings}}$ (N)
OGE	-4.29×10^{-8}	-5.08×10^{-11}	9.91×10^{-6}
IGE	-7.88×10^{-8}	-5.00×10^{-10}	9.98×10^{-6}
IGE-OGE	-3.59×10^{-8}	5.51×10^{-10}	6.78×10^{-8}

3.3.2 Instantaneous aerodynamic forces and power

As depicted in Fig. 3.3C, compared to hovering out of ground effect, the fly in ground effect produces slightly greater vertical force in the several time instances while almost no change is observed in horizontal forces (Fig. 3.3A, B) or in the aerodynamic power of the wings (Fig. 3D). Furthermore, when separating the force histories into the body and wings (Fig. 3.4), we find that the body in ground effect keeps producing positive (upward) vertical force throughout the wingbeat period whereas the body out of ground effect apparently exhibits slight positive vertical force at downstroke but negative (downward) vertical force at late upstroke (Fig. 3.4C). On the other hand, the vertical forces due to the wings show marginal discrepancy between IGE and OGE except for the slight increase at the early downstroke (Fig. 3.4F).

The differences in vertical force between IGE and OGE for body and wings were further quantified separately, which are plotted in Fig. 3.5A-B. The absolute difference in the instantaneous vertical force due to wings in ground effect (Fig. 3.5A, blue dotted line) does have a feature of time-variation but shows a very small cycle-averaged value as shown in Table 3.3. The difference in the vertical forces in the body, however, keeps a large positive value throughout the wingbeat period, which obviously is responsible for

Table 3.4. Comparison of force components generated by body between OGE and IGE, each averaged for the 20th wingbeat cycle. The increases in the IGE from OGE are also shown.

Model	$F_{\mathrm{x,ave,body}}$ (N)	$F_{\mathrm{y,ave,body}}$ (N)	$F_{\mathrm{z,ave,body}}$ (N)
OGE	3.33×10^{-8}	4.11×10^{-11}	-2.46×10^{-9}
IGE	1.74×10^{-7}	-2.72×10^{-10}	7.77×10^{-7}
IGE-OGE	1.40×10^{-7}	-3.14×10^{-10}	7.79×10^{-7}

the most of the difference in vertical forces between IGE and OGE.

Furthermore, with considering the low Reynolds number effect we evaluated the influence of inviscid and viscous force components contributing to the vertical forces on the body and on the wings (Fig. 3.5B). For wings, obviously most of the vertical force is coming from the inviscid (pressure) component. For body, apparently both inviscid and viscous force components maintain the positive value, although the inviscid force component is always larger. This can be further illustrated by means of the pressure distributions on the body surface as discussed in the following section.

3.3.3 Flow visualization and correlations with aerodynamic force augmentation

Fig. 3.6 illustrates the wingbeat cycle-averaged pressure contours on the body of IGE and OGE as well as the difference ($p_{\mathrm{IGE}} - p_{\mathrm{OGE}}$) for the 20th wingbeat cycle. It is seen that a pronounced difference lies on the ventral surface of the body as well as the tip of the abdomen, where high pressure regions are observed; the head in IGE shows slightly lower pressures than OGE, which may also contribute to the vertical force. Here the high pressures on the ventral side can explain the increase in Fx,ave,body, i.e. increase in the backward force component (Tables 3.2, 3.4 and Fig. 3.4A). This unbalance in the horizontal forces may be coped with by altering (decreasing) its body angle in the real-life situation, even though there would be a limitation to the change of body angle because the backside of the body may interfere with the trailing edges of the wings. In fact, the margin is about 30 degrees if the wing kinematics is unchanged.

In Fig. 3.7 the body pressure contours are plotted at ten instances for OGE and IGE. It is seen that the pressures on a certain region are not stable in strength but time-varying. Nevertheless, compared to OGE the abdominal tip in IGE always shows a high-pressure region. This is corresponding to the time-averaged pressures as shown in Fig. 3.6. Similarly, at the joints between head and thorax as well as thorax and abdomen, relatively high-pressure regions are also observed, again showing similar tendency as in Fig. 3.6A.

To further provide an overall image of correlations between flow fields and vertical force production in terms of velocities and pressures we plotted pressure contours and velocity vectors around the hovering model fruit fly in Fig. 3.8A-J. A high-pressure region can be found close to the ground throughout the wing strokes (Fig. 3.8, transparent red surfaces and the pressure contours on the ground). At a glance, the body seems to be effectively lifted up on this high pressure air cushion. The contacting portions with the air cushion appear to have high pressures.

How is this high-pressure region created? Specifically, why this region is observed mainly under the

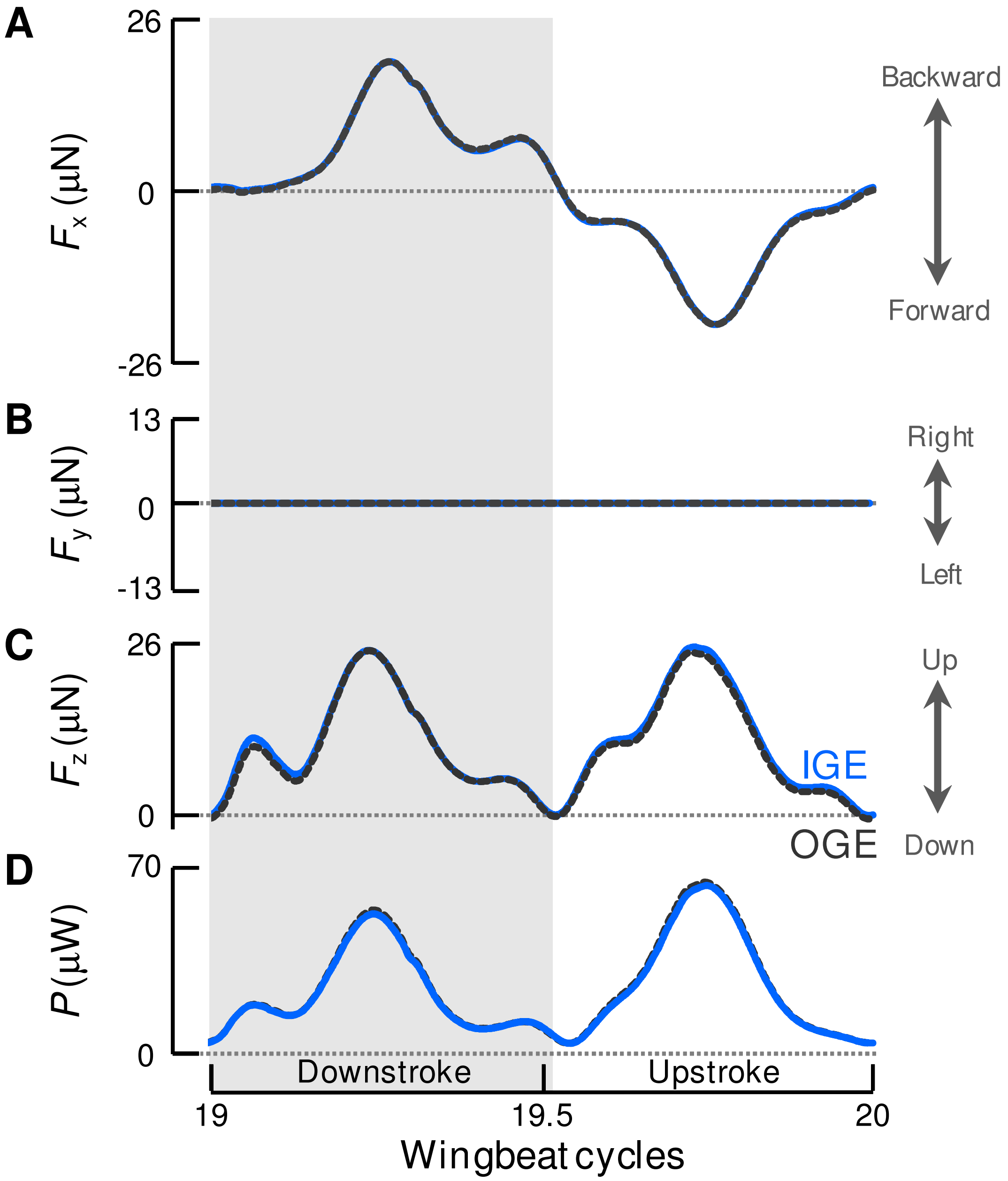

Figure 3.3. Time courses of total aerodynamic forces (A-C: F_x, F_y, F_z) and powers (D) during the 20th wingbeat cycle for IGE (blue solid lines) and OGE (black dashed lines), respectively. The shaded region of downstroke corresponds to $0 \leq t/T \leq 19.54$.

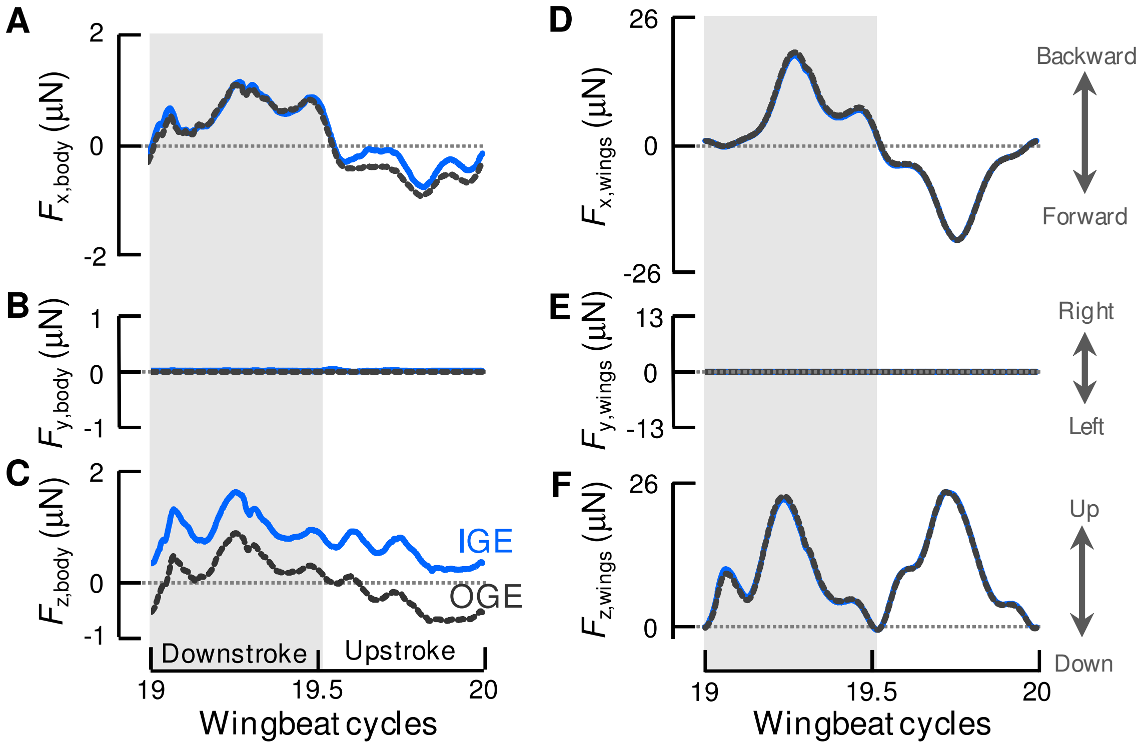

Figure 3.4. Time courses of aerodynamic forces in IGE (blue solid lines) and OGE (black dashed lines) for body (A-C: F_x, F_y, F_z) and wings (D-F: F_x, F_y, F_z) during the 20th wingbeat cycle.

wings and the body but not beneath the wing roots (see e.g. Fig. 3.8F or G)? We believe the downwash is the answer. The downwashes induce by the flapping wings during down- and up-stroke (Fig. 3.8C, H, and I, white arrows) are forced to stagnate and change their directions to horizontal while they are approaching the ground.

This results in a significant reduction in the downward flow speed and pressure rise near the ground surface by converting the dynamic pressure into the static pressure. It is further seen that some of the deflected downward flows originally generated from right wing and left wing head to the center of the body from both sides, subsequently collide each other right under the body, thereby providing another pressure recovery. These are likely the main sources of the high pressure on the lower abdominal section, considering that this portion always exhibits higher pressure than the other part of the body (Fig. 3.8A, E, and J, also see Fig. 3.5A, red line). Moreover, portions of the flows at the center further form an upward flow, resulting in a fountain of the airflow, which eventually impinges against the lower side of the body and probably becoming an aid to the further pressure recovery. This whole process is sometimes termed as fountain effect in the rotary wing community (Watkinson, 2004) and is essentially how a hovercraft lift itself, but it has not been reported for the flapping wing flight before. Unlike hovercrafts, however, as clear from the pressure footprints on the ground in Fig. 3.8, in flapping wings the horizontal

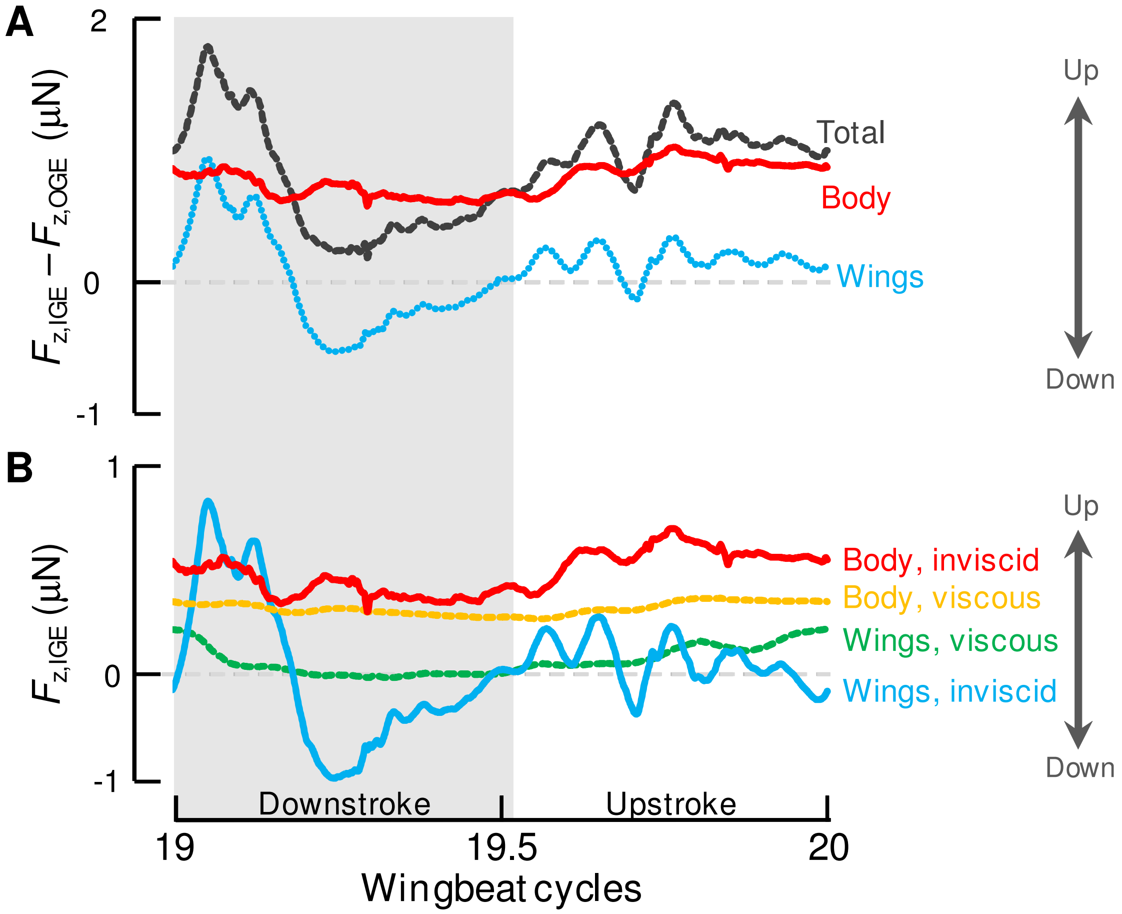

Figure 3.5. (A) Comparison of difference in vertical force between IGE and OGE during the 20th wingbeat cycle. Red solid line, body; blue dotted line, wings; and black dashed line, total vertical force. (B) Decomposition of the vertical forces into inviscid components (Solid lines), viscous components (dashed lines); body (red lines), and wings (blue lines).

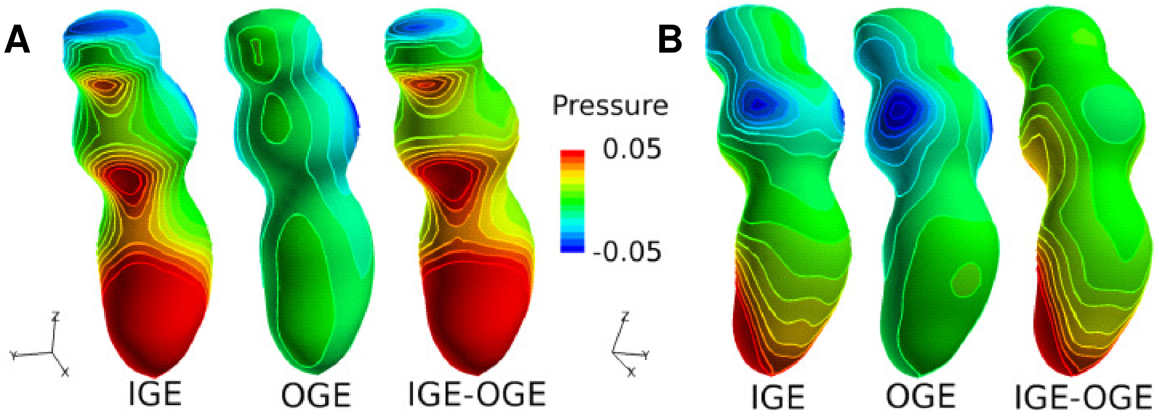

Figure 3.6. Comparison of wingbeat cycle-averaged pressures on body surface between IGE (left) and OGE (middle). The pressures are averaged during the 20th wingbeat cycle (over 50 time frames). Note that the difference between IGE and OGE is also shown (right). Ventral (A) and dorsal (B) sides are shown.

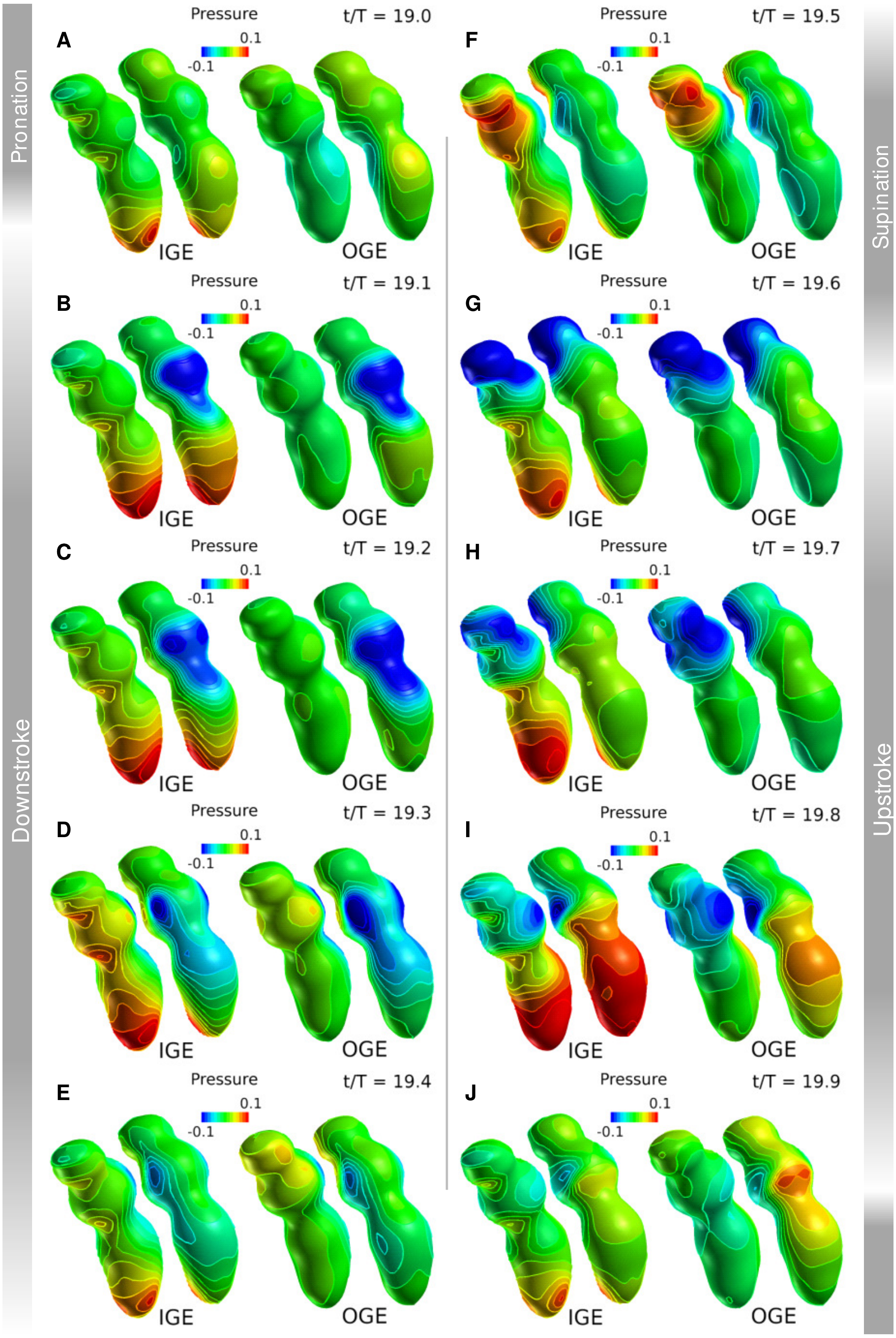

Figure 3.7. Comparison of pressure contours between IGE and OGE during the 20th wingbeat cycle. The ribbons on sides present approximately stroke phases.

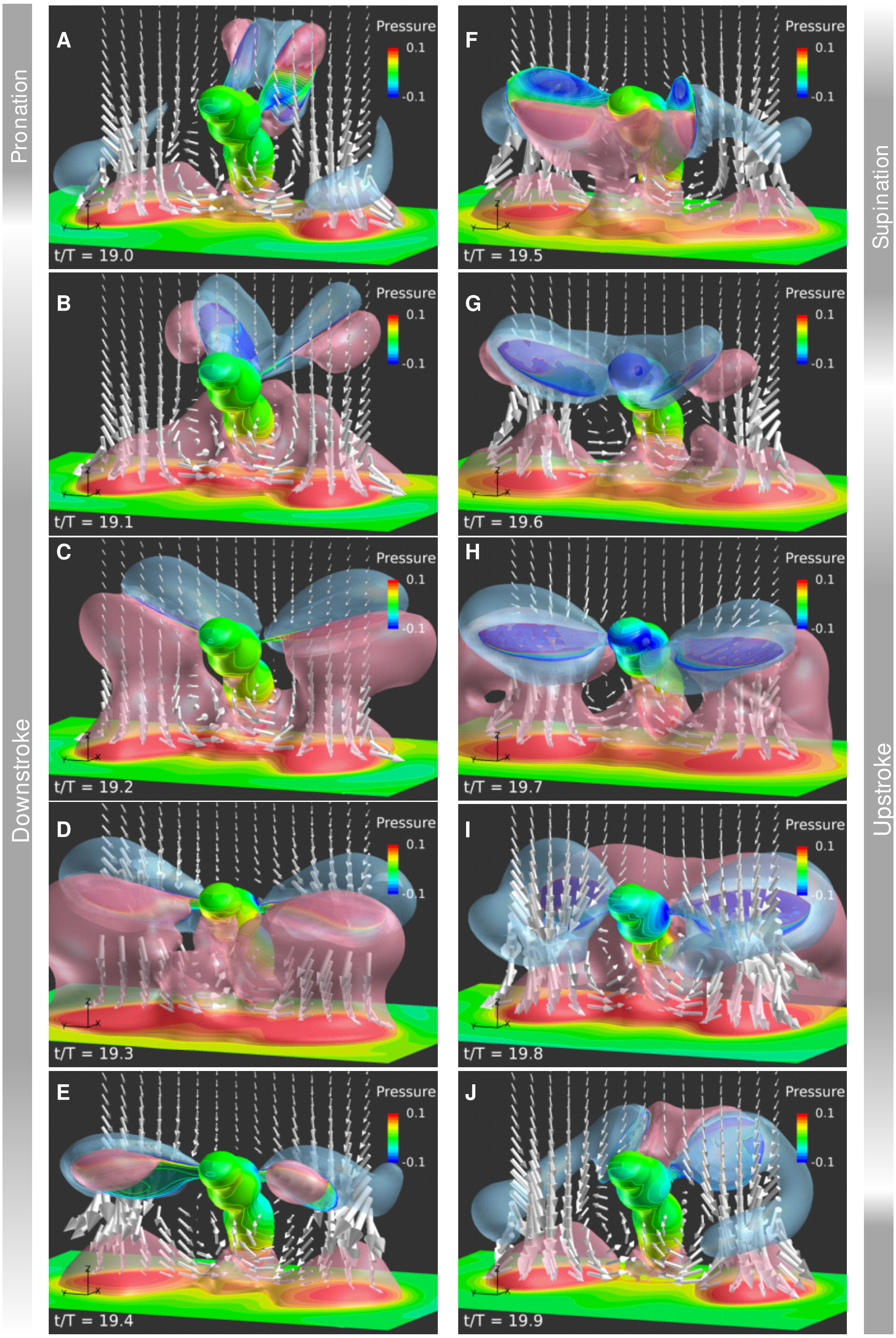

Figure 3.8. Front view of visualized flows fields around a hovering model fruit fly in the IGE computation during the 20th wingbeat cycle. Pressure contours, iso-pressure surfaces (transparent blue, at -0.1, and transparent red, at +0.05), and velocity vectors at the yz-plane cutting through the wing bases (white arrows).

location of the downwashes fluctuate as the wings move back and forth. Nevertheless, the directions and the intensities of velocity vectors under the ventral side of the body seem to remain rather stable (Fig. 3.8). Therefore, the above-mentioned mechanism is probably responsible for creating the time-averaged high pressure region on the ventral side of the body (Fig. 3.6A).

It should be also noted that there found several other features in the body surface pressure contours, although they are not directly correlated to the vertical force increase in the IGE because these features are common in the two cases. The low pressure on the back of the body at the early-downstroke (Fig. 3.7B), high pressure on the head at supination (Fig. 3.7F), low pressure on the head just after the supination (Fig. 3.7G), and high pressure on the back of the body at late-upstroke (Fig. 3.7J and I), all seem to be due mainly to the direct influence from the high or low pressure regions on the wings (see Fig. 3.8B, F, G, J, and I, respectively). They possibly explain the within-wingbeat variation in $F_{\mathrm{x,body}}$ and $F_{\mathrm{z,body}}$ (Fig. 3.4A, C). In addition, the low pressure regions on the both sides of the body (Fig. 3.7C-E, G-I) appear presumably due to the wingroot vortices which are probably only found in the specific wing planforms (i.e. narrow near the wingroot). The point is that these pressure regions are available in both IGE and OGE computations and should not contribute to the overall force difference, although the intensities of which slightly differs. This can be confirmed by the time-averaged contour difference (Fig. 3.6A, B, right models).

3.4 Effect of ground clearance and body

More trials were made, exploring the effect of ground clearance (or height or altitude, h/R) and the existence of body on the increase in the vertical force. The result is summarized in Fig. 3.9. Open symbols are the normal fruit fly model with body and two wings, whereas the filled symbols are the model lacking the body, therefore there should be no fountain effect. The 'IGE model' mentioned until the previous section corresponds to the open orange diamond (normal model at $h/R = 0.8$). As mentioned in the Method section, further decrease in the height required the adjustment of the body angle, therefore in the red symbols ($h/R = 0.7$), the body angle decreased to 30 deg, which seems to be natural for an insect because when the fly is on the ground, the body angle would be nearly zero, i.e. the body axis is parallel to the ground. Since the bottom projection area of the body increased, the fountain effect should be stronger. The comparative study of the same body angle (30 deg) with larger height should be done for confirmation. Nevertheless, he increase in the vertical force at $h/R = 0.7$ is clearly seen even without body (red filled triangle compared to orange filled diamond). This indicates the wings do benefit from the ground effect, presumably due to the alteration of the circulation. Another interesting finding is the general trend of the normal fly model against hight is similar to the theoretical model of the thrust

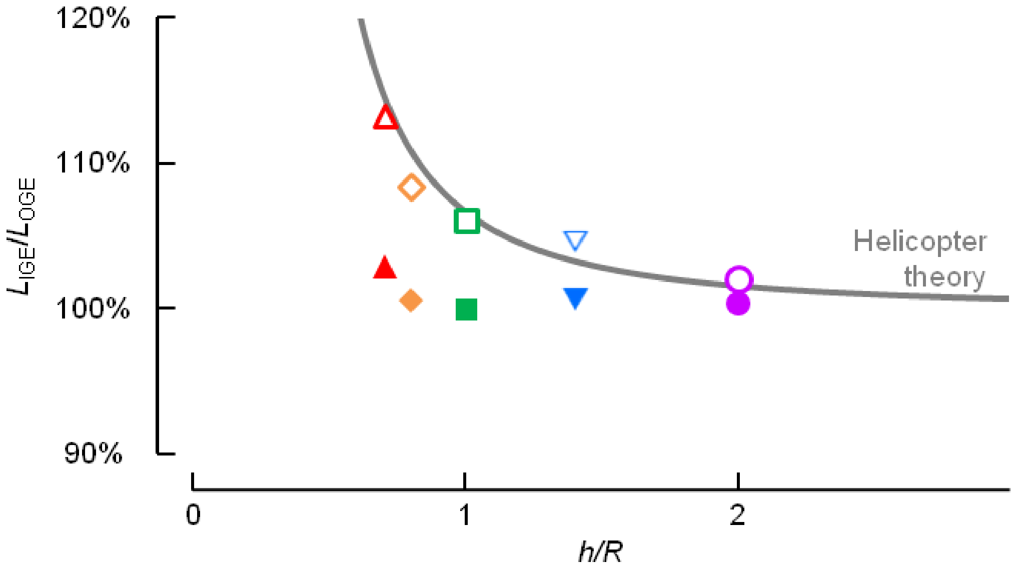

Figure 3.9. Diagram illustrating the relationship between the vertical force and the altitude (h/R) as well as the effect of body. Open symbols are the normal fruit fly model (body + wings) whereas the filled symbols are the model without body. Gray solid curve is derived from helicopter theory (Eq. 5.98 in Leishman, 2006).

(vertical force) in helicopter (Eq. 5.98 in Leishman, 2006). The coincidence may be just by chance, or partially so, because the theoretical calculation does not include fuselage (body) of the helicopter but only the rotor blades. Nevertheless, the good agreement of the theory with the measured data (Fig. 5.36 in Leishman, 2006) might imply the effect of fuselage may be approximated in the simple theory, in another word, the theory may be overestimation for the pure rotor blades but somehow matches with the whole-body force. The more extensive study on the fountain effect in the rotorcraft (especially in low Reynolds number regime) would be necessary for further discussion.

3.5 Concluding remarks

Ground effect in a hovering fruit fly in terms of aerodynamic force and power was explored by numerical simulation. It has been confirmed that a fly in ground effect (IGE) experiences greater vertical force compared to out of ground effect (OGE), provided that both the wing kinematics and body attitude are unchanged from the stable hovering at OGE. It was also found that the major contribution is from the presence of the body. Visualization of velocities and pressures unveiled that in the IGE computation, the wing-induced downwashes are vectored to horizontal direction due to the ground, and portions of which merge together under the body, together forming a high pressure region on the lower ventral side of the body. We believe that this mechanism usually termed as fountain effect in helicopter aerodynamics (Watkinson, 2004) is the main source of the vertical force enhancement in fruit fly hovering in ground effect. This mechanism may be applied to the development of flapping micro air vehicles (fMAVs) with a tailored fuselage shape to effectively and efficiently capture the high pressure air and deflected downwash during low altitude hovering, takeoff or landing.

We showed the wings are essentially out of ground effect at $h/R = 0.8$, but when a real fly is flying at $h/R < 0.8$, the wings may be benefited from the ground effect. However, in such a case the wing kinematics as well as the body attitude is fairly likely different from the OGE hovering (Fontaine et al., 2009). To provide concrete answers to these questions, we need to measure the real insects flights near the ground with sufficient precision not only for wing kinematics but also body shapes and postures, and carry out an extended study to clarify the influence of these parameters on the ground effect.

Also, we did not consider the force balance or moments in the present study. These cannot be ignored in the real situation but the treatment would not be easy because of the nonlinear coupling. The slightest changes in vertical position or body attitude would result in the increase or decrease of the intensity of the ground effect, which would provoke the alteration of aerodynamic force or moment again. Further investigations on this issue would provide insights into the passive stability or active control in the flapping flight near the ground.

References

Aono, H., Liang, F. and Liu, H. (2008), ‘Near- and far-field aerodynamics in insect hovering flight: an integrated computational study.’, *J. Exp. Biol.* **211**, 239–257.

Dickinson, M. H., Lehmann, F.-O. and Sane, S. P. (1999), ‘Wing Rotation and the Aerodynamic Basis of Insect Flight’, *Science* **284**(5422), 1954–1960.

Fontaine, E. I., Zabala, F. A., Dickinson, M. H. and Burdick, J. W. (2009), ‘Wing and body motion during flight initiation in Drosophila revealed by automated visual tracking.’, *J. Exp. Biol.* **212**, 1307–1323.

Gao, T., Liu, N.-s. and Lu, X.-y. (2008), ‘Numerical Analysis of the Ground Effect on Insect Hovering’, *J. Hydrodyn.* **20**(1), 17–22.

Gao, T. and Lu, X.-y. (2008), ‘Insect normal hovering flight in ground effect’, *Phys. Fluids* **20**(8), 087101.

Hedrick, T. L., Cheng, B. and Deng, X. (2009), ‘Wingbeat Time and the Scaling of Passive Rotational Damping in Flapping Flight’, *Science* **324**, 252–255.

Leishman, G. J. (2006), *Principles of Helicopter Aerodynamics with CD Extra*, 2nd editio edn, Cambridge University Press, New York.

Liu, H. (2009), ‘Integrated modeling of insect flight: From morphology, kinematics to aerodynamics’, *J. Comput. Phys.* **228**(2), 439–459.

Shyy, W., Aono, H., Kang, C. and Liu, H. (2013), *An Introduction to Flapping Wing Aerodynamics*, Cambridge University Press, New York.

Truong, T. V., Byun, D., Kim, M. J., Yoon, K. J. and Park, H. C. (2013), ‘Aerodynamic forces and flow structures of the leading edge vortex on a flapping wing considering ground effect.’, *Bioinspir. Biomim.* **8**(3), 036007.

Truong, T. V., Kim, J., Kim, M. J., Park, H. C., Yoon, K. J. and Byun, D. (2013), ‘Flow structures around a flapping wing considering ground effect’, *Exp. Fluids* **54**(7), 1575.

Watkinson, J. (2004), *The Art of the Helicopter*, Elsevier Butterworth-Heinemann, Oxford.

Chapter 4

Flapping flight with leg thrust: butterfly takeoff

4.1 Introduction

In this chapter, I investigate the takeoff of a butterfly. I chose this because the butterfly is interesting in that it uses both wings and legs during the initial phase of the takeoff. If there is no wing motion and pure jumping, there are tremendous number of works has already been done (and being done). I am interested in the fraction of the aerodynamic force and leg thrust force, as well as the timings of them.

There have been several studies on the butterfly aerodynamics (e.g. Brodsky, 1991; Dudley, 1991; Srygley and Thomas, 2002; Zheng et al., 2013) and at least one study dealing with the aerodynamics of butterfly takeoff (Sunada et al., 1993) but usually leg thrust is not taken into consideration. For birds, on the other hand, importance of leg thrust was pointed out as early as 1985 (Heppner and Anderson, 1985) and there are a few papers directly measured the leg thrust force with either with a perch (Heppner and Anderson, 1985; Bonser, Richard and Rayner, 1996; Tobalske, 2004) or a force plate (Earls, 2000), although I presume the use of force plate is not always a good idea because it could mistakingly measure the force due to downwash generated by the wings just above the plate, in which case the leg thrust could be overestimated by the positive aerodynamic pressure on the plate.

Recently a takeoff simulation of a butterfly focusing on leg thrust was published (Bimbard et al., 2013). However, the model used in their study is rather simple: there is no wing deformation and even no feathering angle included.

In this study, I measured the time-varying wing morphology during takeoff as well as the body motion with the aid of coworker (Shuhei Ozawa, a former Masters student). From the high speed video images the three dimensional shape of the wing at each time step is reconstructed. Two additional considerations are presented. Namely, ground effect and leg thrust. It may be predicted that both potentially have significant effects on the butterfly takeoff trajectory. The results showed that in the particular takeoff that concerned, the ground effect has almost negligible impact, whereas the leg thrust is producing several times larger vertical force than the wings, making it the one of the most important factors in the early stage of the takeoff.

4.2 Methods

4.2.1 Measurement of wing and body kinematics

A swallowtail butterfly (*Papilio xuthus*) was captured outside near Chiba University. The trailing edges were damaged and right tail streamer was lost during the capture and captive process (Fig. 4.1A). The measurement was done in the laboratory with low-light environment. When there is sunlight or artificial light the butterfly always exhibit strong tendency to fly towards the light therefore limiting the light was necessary. The butterfly was enclosed in a transparent box made of PMMA. Although transparency was necessary for the following photo recording, the insect cannot see the invisible walls and collides with the walls after the taking off, damaging the wings. Therefore the takeoff trials was unable to be repeated more than a few times for a specimen. No paintings on the wings were made. Instead, the pattern on the wings as well as three locations on the body were selected as the characteristic points (Fig. 4.1A, blue dots).

Three high speed video cameras (Phantom Miro eX4, Vision Research, USA) with resolution of 800 × 600 pixels each were placed approximately orthogonal to each other for maximizing the chance that each characteristic point is always visible by at least two cameras, which is the necessary for the three-dimensional reconstruction. The cameras were synchronized at 1,000 Hz. Data is stored in the flash memory in each camera and transferred to a Windows laptop PC via 100BASE-TX Ethernet. Tracking and three dimensional reconstruction of the characteristic points were carried out using commercial software (DIPP-Motion Pro, DITECT, Japan) as shown in Fig. 4.1C. After the photo-recording, the butterfly was killed and the masses of the body and each wing were measured.

4.2.2 Numerical simulation

An integrated flapping flight simulator is used as in Chapter 2, where the computational fluid dynamics (CFD) considering virtual ground and the simplified rigid body dynamics (sRBD) are coupled. The details of the solvers can be found in Appendices A and B. In this section, let me explain the special

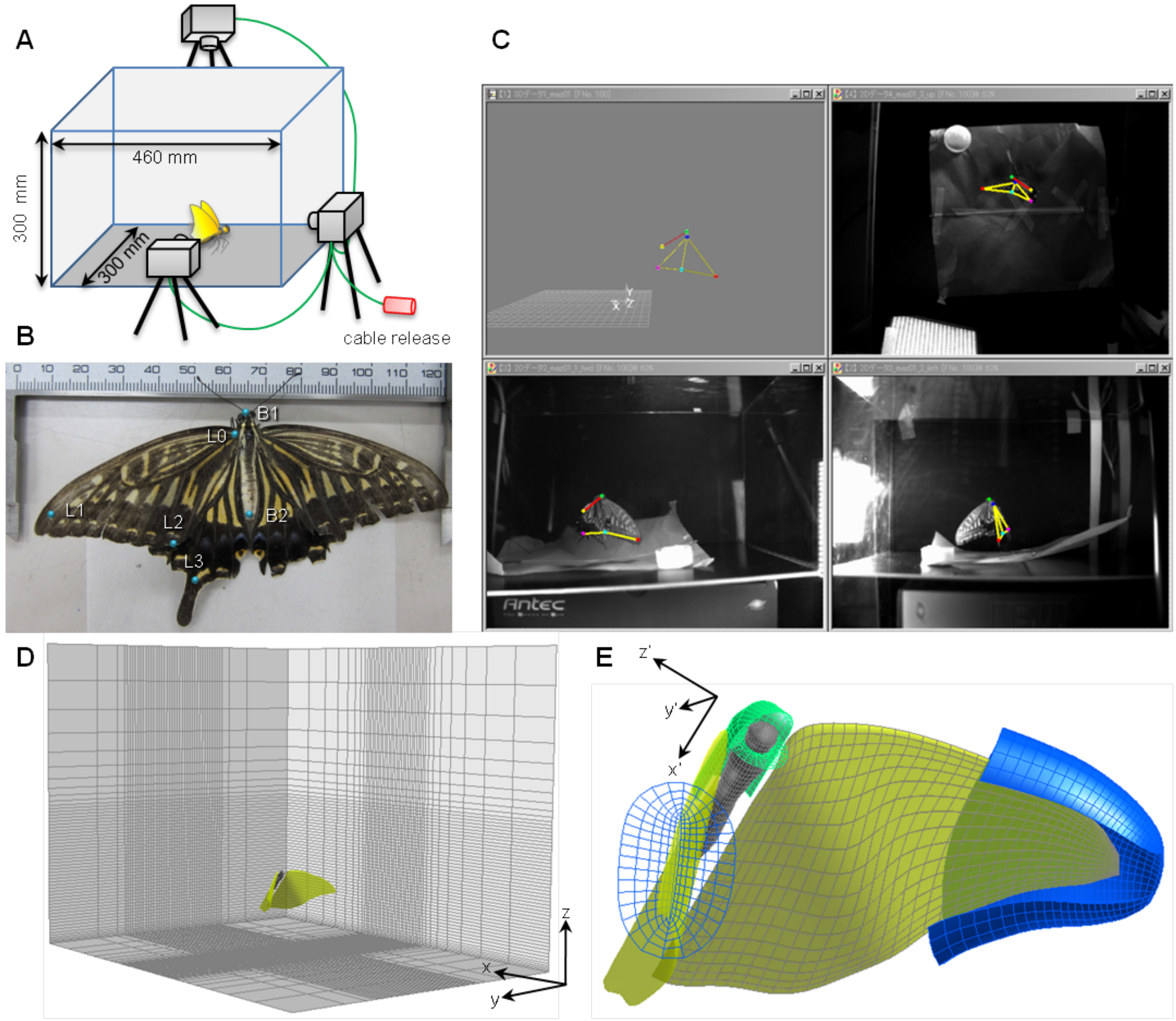

Figure 4.1. Takeoff measurement and grids for numerical simulation. (A) Measurement setup. The butterfly was placed in a acrylic box. Three synchronized high speed video cameras, together with three strobe LED lights (two infra-red lights and one white light, not drawn) were used. A cable release was pressed after the butterfly takes off, thereby saving the date of two seconds preceding the press. (B) The characteristic points (C) A time slice of the reconstruction process. Body (red line) and left wing (yellow lines) are reconstructed. (D) The overview of computation grids along with the coordinates of the inertial frame (the origin not shown). The clustered region of the background grid moves according to the body motion so that inner grid blocks (body and wings) are always kept inside of the clustered region. (E) The body and wing grids along with the coordinates of the principle axes of inertia frame. The origin of the coordinates is the total CG of the insect, which is not shown. The outer boundaries and the structure of body (green) and wing (blue) grids are also illustrated. All the C, D and E are showing the same time slice $t/T = 0.76$.

treatments necessary for butterfly takeoff.

Modification to the simplified rigid body dynamics solver

For a single rigid body where there is no contact with the ground, the equations of motion can be written as

$$M\dot{\mathbf{V}} = \mathbf{F}_{\text{aero}} + \mathbf{F}_{\text{grav}}, \tag{4.1}$$

$$\mathbf{J}'\dot{\mathbf{\Omega}}' + \tilde{\mathbf{\Omega}}'\mathbf{J}'\mathbf{\Omega}' = \mathbf{N}'_{\text{aero}}. \tag{4.2}$$

which are the same as eqs. B.1 and B.2. The terms with primes are in the body frame, defined in Fig. 4.1. The applied force is composed of aerodynamic force $\mathbf{F}_{\text{aero}}$ and gravitational force $\mathbf{F}_{\text{grav}} = [0, 0, F_{\text{grav,z}}]^T$; and the applied torque around the center of mass is the aerodynamic torque $\mathbf{N}'_{\text{aero}}$. For the present computation, they are modified as follows:

$$M\dot{\mathbf{V}} = \mathbf{F}_{\text{aero}} + \mathbf{F}_{\text{grav}} + \mathbf{F}_{\text{GR}} + \mathbf{F}_{\text{leg}}, \tag{4.3}$$

$$\mathbf{J}'\dot{\mathbf{\Omega}}' + \tilde{\mathbf{\Omega}}'\mathbf{J}'\mathbf{\Omega}' = \mathbf{N}'_{\text{aero}} + \mathbf{N}'_{\text{leg}}. \tag{4.4}$$

where $\mathbf{F}_{\text{GR}} = [0, 0, F_{\text{GR,z}}]^T$ is ground reaction force (GRF), $\mathbf{F}_{\text{leg}} = [F_{\text{leg,x}}, 0, F_{\text{leg,z}}]^T$ is leg thrust force vector, and $\mathbf{N}'_{\text{leg}} = [0, N'_{\text{leg,y}'}, 0]^T$ is the leg thrust pitching torque in the body frame.

4.2.3 Butterfly model

The base wing gird is generated from the planform of the wings where ipsilateral forewing and hindwing are combined together (Fig. 4.1A and B). The wing geometry is assumed to be symmetric and the left tail streamer was neglected. The base wing grid is then deformed using the movement of the characteristic points along time (Fig. 4.1E) with the aid of Toshiyuki Nakata, a former PhD student. See Nakata et al. (Nakata et al., 2011) for the details of the method. The body is simplified as a rigid, non-deforming body generated from the planform view (4.1A and B). The insect grids are located close to the bottom surface of the background grid (Fig. 4.1D). No-slip boundary condition is applied to the bottom surface, making it a virtual ground. Major parameters for these two models are presented in the Table 4.2.

One notable thing here is the x'-component of the wingbeat cycle-averaged moment of inertia, which is the moment of inertia around the body axis. Since a body of an insect has a cylindrical shape this value is usually very small compared to the other axes: for example, the model fruit fly in Chapter 2, x'-component is less than a quarter of the other axes (Table 2.1). However, for the butterfly in the present case, it is more than half of the other axes (Table 4.2). This is the consequence of the large wing masses-to-body mass ratio of the butterfly.

Ground reaction force

The ground reaction force (GRF) $\mathbf{F}_{\mathrm{GR}}$ was introduced. This force has the z-component in the inertial frame only, i.e. $\mathbf{F}_{\mathrm{GR}} = [0, 0, F_{\mathrm{GR,z}}]^T$. The instantaneous magnitude $F_{\mathrm{GR,z}}$ for given time is defined as

$$F_{\mathrm{GR,z}} = -(F_{\mathrm{aero,z}} + F_{\mathrm{grav,z}} + F_{\mathrm{leg,z}}) \quad \text{while} \quad F_{\mathrm{aero,z}} + F_{\mathrm{grav,z}} + F_{\mathrm{leg,z}} < 0 \tag{4.5}$$

where F_{aero}, $F_{\mathrm{grav,z}}$, and $F_{\mathrm{leg,z}}$ are the z-components of aerodynamic force, gravitational force, and leg thrust force (see next subsection), respectively. The ground reaction force acts to cancel out the gravitational acceleration in the negative z-axis, preventing the butterfly model falls from the virtual ground.

Leg thrust model

The leg thrust force $\mathbf{F}_{\mathrm{leg}}$ and leg thrust torque $\mathbf{N}'_{\mathrm{leg}}$ are modeled as follows. First, the flight is assumed to be bilaterally symmetric about sagittal plane therefore force has only the x- and z-components and torque has only the y'-components:

$$\mathbf{F}_{\mathrm{leg}} = \begin{bmatrix} F_{\mathrm{leg,x}} \\ 0 \\ F_{\mathrm{leg,z}} \end{bmatrix}, \ \mathbf{N}'_{\mathrm{leg}} = \begin{bmatrix} 0 \\ N'_{\mathrm{leg,y'}} \\ 0 \end{bmatrix}. \tag{4.6}$$

Each of force or torque component is modeled as a sinusoidal wave. Since direct measurement of the butterfly's leg thrust is not available, I chose a sinusoidal wave mainly because of its simplicity. Also, from the leg thrust measurements of fruit fly (lowest row in Fig. 7A of (Card and Dickinson, 2008)) or birds (Fig. 2A of Bonser, Richard and Rayner, 1996, Fig. 8 of Earls, 2000), sinusoidal may be a reasonable approximation.

After several preliminary trials, I have found the force is better sought using the polar coordinates, i.e. instead of changing x- and z-components independently and arbitrary, decompose the force vector into magnitude and angle. This is because the flight direction of the butterfly seemed to be largely dependent upon the angle but independent of force magnitude or torque. Thus, I hereafter call this angle a launch angle θ_{thrust}. If I arbitrary change either x- or z-component of leg thrust force, in every trial the launch angle varies, consequently finding the best combination takes a large number of trials. I therefore first find the launch angle and then fixed it while varying force magnitude and torque. In general, force magnitude determines how far the butterfly goes (overshoot or undershoot compared to the measured trajectory) and pitching torque determines the history of body angle, although they are not totally independent but in reality a slight coupling observed. The leg thrust force and torque are therefore written as

$$F_{\mathrm{leg,mag}} = A_{F\mathrm{leg}}(1-\cos\theta_{\mathrm{leg}})/2 \tag{4.7}$$

$$F_{\mathrm{leg,x}} = F_{\mathrm{leg,mag}}\cos\theta_{\mathrm{thrust}} \tag{4.8}$$

$$F_{\mathrm{leg,z}} = F_{\mathrm{leg,mag}}\sin\theta_{\mathrm{thrust}} \tag{4.9}$$

$$N'_{\mathrm{leg,y'}} = A_{N'\mathrm{leg}}(1-\cos\theta_{\mathrm{leg}})/2 \tag{4.10}$$

where $A_{F\mathrm{leg}}$ and $A_{N'\mathrm{leg}}$ are the amplitude of leg thrust force in the inertial frame and the amplitude of y-component of the leg thrust torque in the body frame, respectively. The function $theta_{\mathrm{leg}}$ determines the temporal location of the leg thrust as

$$\theta_{\mathrm{leg}} = \frac{2\pi(\hat{t}-\hat{t}_{\mathrm{leg,begin}})}{\hat{t}_{\mathrm{leg,end}}-\hat{t}_{\mathrm{leg,begin}}} \quad \text{if} \quad \hat{t}_{\mathrm{leg,begin}} \le \hat{t} \le \hat{t}_{\mathrm{leg,end}} \quad \text{otherwise} \quad \theta_{\mathrm{leg}} = 0. \tag{4.11}$$

where $\hat{t}$ is normalized time, defined as $\hat{t} := t/T$ where t is time and T is wingbeat period ($T := 1/f = 1/7.58 = 0.13$ s). The initiation and cease timings were manually determined from high-speed video recordings as $\hat{t}_{\mathrm{leg,begin}} = 0.2T$ and $\hat{t}_{\mathrm{leg,end}} = 0.42T$, respectively. The amplitudes were systematically varied to find the history of body angle and body trajectory closest to the measured data. The best set of launch angle, force amplitude and torque amplitude are $\theta_{\mathrm{thrust}} = 55$ (deg), $A_{F\mathrm{leg}} = 35$ (mN) $A_{N'\mathrm{leg}} = 20 \times 10^{-6}$ (N·m), respectively. The force and torque profiles are shown in Fig. 4.2 where green lines are the best curves and magenta dashed lines are the examples of the trials to later show the influence (sensitivity) of the amplitude on body angle and trajectory.

It should be noted that from the high-speed video recordings it is evident that the legs do not simultaneously leave ground, therefore the selected leg thrust profile surely includes some errors. Furthermore, in the present study the same θ_{leg} is used for both force and torque, although in reality there the timings. Very high response pressure sensitive paint (PSP) or a super accurate sensor for the insect-scale forces (Takahashi et al., 2013; Reinhardt and Blickhan, 2013) would be required but it is beyond the scope of the current study.

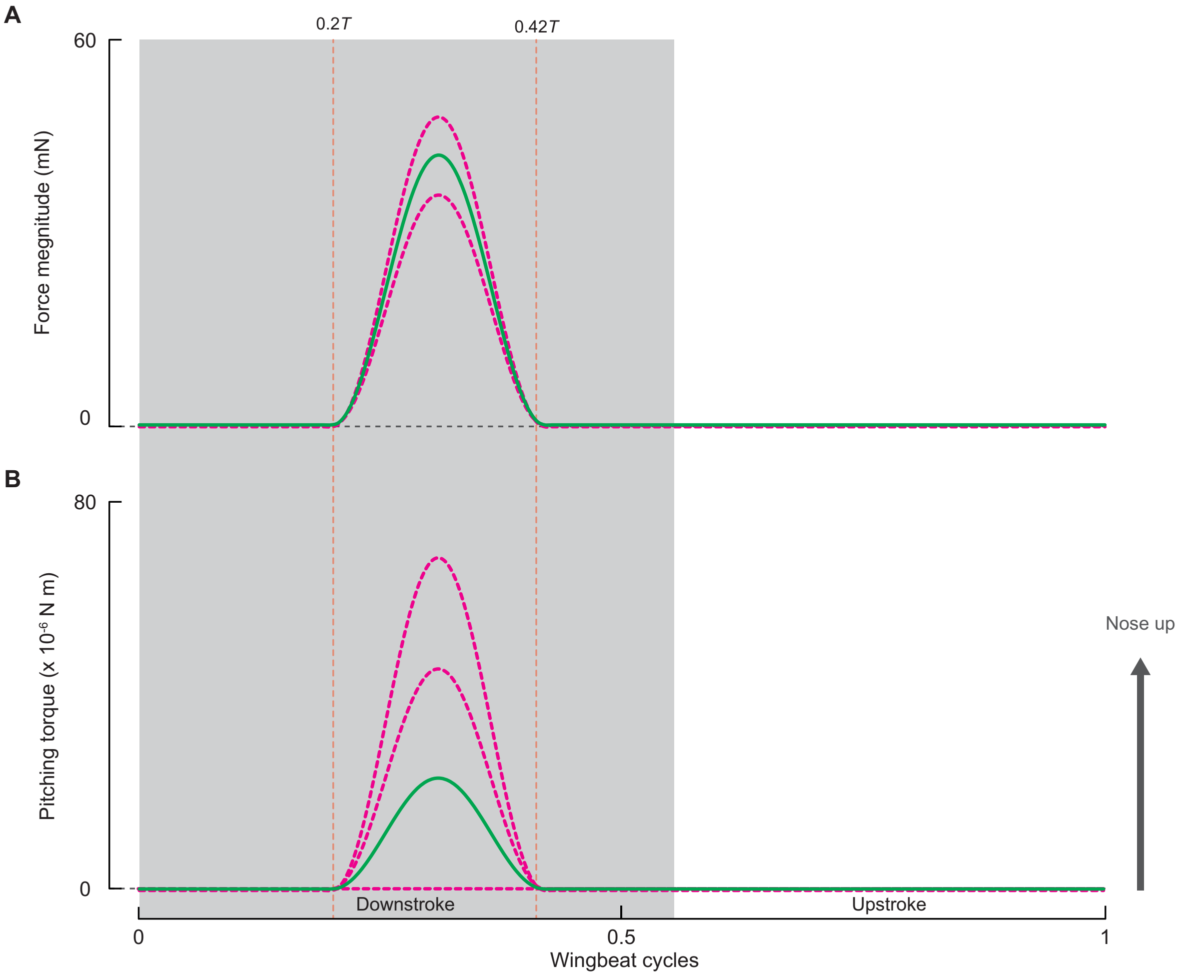

Figure 4.2. Profile of leg thrust force magnitude (A) and torque (B). Positive torque corresponds to the nose up moment. Several trials are represented by magenta dashed lines: for force magnitude, $A_{F\text{leg}}$ = 30 & 40 mN in A; and for torque, $A_{N'\text{leg}}$ = 0, 40, & 60 $\times 10^{-6}$ N m in B. Green solid lines ($A_{F\text{leg}}$ = 35 mN in A and $A_{N'\text{leg}}$ = 20 $\times 10^{-6}$ N m in B) represent the selected amplitudes whose resultant body angle and trajectory best fit with those from measurement (See Figs. 4.7 and 4.5).

Table 4.1. Three computation cases for comparison of ground effect and leg thrust. h_{ini} is height (distance) from ground, $A_{F\text{leg}}$ is leg thrust force amplitude, θ_{thrust} is thrust angle for leg thrust force, and $A_{N'\text{leg}}$ is leg thrust torque amplitude.

Model	Ground effect	Leg thrust		
	h_{ini} (mm)	$A_{F\text{leg}}$ (mN)	θ_{thrust} (deg)	$A_{N'\text{leg}} \times 10^{-6}$ (N·m)
OGE-LT	100	0	N/A	0
IGE-LT	20	0	N/A	0
IGE+LT	20	35	55	20

Ground effect

The ground effect is simulated by introducing a virtual ground in the computational domain, as exactly the same as in Chapter 3.

4.2.4 Computation cases

To test the hypothesis that both leg thrust and ground effect matter in the takeoff of butterfly, the following three computations are performed and compared to the measured results: out of ground effect and no leg thrust (OGE-LT); in ground effect but no leg thrust (IGE-LT); and in ground effect with leg thrust (IGE+LT), which is the most realistic 4.1.

4.3 Results and discussion

Although the rigid body dynamics was solved for 6 DOF, no side force or rotation around roll or yaw was observed because both the wing geometry and wing motion was assumed to be bilaterally symmetric in the current simulation and there was no asymmetric coupling observed. Therefore, only the x- (forward-backward) and the z- (vertical) components for forces or translational motion, and the y-component for torque or rotational motion, will be shown in the following sections.

4.3.1 Morphological and kinematic parameters

The morphological and kinematic parameters obtained in the measurement and used for the numerical simulation are summarized in Table 4.2. One notable parameter here is the large moment of inertia in x'-direction (i.e. around insect's roll axis), which is the result of large wing mass. The wing mass-to-body mass ratio calculates to 0.18. Wingbeat frequency is as low as less than ten thus reference wingtip velocity is just slightly over 2 m/s, which is comparable to the tiny fruit fly (See Chapter 2). However, due to the large mean chord length for the merged forewing and hindwing the Reyonlds number is over 4,000 (compared to fruit fly's 139).

Table 4.2. Parameters obtained in experiment and used for numerical simulation. Moment of inertia is in the body frame and averaged over one wingbeat cycle.

Wingbeat frequency, f (Hz)	7.58
Wingbeat amplitude, Φ (deg)	169
Density of air, ρ (kg/m^3)	1.225
Kinematic viscosity of air, ν (m^2/s)	1.5×10^{-5}
Wing length, R (mm)	53.5
Mean chord length (fore + hindwing), c_m (mm)	26.8
Aspect ratio, AR	2.0
Reference velocity, U_{ref} (m/s)	2.39
Reynolds number, Re	4280
Reduced frequency, k	0.267
Initial body angle, χ_ini (deg)	0
Total mass, M (mg)	393
Body mass, m_b (mg)	333
Wing mass (all the wings), m_w (mg)	60
Moment of inertia (x'-component), $J'_{\mathrm{x}'}$ (N·m)	4.53×10^{-8}
Moment of inertia (y'-component), $J'_{\mathrm{y}'}$ (N·m)	6.43×10^{-8}
Moment of inertia (z'-component), $J'_{\mathrm{z}'}$ (N·m)	6.65×10^{-8}

4.3.2 History of body motion

Time course of body motion as well as instantaneous wing shapes from the numerical simulation are illustrated as snapshots in Fig. 4.3.

The IGE-LT model (red) vanishes at around half the wingbeats, because the wingtips of the model touched the ground at $t/T \simeq 0.47$ (and was to protruding from the ground later). The real butterflies not infrequently touches the wingtips or even large portion of leading edges to the ground but then there will be a ground reaction force. Implementation of such contacting treatment requires additional effort and is beyond the scope of current study, therefore the computation was halted whenever wing or body touches the ground.

Nevertheless, it has been revealed from the difference between IGE-LT and IGE+LT models, the ground effect alone cannot lift the butterfly up at least in this particular takeoff sequence. In fact, it is later clarified the ground effect is negligible in this takeoff. This can be assumed from the images that the horizontal location of the OGE-LT model and IGE-LT model are essentially the same (Fig. 4.3, right images).

Also, the deviation from the original locations (crosshair marks) indicates IGE+LT model (green, which was adjusted to be similar to the measurement) moves longer distance in both horizontal and vertical compared to OGE-LT model (blue), indicating the force augmentation benefit from the leg thrust.

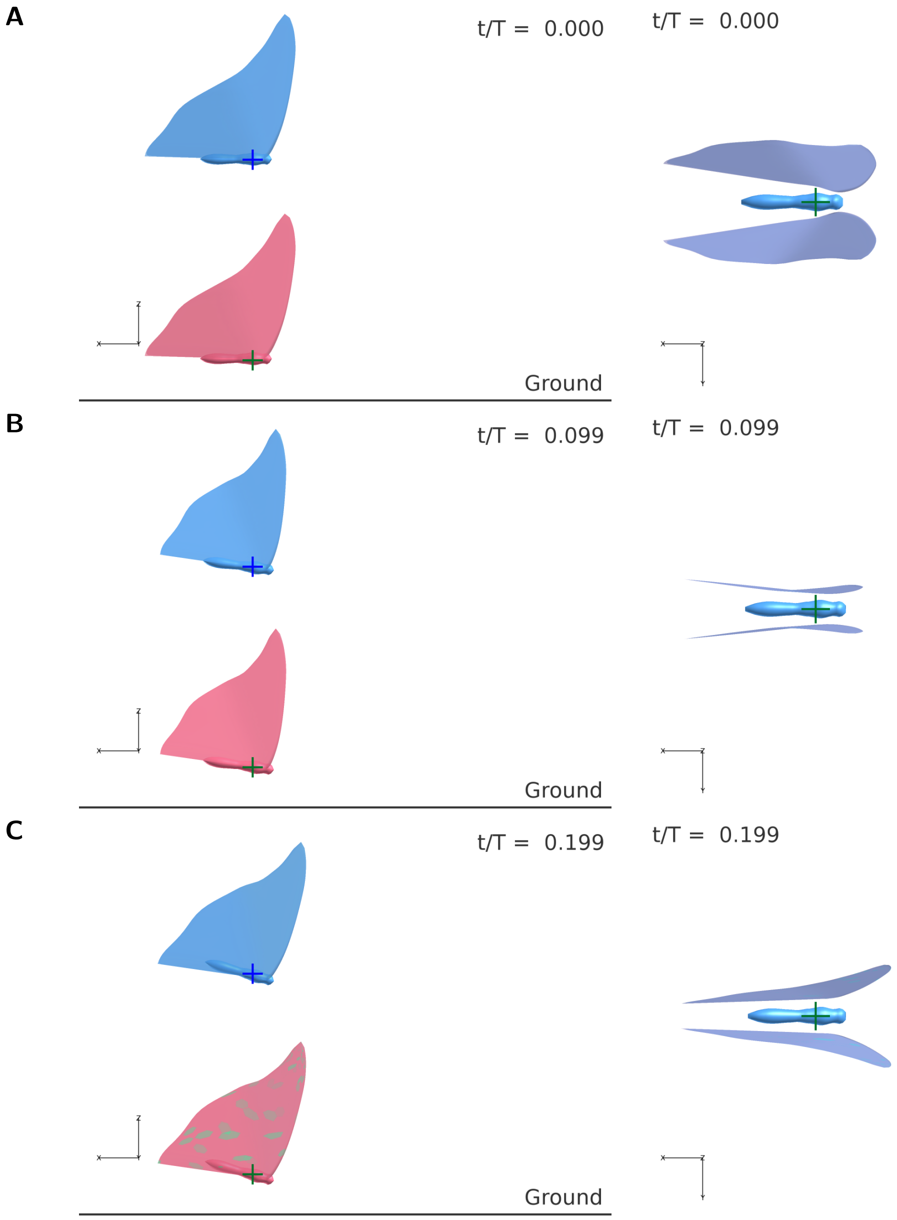

Figure 4.3. Snapshots of the butterfly takeoff simulation for approximately each 0.1 wingbeat cycles. Left, lateral view from right; right, dorsal view from above. Key to colors: blue, OGE-LT; red, IGE-LT; and green, IGE+LT. Cross hairs indicate the initial positions of the wingbase. IGE-LT model is not drawn after $t/T > 0.48$ because the wingtips of which touched the ground.

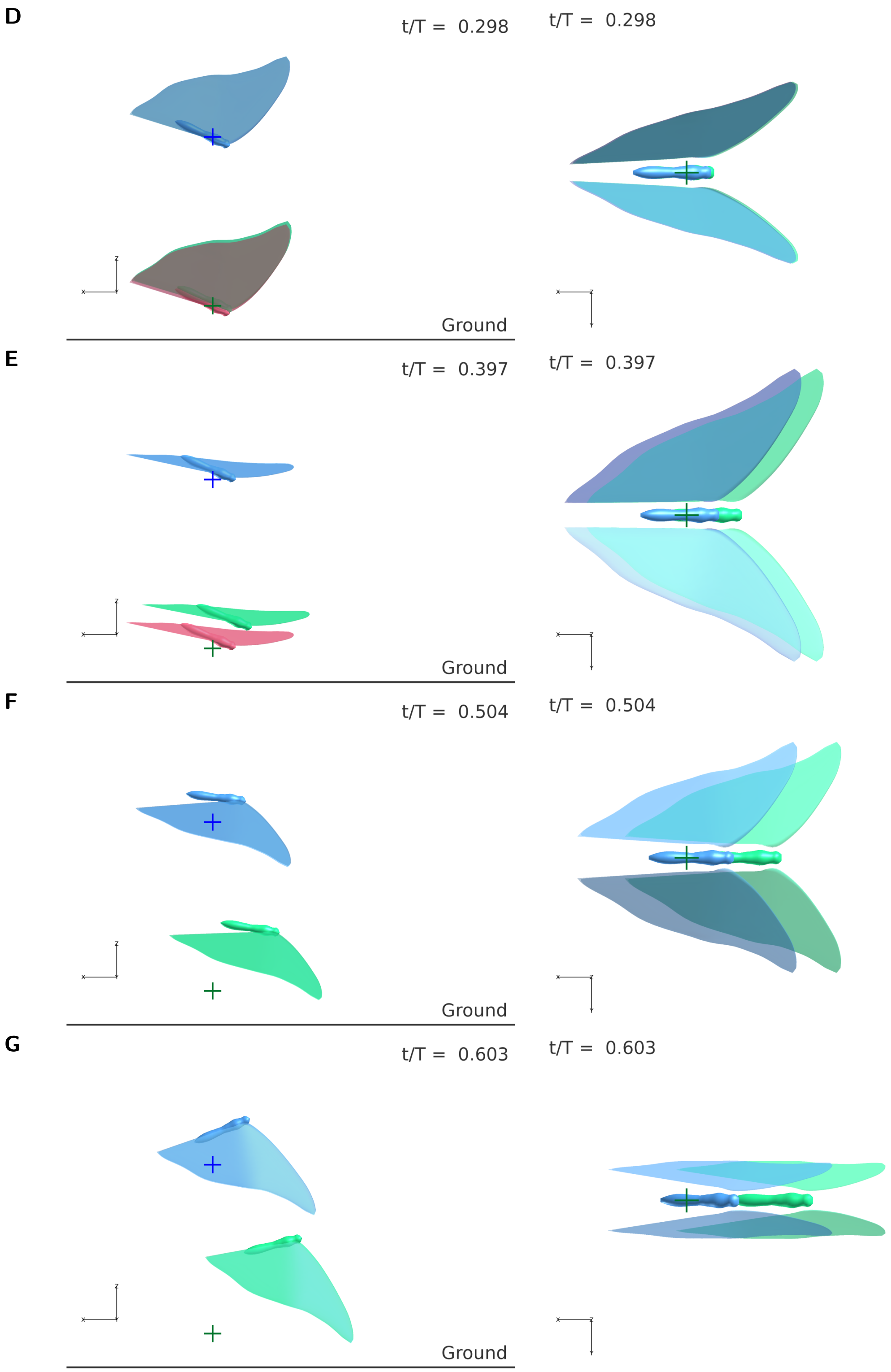

Figure 4.3. Snapshots of the butterfly takeoff simulation. (*cont.*)

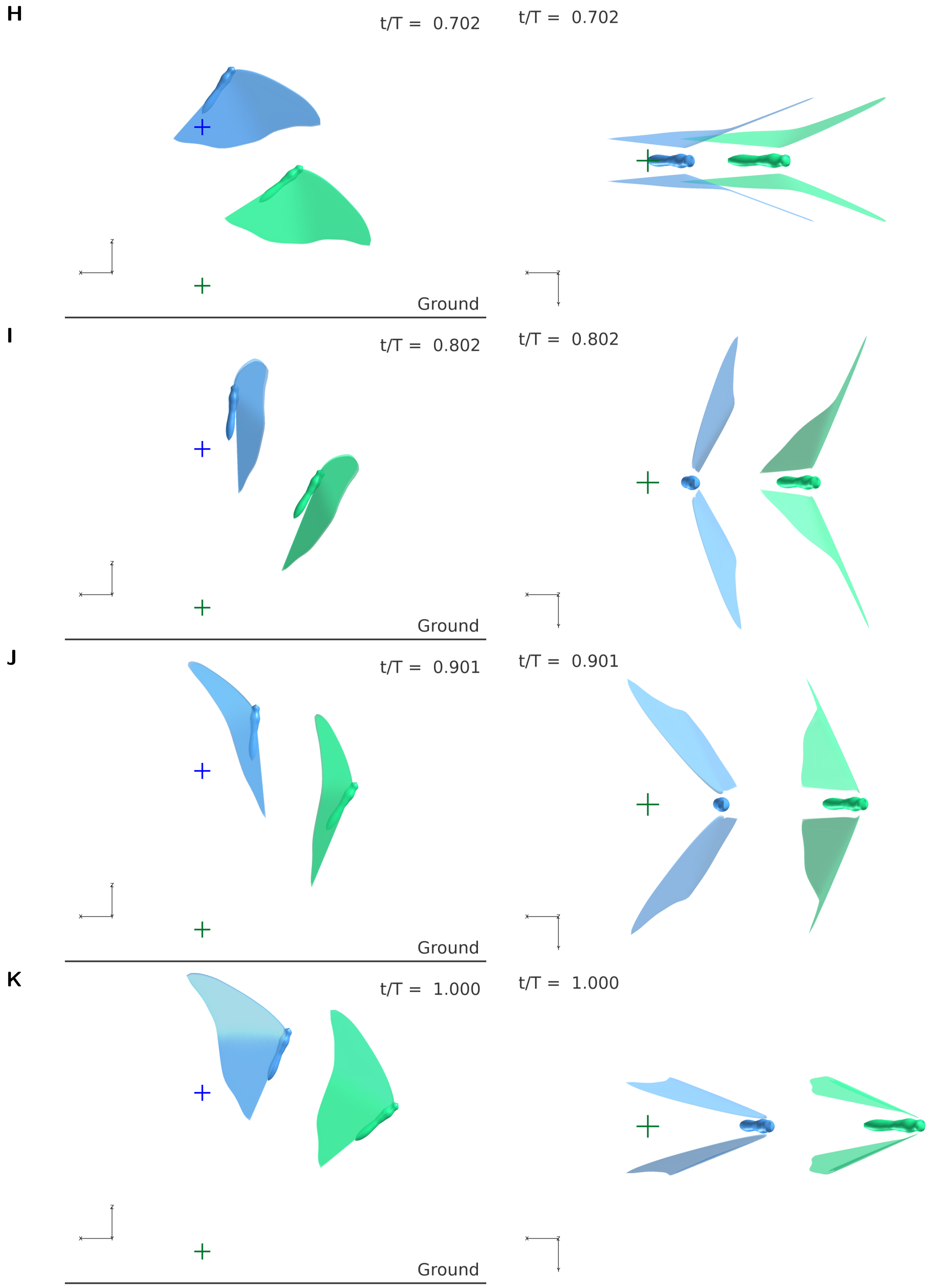

Figure 4.3. Snapshots of the butterfly takeoff simulation. (*cont.*)

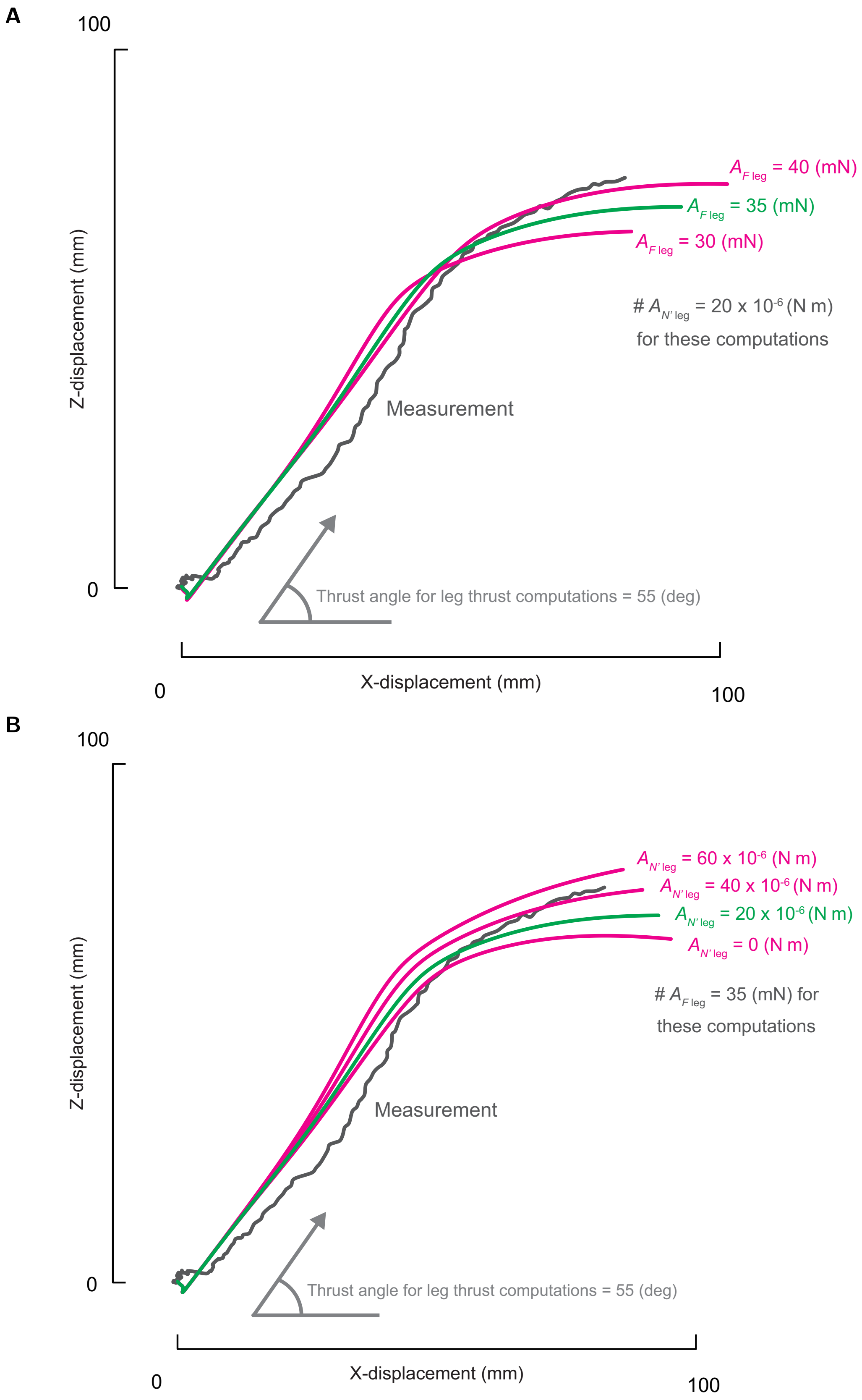

Figure 4.4. Effect of leg thrust force amplitude $A_{F\mathrm{leg}}$ (A) and leg thrust pitching torque amplitude $A_{N'\mathrm{leg}}$ (B) on body trajectory. Green line is the same IGE+LT model as in Fig. 4.5; magenta lines are the trials before arriving at the best result.

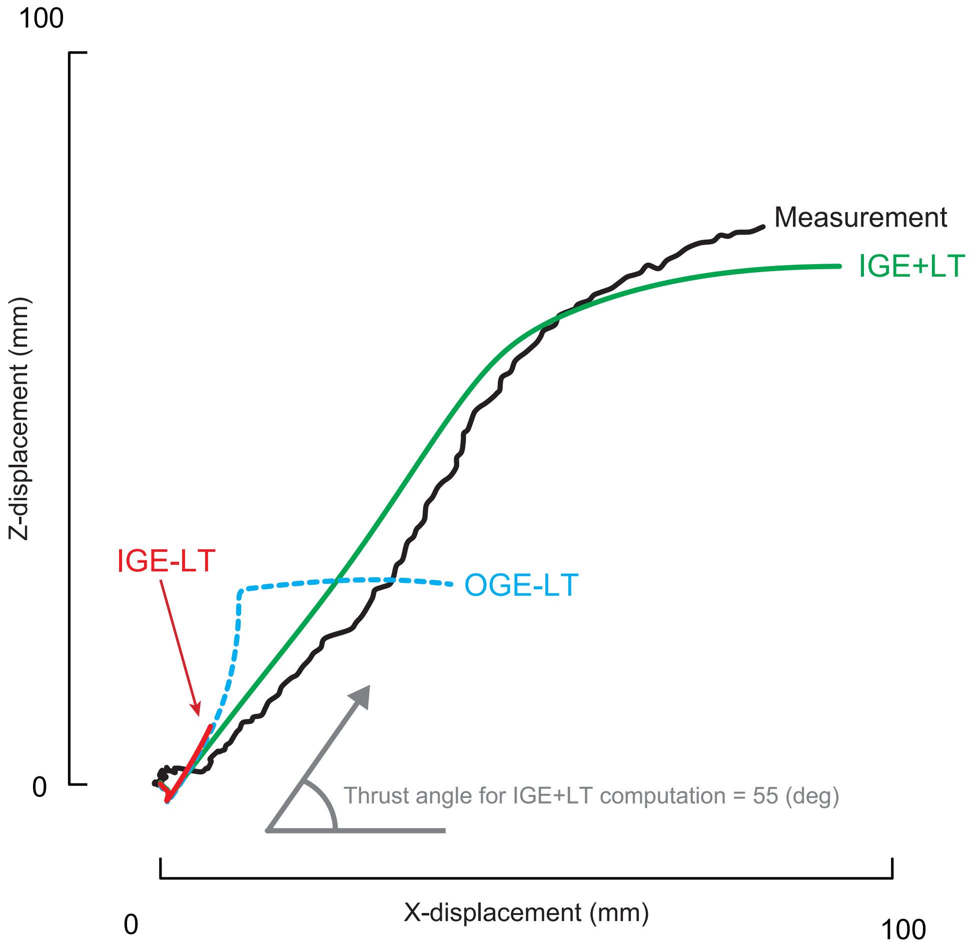

Figure 4.5. Body trajectory in butterfly takeoff as the displacement from the original position in the xz-plane in inertial frame. Black, from measurement; colored, relative motion of wingbase computed from numerical simulations. Key to colors: blue dashed line, OGE-LT; red solid line, IGE-LT; and green solid line, IGE+LT.

Body trajectory

The trajectories of body points in the vertical (xz-) plane as the deviation from the original locations are shown in Figs. 4.4 and 4.5. The movement in the y-direction is not shown because it is very small compared to the x- or z- movement (less than 8 mm in measurement and less than 1 mm in simulation). The measurement point is the intersection of body and wing estimated from head and tail points. The simulation results are the corresponding points. The deviation is selected to ignore the difference in the original height (h_{ini}) between the models.

In Fig. 4.4, the effect of leg thrust force amplitude (A) and torque amplitude (B) are illustrated where the green lines correspond to the best fitted, IGE+LT model. It can be seen the result of the force amplitude is rather unpredictable, because by lowering the force amplitude, at first the vertical displacement increased but the final altitude is lower; on the contrary increasing the force amplitude resulted in the reversed. Thus, there could be some non-linear coupling between leg thrust and aerodynamic forces. On the other hand, the effect of leg thrust torque amplitude seems to be more linear. However, it is later shown the relative impact of the torque is larger because the leg thrust torque amplitude is less than or of equal to the magnitude of aerodynamic torque, whereas the leg thrust force amplitude is more than 9 times the body weight and more than twice the peak aerodynamic forces. Therefore it can be concluded the trajectory is sensitive to both leg thrust force and torque.

It should be noted the torque amplitude does not have a good ability to change the distance traveled but rather the angle between the final destination and the initial location. Therefore, in order to go further, butterfly must kick stronger. Alternatively, butterfly might choose the lower thrust angle for going further horizontally (results not shown). Thus there would be some freedom for the butterfly.

In the comparison between three models (Fig. 4.5), it is quite clear the no-leg thrust models (OGE-LT, blue and IGE-LT, red) fails to reproduced the measured body trajectory (green) while the selected combination of leg thrust force and torque as well as thrust angle resulted in a good agreement with measurement (IGE+LT, green line). Also there is no noticeable difference between OGE-LT (blue) and IGE-LT (red), indicating very small ground effect.

Body angle

The instantaneous body angles are shown in Figs. 4.6 and 4.7. In contrast to the body trajectory, the effect of both leg thrust force amplitude (Fig. 4.6A) and torque (Fig. 4.6B) are both effective in changing the body angle and it seems that both have linear effects. As mentioned above, torque amplitude cannot contribute to the distance that much, therefore it may be reasonable to consider the force amplitude mainly determines how far it travels and thrust angle is to the initial direction, whereas the torque

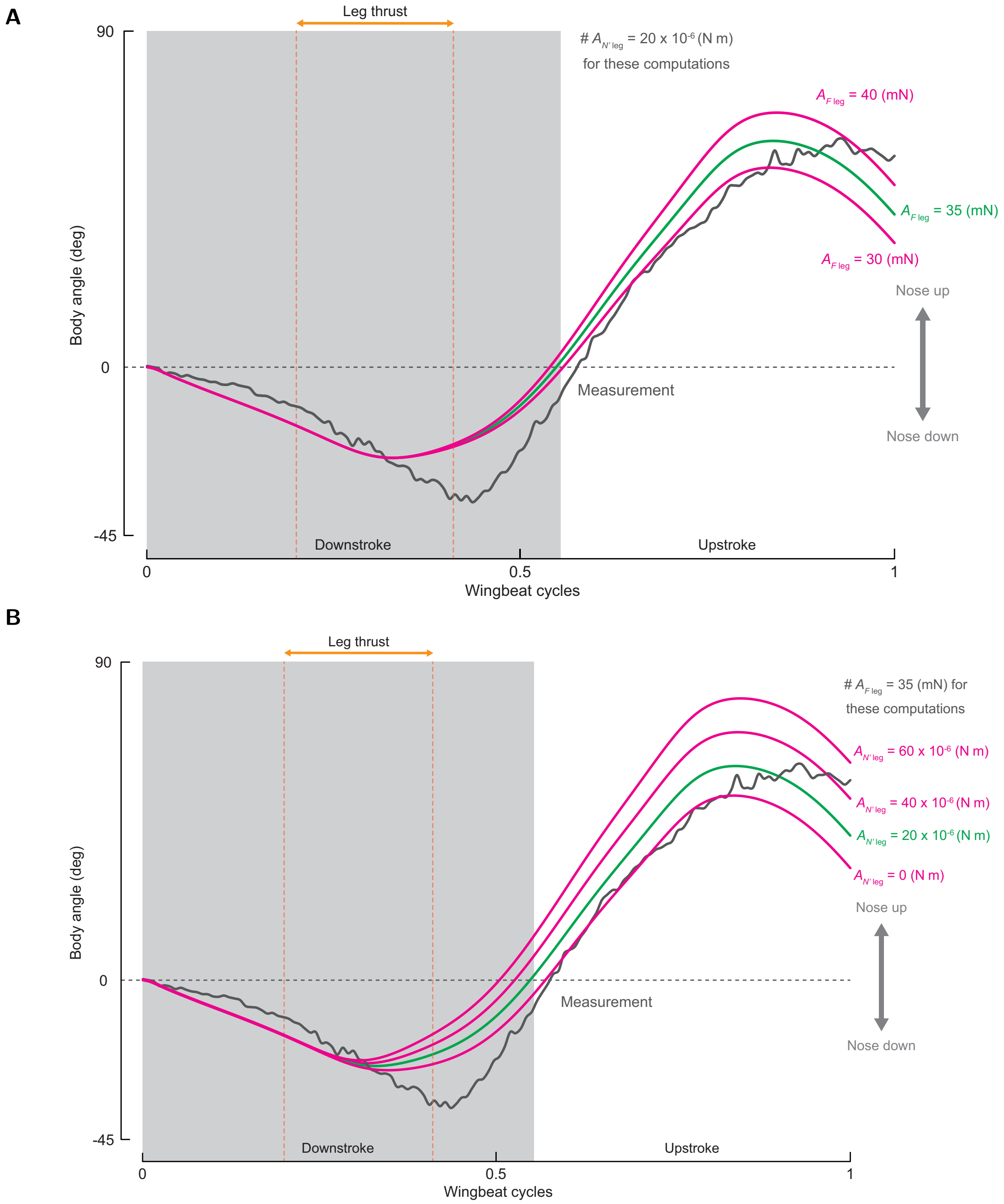

Figure 4.6. Effect of leg thrust force amplitude $A_{F\text{leg}}$ (A) and leg thrust pitching torque amplitude $A_{N'\text{leg}}$ (B) on history of body angle. Green line is the same IGE+LT model as in Fig. 4.7; magenta lines are the trials before arriving at the best result.

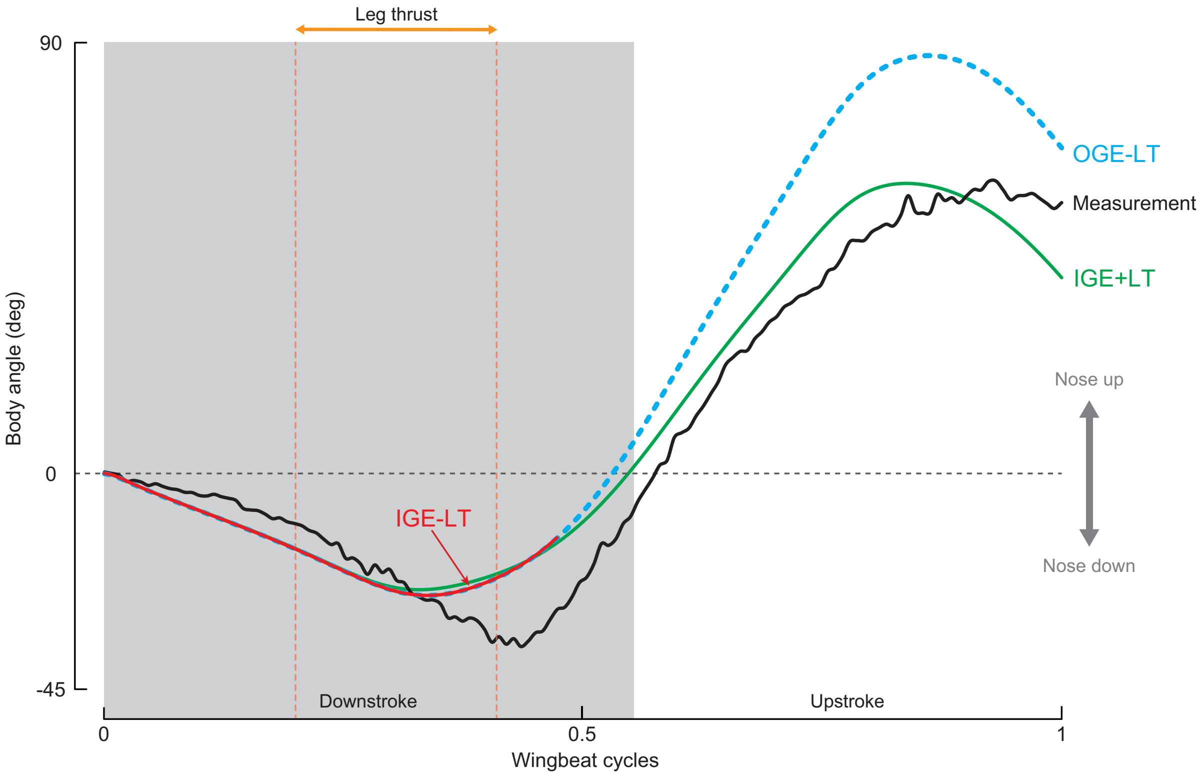

Figure 4.7. Body angle in butterfly takeoff. Black, from measurement; colored, relative motion of wingbase computed from numerical simulations. Key to colors: blue dashed line, OGE-LT; red solid line, IGE-LT; and green solid line, IGE+LT.

amplitude is a rather dependent variable to adjust the body angle.

The comparison between three model computations (Fig. 4.7) support this hypothesis. In contrast to the body trajectory, where lack of leg thrust resulted in a total failure of takeoff (Fig. 4.5), lacking the leg thrust resulted in what seems to be a non-fatal error (OGE-LT, blue dashed line). However, considering the aerodynamic forces the 30 degrees difference in body angle would not be regarded as small discrepancy and the adjustment of body angle is still important. Note the difference between OGE-LT (blue) and IGE-LT (red) are again negligible.

Velocity and angular velocity

Velocity and angular velocity histories are shown in Fig. 4.8. From these figures it is clear that the leg thrust forces significantly boost both forward and upward velocities (Fig. 4.8A and B, notice orange dotted vertical lines indicating the period leg thrust is applied). Especially the vertical velocity in OGE-LT model arrives at almost zero at the end of stroke, literally indicating failure of taking off. The pitching angular velocity (Fig. 4.8C) illustrates the oscillatory nature in the butterfly's flight. Noting the present computation does consider either inertial torque due to flapping or body deformation (articulation), it

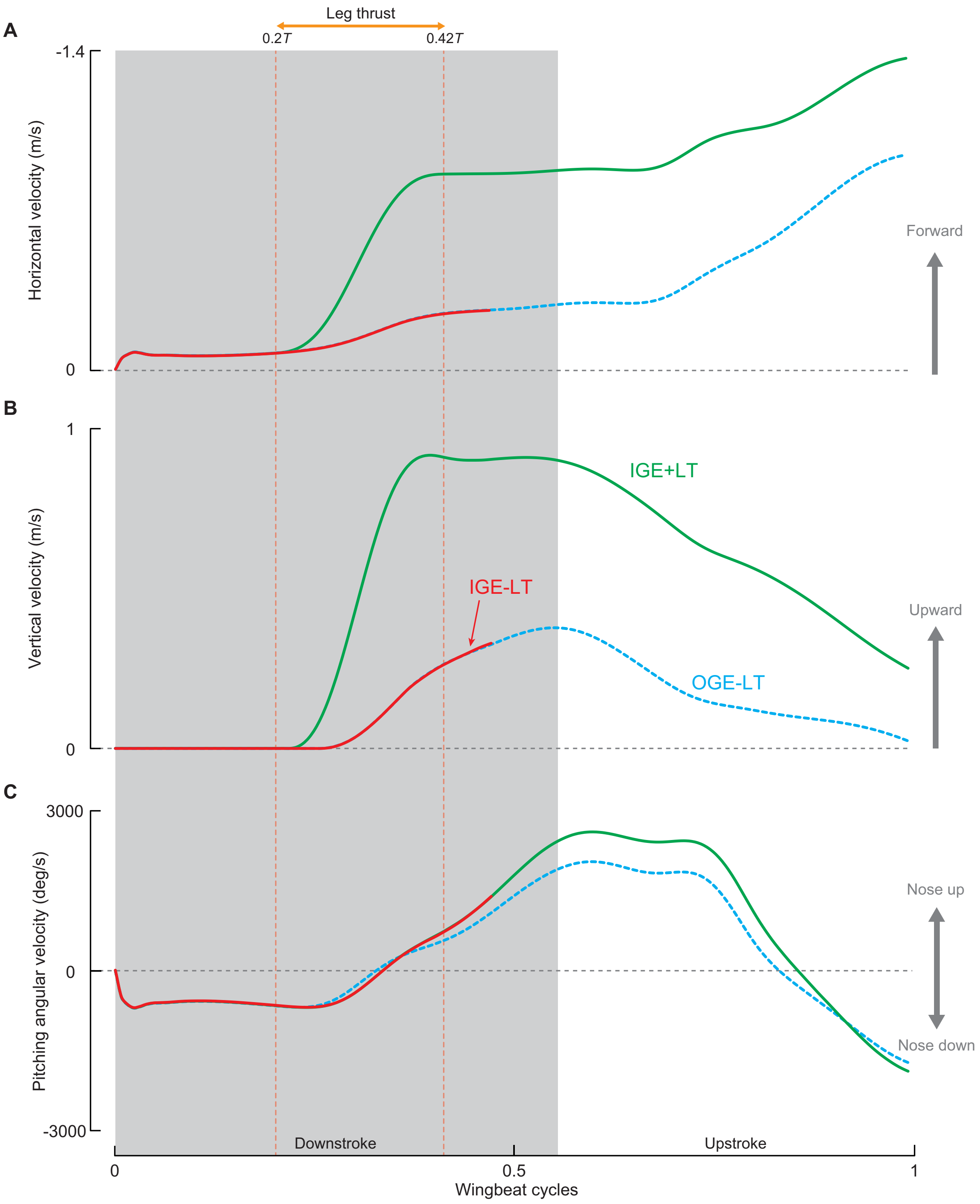

Figure 4.8. Histories of horizontal velocity (A), vertical velocity (B) and pitching angular velocity (C) computed in numerical simulation. Key to colors: blue dashed line, OGE-LT; red solid line, IGE-LT; and green solid line, IGE+LT. Note in horizontal velocity (A) the y-axis is inverted for convenience.

may be understood that the oscillation of the body angle characteristics in butterflies is at least partly due to aerodynamic torque.

4.3.3 Forces, torques and implications in the takeoff strategy

Force and torque components are summarized in 4.9. As it has been evident so far, there is only negligible difference between OGE-LT and IGE-LT computations, indicating there is almost no ground effect in this particular takeoff sequence.

A quite interesting event in these plots are found during the late period of leg thrust (around $0.3 < t/T < 0.5$) where the intensity of aerodynamic forces and torque are substantially reduced (green solid lines in Fig. 4.9). Horizontal force becomes almost zero and the vertical force becomes slight negative, while nose-up torque is relaxed. Pressure contours in this period (Fig. 4.10) illustrate striking contrast. The low-pressure regions on the leading edges of dorsal side of the wings (corresponding to the leading-edge vortices) in IGE+LT model (Fig. 4.10A) are greatly reduced compared to OGE-LT model (Fig. 4.10B). This is presumably caused by the rapid increase in the vertical (Fig. 4.8B) and perhaps partly by the increase in horizontal velocity, too (Fig. 4.8A).

Fig. 4.11 shows the far-field vortex structures of the butterfly models near the end of the stroke period ($t/T = 0.802$) where there is again a reduction in aerodynamics forces (Fig. 4.9). The vortex rings and the surrounding air velocity as footprints of the forces agree with this reduction, namely, weaker jet flow can be found in the IGE+LT model (Fig. 4.11B) compared to OGE-LT model (Fig. 4.11A).

In terms of energy economy, these reduction in useful (forward- and upward-) aerodynamic forces accompanied with the strong leg thrust forces (more than 9 times the body weight) would surely result in the higher metabolic cost. Nevertheless, this might have been a reasonable choice for this butterfly because the current takeoff seems to be an escape response to the external stimuli, not a voluntary one. Thus, there might be a trade-off between energy consumption and escape time.

Also notice that the duration of takeoff is very short compared to the remainders of the flight sequences. Therefore, bursting energy expenditure during short period of takeoff might not affect the fuel economy in total. Further studies on the comparison between with or without leg thrust takeoffs by recording real insects or birds Tobalske, 2004 would be required, which would promote better understanding in the relationship between animal behavior and takeoff biomechanics.

4.4 Conclusion

Butterfly takeoff was recorded with high-speed video cameras and its body motion as well as wing deformation was tracked and digitized. Using a simplified leg thrust model and virtual ground, the

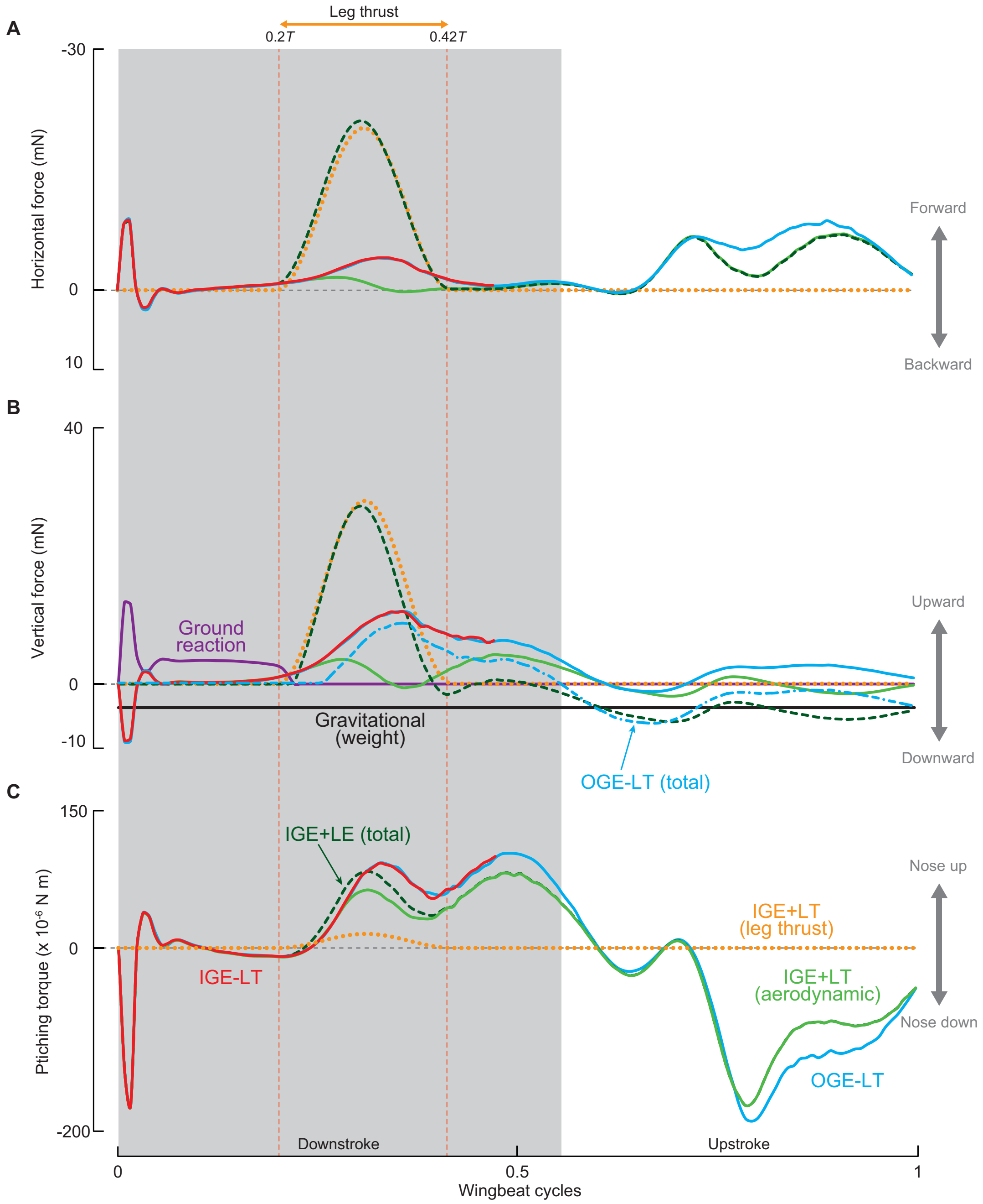

Figure 4.9. Histories of forces and torques. (A) Horizontal (x-component) forces. The axis is inversed for convenience of examination (positive is backward and negative is forward). Solid lines are aerodynamic forces: blue, OGE-LT model; red, IGE-LT model; and green, IGE+LT model. Orange dotted line is leg thrust force. Dark-green dashed line is the sum of aerodynamic force and leg thrust force in IGE+LT model. (B) Vertical (z-component) forces. The same legends in (A) applies for the blue, green, red, and orange lines. In addition, gravitational force (black) and ground reaction force (purple) are shown. The gravitational force is exactly the same for the all the cases. The ground reaction force drawn here is for the IGE+LT model, but almost the same for all three cases except for the very small (< 0.2 mN) difference at the beginning of the leg thrust, thus the ground reaction forces for the other two cases are not shown. Blue dot-dashed line and dark-green dashed line are the sum of all the vertical forces in OGE-LT model and IGE+LT model, respectively. The counterpart for IGE-LT model is not drawn because it is essentially the same as that of OGE-LT model. (C) Pitching (y-component) torques around the insects total center of mass. The same legend as of (A) applies.

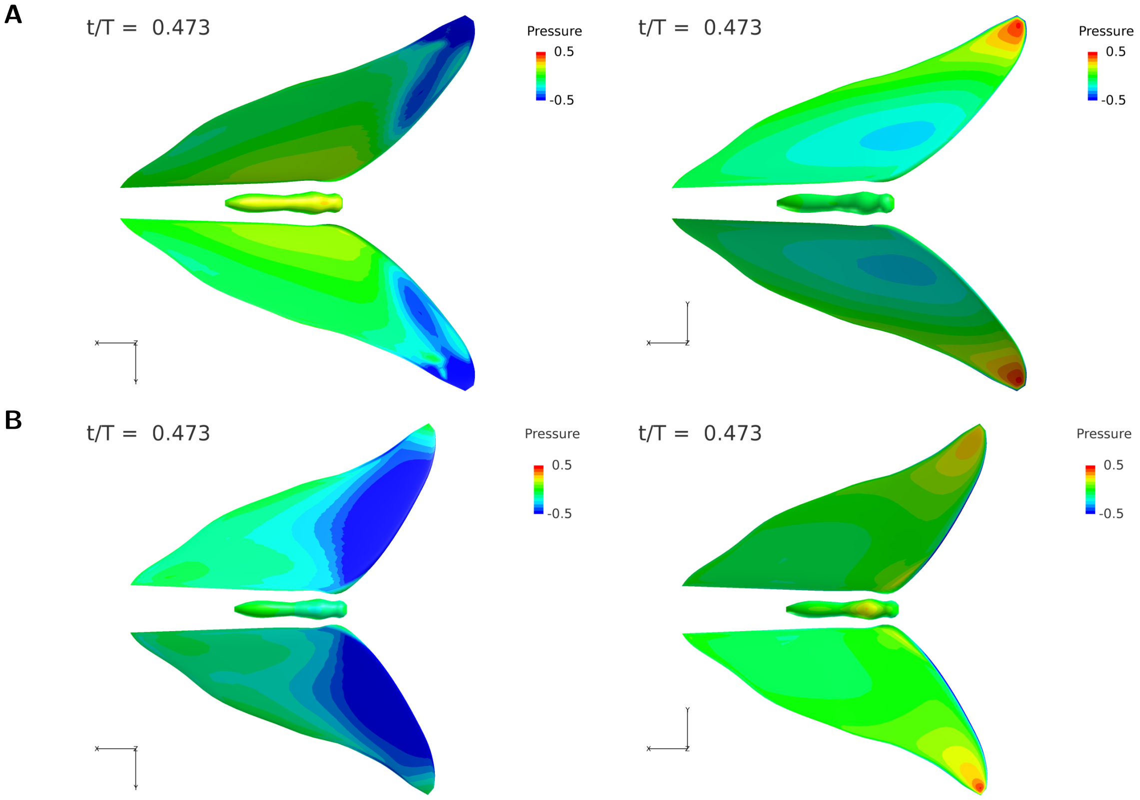

Figure 4.10. Pressure contours on the butterfly's wings and body for OGE-LT model (A) and IGE+LT model (B), both at $t/T = 0.473$ (mid to late downstroke). Pressure is the normalized gauge pressure. Left, dorsal views; right, ventral views.

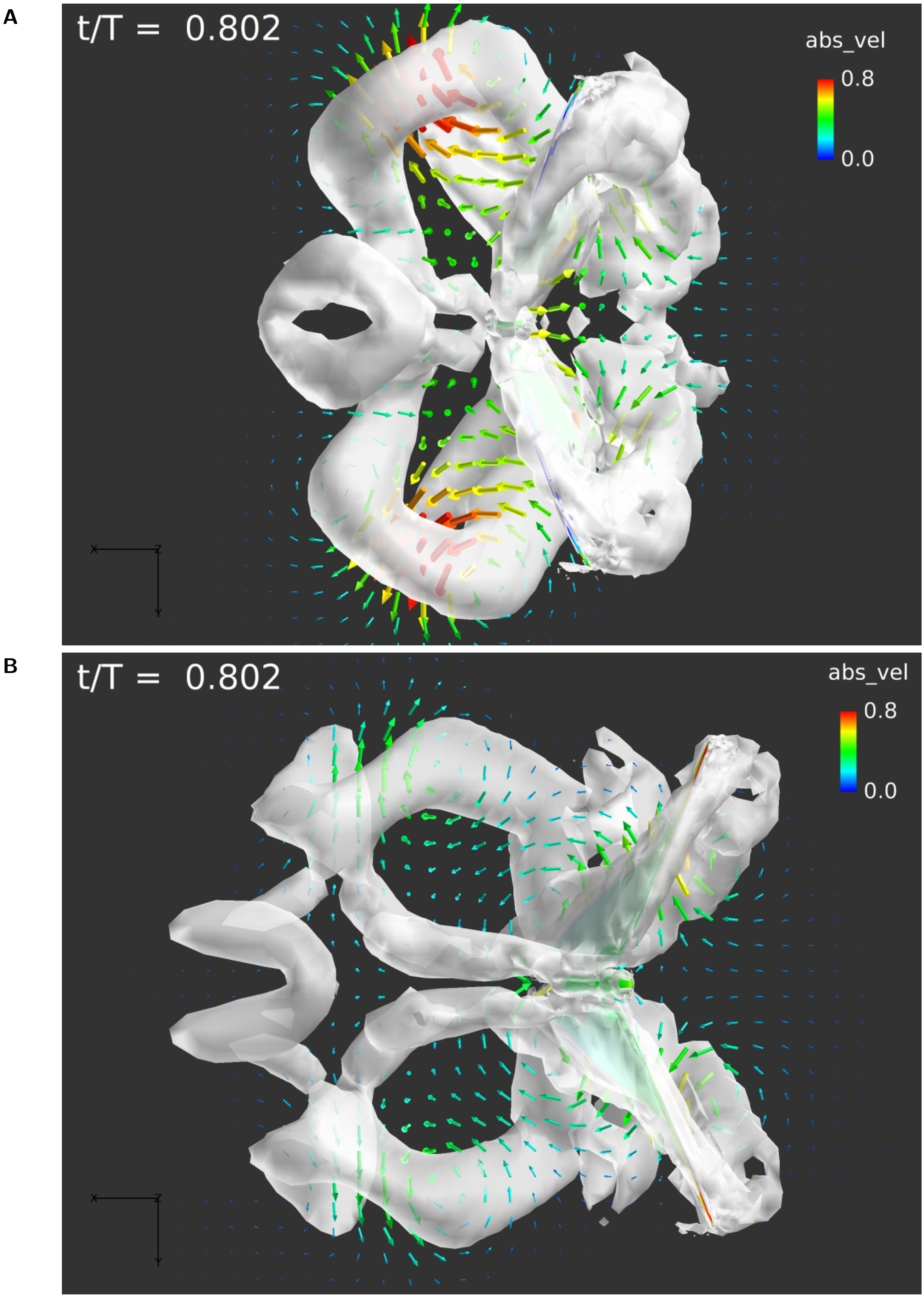

Figure 4.11. Top view of flow visualizations of OGE-LT model (A) and IGE+LT model (B), both at $t/T = 0.802$ (late upstroke). White, smoke-like object is the iso-surfaces of Q-criterion at 0.05. Vectors are the velocity field in a horizontal plane at the height of 3.6 (A) and 1.5 (B) mean chord length above the ground, colored by absolute velocity.

relative importance of leg thrust and ground effect in butterfly takeoff was explored with a realistic dynamically deforming wing model based on the measurement. The results shows there is no influence from ground but a significantly large contribution from leg thrust. The rapid increase in the flight velocity diminish the aerodynamic forces during and just after the leg thrust period but this might be the adaptation strategy of the butterfly to the quick escape response.

In the current study the ipsilateral (i.e. being the same side of the body) forewing and the hindwing are modeled as a merged, single wing grid. One possible future approach is to model each fore- and hindwing separately and see if there is an influence. It was reported the hindwing is unnecessary in the acquisition of the aerodynamic forces but improves maneuverability, by removing the hindwings of butterflies (Jantzen and Eisner, 2008). The separate wing model may be suitable for such a forewing-only situations. However, it must be very careful because the wing kinematics is very likely different from the intact insect. Therefore, the framework combining the experimental and numerical methods, which has been developed in the current study, would be mandatory in the such an investigation, and probably flapping flight in general.

References

Bimbard, G., Kolomenskiy, D., Bouteleux, O., Casas, J. and Godoy-Diana, R. (2013), ‘Force balance in the take-off of a pierid butterfly: relative importance and timing of leg impulsion and aerodynamic forces.’, *J. Exp. Biol.* **216**(Pt 18), 3551–3563.

Bonser, Richard, H. C. and Rayner, J. M. V. (1996), ‘Measuring leg thrust forces in the common starling’, *J. Exp. Biol.* **199**, 435–439.

Brodsky, A. K. (1991), ‘Vortex Formation in the Tethered Flight of the Peacock Butterfly Inachis io L. (Lepidoptera, Nymphalidae) and some Aspects of Insect Flight Evolution’, *J. Exp. Biol.* **161**, 77–95.

Card, G. and Dickinson, M. H. (2008), ‘Performance trade-offs in the flight initiation of Drosophila.’, *J. Exp. Biol.* **211**, 341–353.

Dudley, R. (1991), ‘Biomechanics of flight in neotropical butterflies: aerodynamics and mechanical power requirements’, *J. Exp. Biol.* **159**, 335–357.

Earls, K. D. (2000), ‘Kinematics and mechanics of ground take-off in the starling Sturnis vulgaris and the quail Coturnix coturnix.’, *J. Exp. Biol.* **203**(Pt 4), 725–39.

Heppner, F. H. and Anderson, J. G. T. (1985), ‘Leg thrust important in flight take-off in the pigeon’, *J. Exp. Biol.* **114**, 285–288.

Jantzen, B. and Eisner, T. (2008), 'Hindwings are unnecessary for flight but essential for execution of normal evasive flight in Lepidoptera.', *Proc. Natl. Acad. Sci. U. S. A.* **105**(43), 16636–16640.

Nakata, T., Liu, H., Tanaka, Y., Nishihashi, N., Wang, X. and Sato, A. (2011), 'Aerodynamics of a bio-inspired flexible flapping-wing micro air vehicle.', *Bioinspir. Biomim.* **6**(4), 045002.

Reinhardt, L. and Blickhan, R. (2013), 'Ultra miniature force plate for measuring triaxial forces in the micro newton range', *J. Exp. Biol.* .

Srygley, R. B. and Thomas, A. L. R. (2002), 'Unconventional lift-generating mechanisms in free-flying butterflies.', *Nature* **420**(6916), 660–664.

Sunada, S., Kawachi, K., Watanabe, I. and Azuma, A. (1993), 'Performance of a butterfly in take-off flight', *J. Exp. Biol.* **183**, 249–277.

Takahashi, H., Matsumoto, K. and Shimoyama, I. (2013), Micro force plate array for measurement of ground reaction force of insect running, *in* '2013 IEEE 26th Int. Conf. Micro Electro Mech. Syst.', Vol. 2, Ieee, pp. 59–62.
URL: *http://ieeexplore.ieee.org/lpdocs/epic03/wrapper.htm?arnumber=6474176*

Tobalske, B. W. (2004), 'Take-off mechanics in hummingbirds (Trochilidae)', *J. Exp. Biol.* **207**(8), 1345–1352.

Zheng, L., Hedrick, T. L. and Mittal, R. (2013), 'Time-varying wing-twist improves aerodynamic efficiency of forward flight in butterflies', *PLoS One* **8**(1), e53060.

Chapter 5

Flapping flight with wing deformation: hummingbird hovering

5.1 Introduction

Wing deformation in flapping flight has been attracting attention from the biomechanics of animal flight community as well as flapping aerial vehicle researchers. This is because it has been shown the wing compliance and inherent deformation during flapping due to inertial and/or aerodynamic loads can be beneficial in generating aerodynamic forces1). One of the best ways to elucidate such complex phenomena is to obtain wing deformation of real animals flapping wings and construct the numerical model, thereby enabling the comparative study between the realistic model and an idealized flat-plate model or a reduced deformation model. There are a few such works available but to date forward flight of insect are the majority (Young et al., 2009; Zheng et al., 2013*b*; Le et al., 2013) and therefore still limited in number, species, or flight conditions. Note there are several other methods include fluid structure interaction (FSI) (Nakata and Liu, 2012) or utilization of optimization (Zheng et al., 2013*a*).

Hummingbirds are known to have significant wing deformation during hovering flight (Warrick et al., 2005; Wolf et al., 2013; Tobalske, 2010) but its impact on the generation of aerodynamic force is largely unknown. In this study we aim at clarifying the effect of wing deformation in a hummingbird wing by combination of experimental and numerical methods.

5.2 Methods

5.2.1 High speed video recordings and three-dimensional wing reconstruction

Hovering flight of a hummingbird (*Amazilia amazilia*) feeding nectar (NEKTAR-PLUS, Nekton GmbH, Germany) was recorded in the Tama Zoological Park (Tokyo, Japan) in November 2012. The hummingbird lived in a large greenhouse (1140 m^2 in area and 16 m in ceiling height) in the zoo. The air temperature was 22 C. Four high-speed digital video cameras, composed of three FASTCAM SA3 and a FASTCAM SA2 (Photron Ltd., Japan; courtesy Photron) were used, whose resolutions are $1024times1024$ and $2048times1080$ pixels, respectively. The cameras were synchronized at 2000 frames per second via Gigabit Ethernet and the shutter speed for all the cameras was set at 1/3000 s. To improve the contrast of the image, white background paperboards were placed. On the assumption that the wing shape and wing kinematics of a stationary hovering hummingbird is bilaterally symmetric about the sagittal plane, we focused on the right wing.

A custom-made calibration tool with eight metallic spheres is used for the later calibration (Fig. 5.1). The dimension of the calibration frame is 150 mm x 120 mm x 120 mm. The image of a metallic ruler hung from the metal wire, which usually carries the nectar feeder, was shot to provide vertical unit vector (thus horizontal plane).

The mass of the hummingbird was measured on two days later of the day of video recordings. A single-axis load cell, LTS-100GA, and a 12-bit AD interface, PCD-300A (Kyowa Electronic Instruments Co., Ltd, Japan) were used with sampling rate of 1000 Hz. A ring-shaped perch was attached to the top of the load cell and located under the nectar feeder. The averaged mass for the three events was approx. 5.4 g. Usually the bird start to drink when its body mass is approx. 5.1 g and leave the feeder at around 5.5 g.

Three-dimensional coordinates of the hummingbird right wing was reconstructed as follows. After preliminary sampling of wingbeat frequency, wingbeat amplitude, and body angle for the whole recording data, one wingbeat cycle from the first recording bout was selected for further study, because the cycle featured the most reciprocating wing kinematics.

The selected cycle is composed of 65 time frames. After unsharp masked to reduce blur, each image was imported as a background bitmap to a commercial CAD software Rhinoceros (Robert McNeel & Associates, USA). The wing outlines (edges) and feather shafts (rachises) were manually tracked and extracted as points for each image (Fig.5.2). The exported points were then processed with an in-house DLT program. Because of the identity of each point is unknown except for the start and end points, a simplex optimization was utilized to reduce error and obtain best fit curves. The reconstructed points were then fitted with triangle elements to calculate wing surface area (Fig. 5.3).

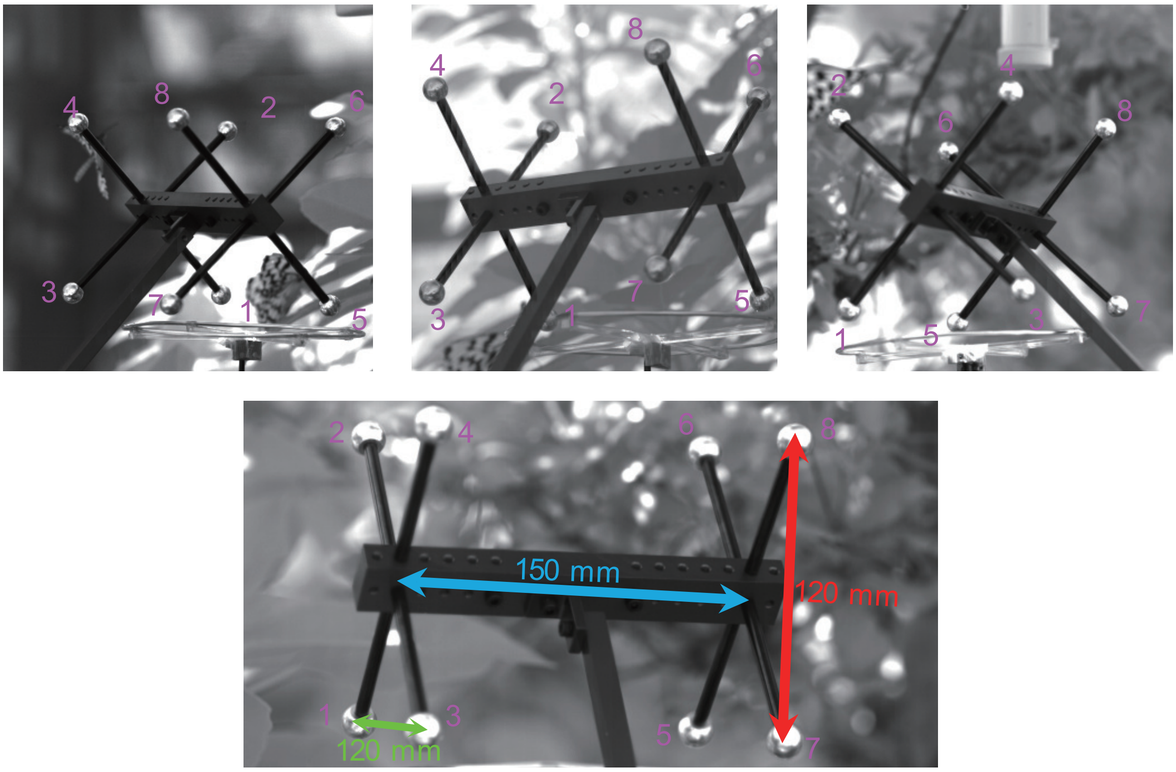

Figure 5.1. Calibration frame and its dimension. The numbers in purple color are the identity of the spheres. Note the fourth image is from SA2 whose resolution is $2048 times 1080$ pixels whereas the others are $1024 times 1024$ pixels.

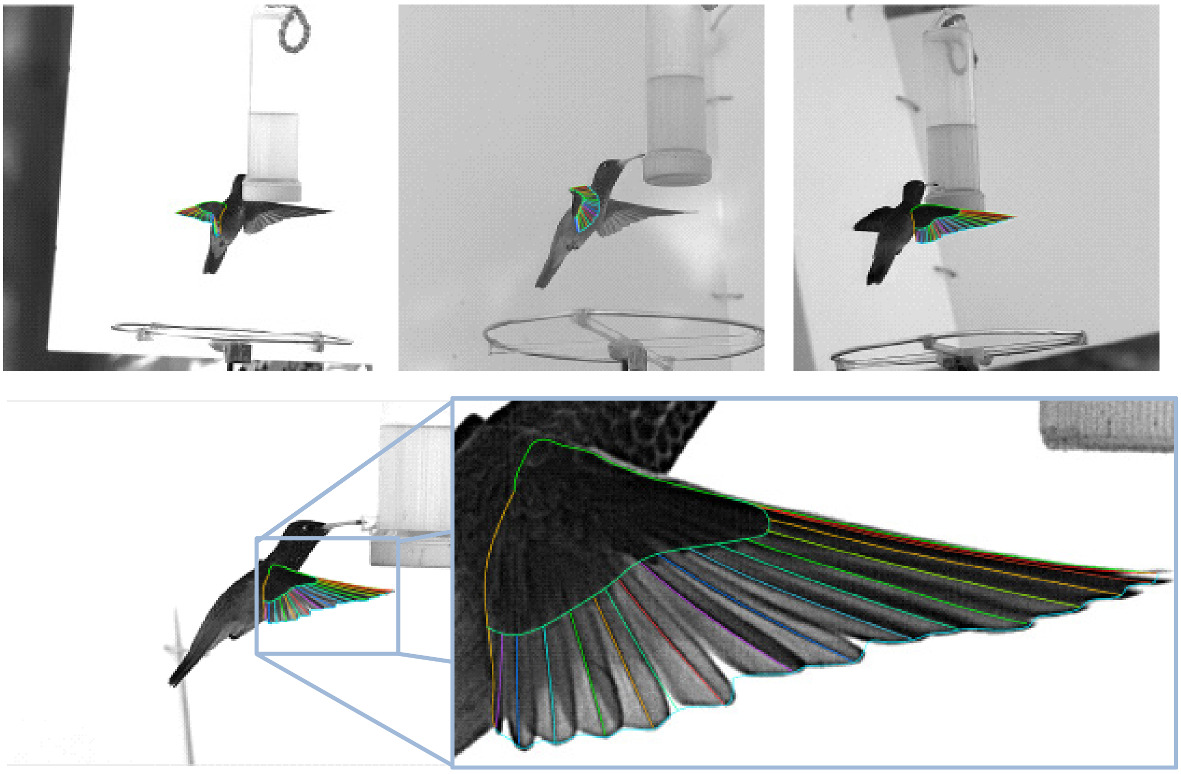

Figure 5.2. Sample images in the three-dimensional reconstruction process. The wings are in the early upstroke.

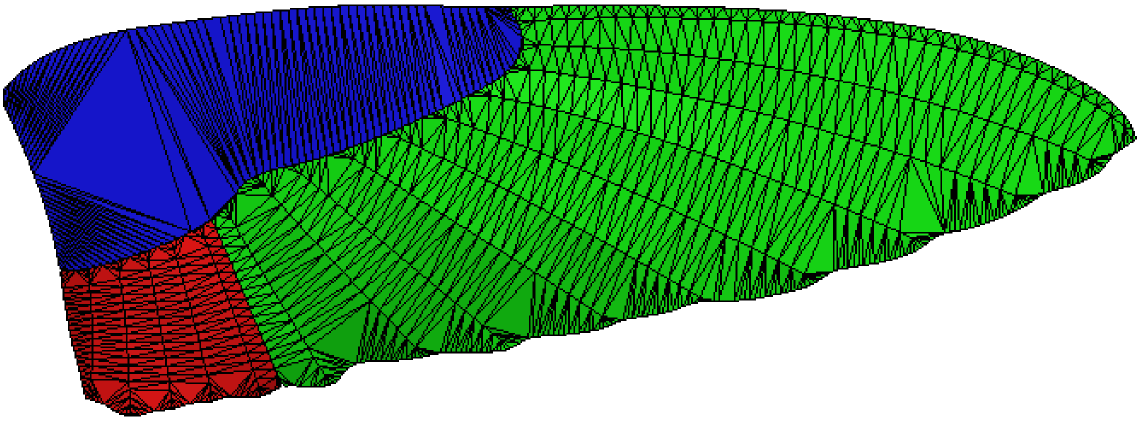

Figure 5.3. Triangle surface mesh of the reconstructed wing. The wing is partitioned into three regions: green, primary feathers; red, secondary feathers; and blue, covert feathers. Note the covert feathers are hiding some parts of the primary or secondary feathers.

5.2.2 Numerical simulation

Single-wing flapping computations were carried out with four types of numerical wing models: a full-fidelity, dynamically morphing wing model (hereafter termed original model) and three flat-plate wing models. The in-house flow solver proven in various applications of insect flapping flights (Liu and Aono, 2009; Nakata et al., 2011) is used with slight modifications: instead of having three grid blocks (body = global block plus two local wing blocks), in this study one Cartesian global grid is prepared in which one local wing grid block is immersed (Fig. 5.4). The aerodynamic force and power are calculated via integration over the cells on wing surface. The details of the numerical methods can be found elsewhere (Liu, 2009).

The original wing model was created based on the reconstructed wing surface where fifth order Fourier series was employed for temporal interpolation. The wing surface area, among other morphological parameters, of the original wing showed significant variation during the course of wing strokes. Therefore, for comparison, three flat models having different wing areas were prepared: flat-ave model has the wing area of the wingbeat-cycle averaged area of the original wing model; flat-max model has the largest wing area in the original model; flat-min model has the smallest wing area in the original model. The wing areas of the flat models are time-invariant. The planform shapes of the flat models are based on the original model at the pronation phase because at the moment the wing has almost no deformation. Because the change in wing length was less than 10%, this variation was neglected in the current study and all the flat models have the same wing lengths R derived from the time-average of the original model; instead, the mean chord lengths were manipulated to achieve the desired areas, as illustrated in Fig. 5.5. The variation in mean chord length leads to slight differences in the aspect ratio, Reynolds number and

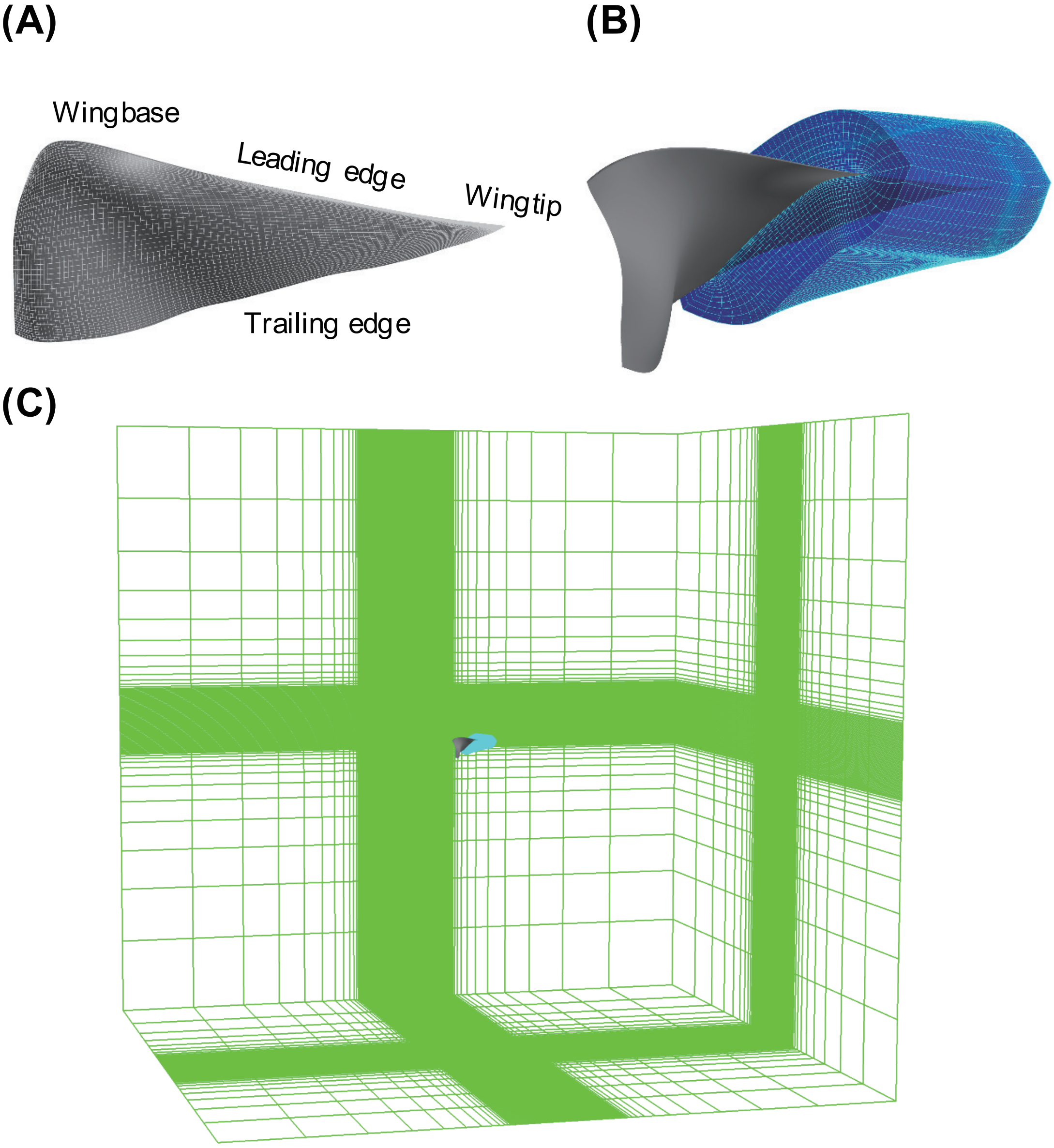

Figure 5.4. The numerical grid system, composed of a right wing model of the measured hummingbird (A, B) and a background Cartesian grid (D). (A) The original wing model surface viewed from approximately the same angle as Fig. 5.2(E). In (B), wingtip portion of outer boundary of wing gird and cross section are illustrated in blue. (C) Global grid block, the middle of which wing grid block is immersed in.

Table 5.1. Parameters obtained in experiment and used for numerical simulation.

Wingbeat frequency, f (Hz)	28.8
Wingbeat amplitude, Φ (rad)	1.80
Density of air, ρ (kg/m^3)	1.171
Kinematic viscosity of air, ν (m^2/s)	1.577×10^{-5}
Wing length, R (mm)	70.9
Reference velocity, U_{ref} (m/s)	7.34
Stroke plane angle, β (deg)	12.2

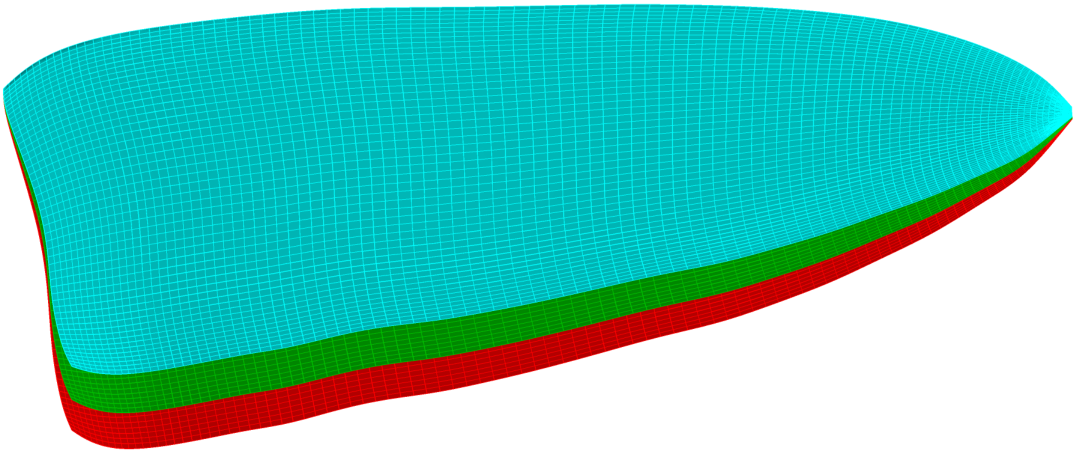

Figure 5.5. Comparison of planforms of flat wing models. Green, average area model (flat-ave); red, max area model (flat-max); blue, min area model (flat-min).

reduced frequency.

The wing angles necessary for actuating the flat wing models were extracted from the original model. Stroke plane angle, positional angle, and elevation angle were derived from wingtip path, whereas for feathering angle the wing chord at 75% wing length (i.e. 0.75R from wingbase) in the original model was used. The resultant wing kinematics is shown in Fig. 5.10(A). For definition of the wing angles refer to Liu & Aono (Liu and Aono, 2009).

The parameters common for all the models are summarized in Table 5.1 and the different parameters in the different wing models are summarized in Table 5.2. In the present study, wing thickness is set as 0.002 times the mean chord length, therefore the dimensional thicknesses subtly vary among the models. Each simulation trial was carried out from 0 to 8 wingbeat cycles (t/T).

Table 5.2. Comparison of the morphological parameters and the dimensionless numbers between the different models.

Model	c_m (mm)	S_surf (mm^2)	Re	k
Original	18.1	1198-1468	8420	0.223
Flat-max	20.7	1468	9640	0.255
Flat-ave	18.9	1338	8790	0.233
Flat-min	16.9	1198	7870	0.208

5.3 Results and Discussion

5.3.1 Wing morphology and kinematics

Fig. 5.6 illustrates the time course of external shapes and orientations of the wing models (gray, original model and green, flat-ave model) for a complete wingbeat cycle. Fig. 5.7 shows the time course of four spanwise sections (airfoils) of the original model in the wing frame. From these still images it is evident the wing (original model) has substantial wing deformation including both twist and camber.

To further assess the dynamic wing deformation, the temporal variation of the morphological and kinematic parameters extracted from the original wing model are presented in Fig. 5.8. Positional angle (Fig. 5.8A, open circles) shows a symmetry in downstroke and upstroke. The mean positional angle around which the wing oscillates is apparently around 0 deg, which shows contrast to the previous reports (Tobalske et al., 2007; Wolf et al., 2013). Elevation angle is not particularly large or small (Fig. 5.8A, filled triangles). The ratio of downstroke and upstroke duration was approximately 1:1, which is consistent with a report for the hovering observations on a different hummingbird species (Tobalske et al., 2007). Wing surface area (Fig. 5.8B) shows significant variation during the strokes. The area rapidly increases from pronation to early downstroke and continues gradual increase throughout the downstroke. It rapidly decreases in supination, followed by a gradual decrease and eventual increase in the upstroke. The peak-to-peak variation of wing surface area reached around 250 mm^2, which is more than 20% of the wingbeat cycle-averaged value. In contrast, wing length variation (Fig. 5.8C) is rather small, where peak-to-peak variation is merely slightly more than 6% of the average value. Consequently, the variation in wing surface area is presumably attributed to the spreading of individual feathers in circumferential direction. Feathering angle variation at four spanwise locations shows the twist in 'wash-out' trends (Fig. 5.8D), i.e., the outer sections are more aligned to the disk of rotation (stroke plane). The half-amplitudes during down- and upstroke do not show substantial asymmetry. It is quite interesting that the local camber (normalized by local chord length (measured at mid-chord locations), Fig. 5.8E) shows positive values during downstroke and negative values during upstroke. Note the positive and negative signs correspond to dorsal and ventral sides of the wing, respectively. Thus, in the stroke plane frame, the wing shows convex upward against stroke plane during both strokes. A few exceptions are found in the inner spanwise locations during upstroke, especially in the $0.2R$ (blue line) in late upstroke. This is probably related to the anatomical characteristics, but in terms of aerodynamic force production, the inner portions should have smaller impact due to smaller tangential velocity compared to the outer part of the wing. Local cambers also exhibit slight asymmetry during down- and upstroke. In general, cambers are greater during downstroke. Geometrical angles of attack calculated at mid-chord locations show similar asymmetry tendency (Fig. 5.8F). The angles during downstroke are around 25 ($0.8R$) to 65 ($0.8R$) degrees, whereas during upstroke they are around 20 ($0.8R$) to 50 ($0.8R$) degrees. It should also be noted that during angles are rather stable during downstroke but during upstroke it gradually decreasing. These morphological (camber) and kinematic (AoA) asymmetries might be responsible to the aerodynamic force asymmetry which has been predicted by PIV experiments and also confirmed in the present computation (shown later).

5.3.2 Aerodynamic force and power

Comparison between the models on wingbeat averaged vertical force, power, and vertical force-to-power ratio until 8th wingbeat is summarized in Fig. 5.9 and the numbers in the 8th cycle are listed in Table 5.3. The original wing model with prescribed deformation outperforms the other flat-plate models in vertical force (Fig. 5.6(A)). This is not without cost, though. The original model requires greater power (Fig. 5.6(B)). However, vertical force produced with unit power (F_{v}/P) was greater in the original wing model (Fig. 5.6(C)). Therefore it can be concluded the original, deforming wing is energetically more efficient in generating the usable force. From the instantaneous vertical force plot (Fig. 5.10(C)), three features can be interpreted.

Firstly, the vertical force is always positive with two or three distinct peaks in both downstroke and upstroke. This is common in all the wing models although the number of peaks in downstroke is one in the original model whereas two in the flat-plate models. The positive trend in the vertical force has repeatedly been reported for insects and consistent with the estimation in the hummingbird hovering from PIV (particle image velocimetry) measurement using circulation (Warrick et al., 2005; Wolf et al., 2013). Our results on flat wing models clearly shows the deformation is not a mandatory factor for generating positive vertical force in upstroke but rather a wing kinematics matters.

Secondly, greater force is generated during downstroke than during upstroke while pronation and supination do not contribute to the vertical force. This is again common to all the wing models. Moreover, the fraction of vertical force generated during downstroke and upstroke was approximately 7:3 in all the models (Table 5.3), which again is consistent with the estimations in the experiments (Warrick et al., 2005; Wolf et al., 2013). Also noted is that the vertical force during downstroke is sensitive to the area

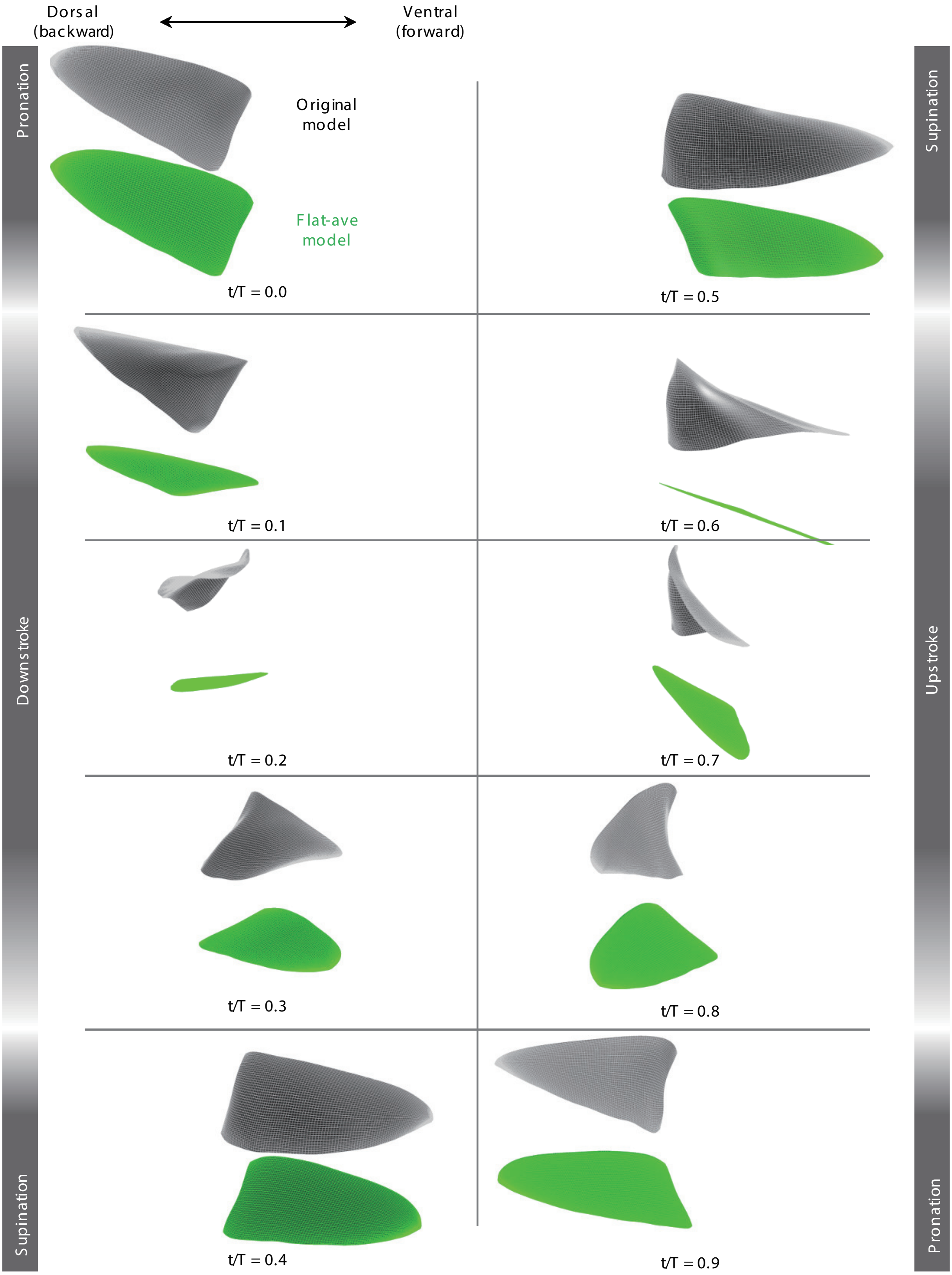

Figure 5.6. Time course morphology and kinematics of model wings. Gray, original model; green, flat-ave model. Viewed from right side and slightly (15 deg) above.

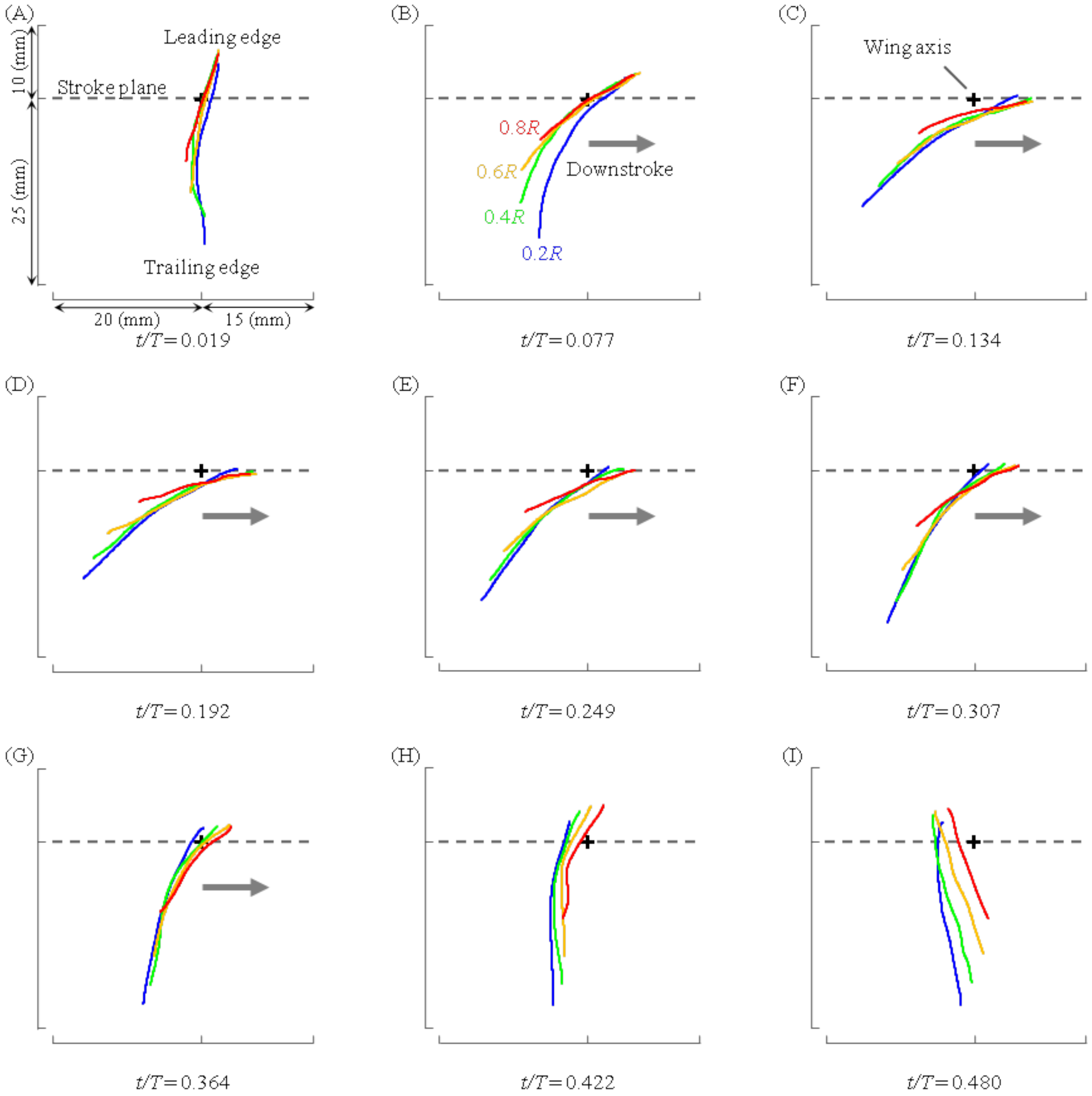

Figure 5.7. Airfoil shapes of right wing grid, illustrating twist and camber simultaneously. The wing is in the wing frame, i.e. the right wing is seen from right wingtip, where wingbase and wingtip are aligned, which is marked as a plus sign, and the horizontal axis (gray dashed line) is the stroke plane. The airfoils at different spanwise locations are marked by colors: blue, $0.2R$; green, $0.4R$; yellow, $0.6R$; and red, $0.8R$. Arrows indicate the downstroke (right arrow) or upstroke (left arrow), not the exact velocity of the particular location on the wing.

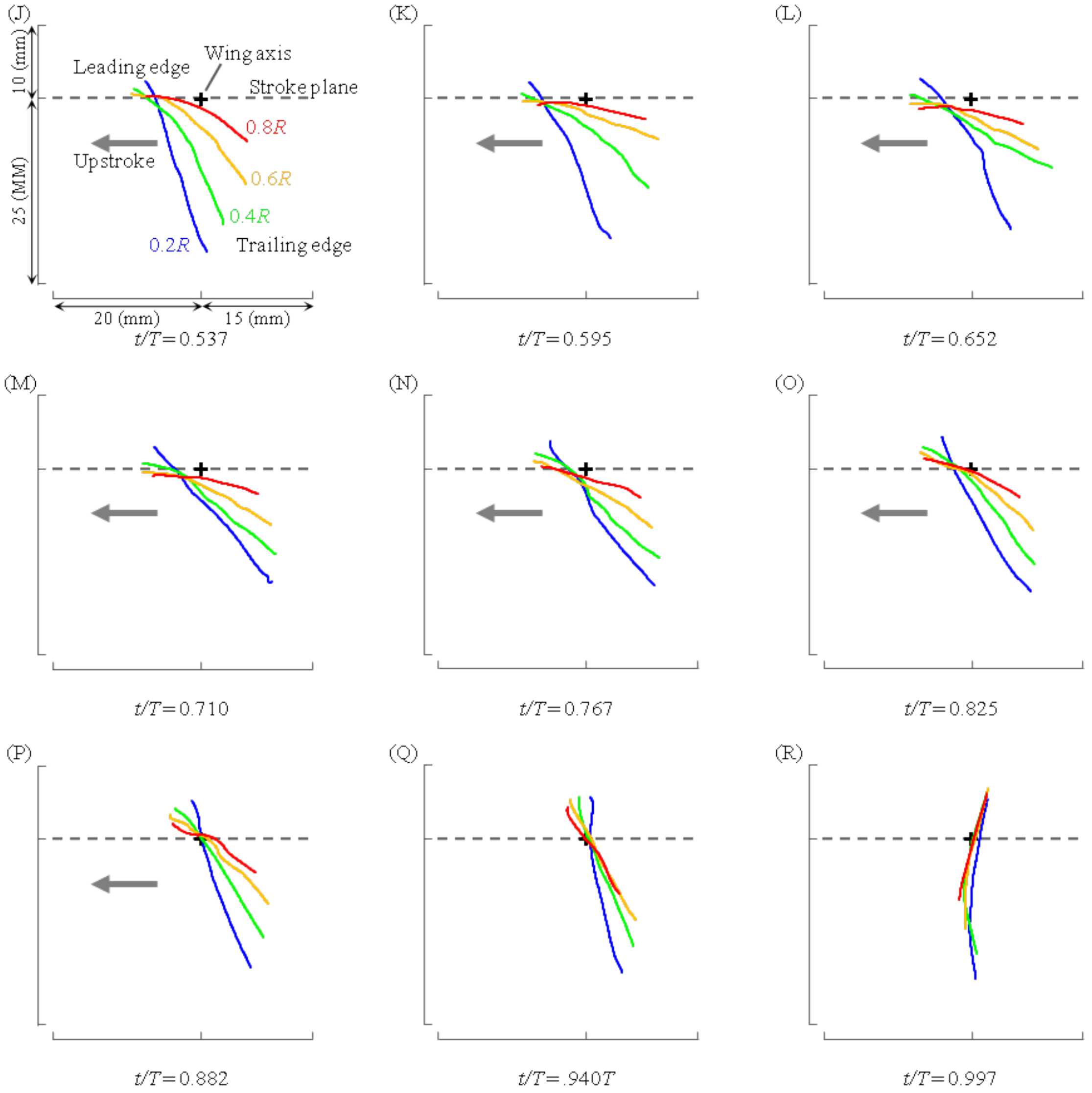

$t/T=0.537$ $t/T=0.595$ $t/T=0.652$

$t/T=0.710$ $t/T=0.767$ $t/T=0.825$

$t/T=0.882$ $t/T=.940T$ $t/T=0.997$

Figure 5.7. Airfoil shapes of right wing grid. (*cont.*)

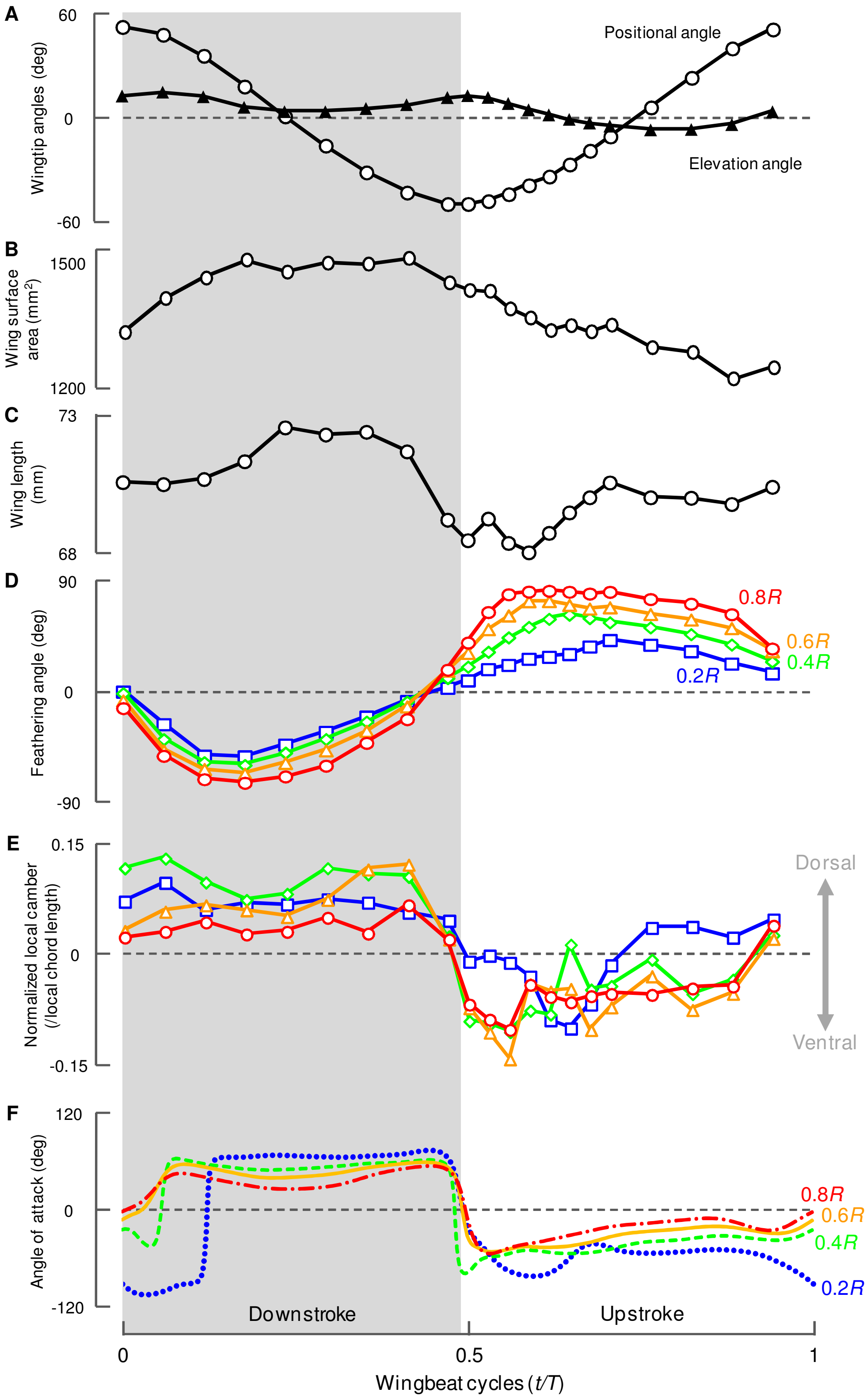

Figure 5.8. Within-wingbeat variations in morphological and kinematic parameters. (A) Wingtip kinematics. Open circles, positional angle; filled triangles, elevation angle. (B) Wing surface area. (C) Wing length. (D) Feathering angles. (E) Local cambers at mid-chord, normalized by local chord length. (F) Geometrical angles of attack at mid-chord. Key to color from (D) to (F): blue, $0.2R$; green, $0.4R$; yellow, $0.6R$; and red, $0.8R$.

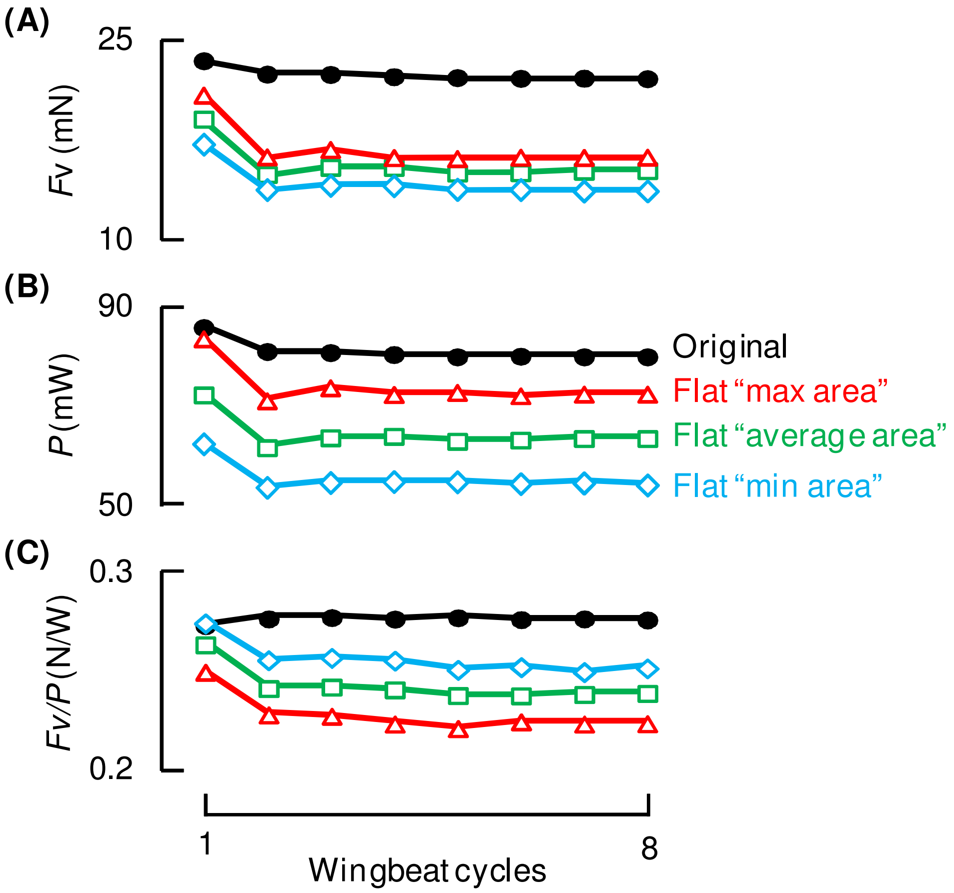

Figure 5.9. Wingbeat cycle averaged vertical force (A), power (B) and vertical force-to-power ratio. Filled black circle, original morphing wing model; open red triangle, flat-max model; open green square, flat-ave model; open blue diamond, flat-min model.

difference but during upstroke the difference among the flat models is relatively small.

Thirdly, the discrepancy between the original model and flat-plate models is largest in the downstroke. Specifically, the force in the flat-plate models seems to be subjected to advanced phase-shift from the original model. The exact reason of this phase difference has not yet been investigated but it is possible the spanwise bending plays some roles.

Instantaneous power generally follows the trend in the vertical force (Fig. 5.10(D)). One large discrepancy between vertical force and power is found in the late upstroke to early downstroke. This means the power is wasted instead of consumed for generating vertical force, which consistent with the wing posture: feathering angle is around zero at pronation. The zero feathering angle means (in our definition) the wing chord is perpendicular to the stroke plane and the stroke plane is almost horizontal (stroke plane angle is less than 15 degrees). However, the wing posture alone cannot explain the discrepancy between original and flat-plate models because they have almost the same posture at that moment (Fig. 5.6). In addition, as stated earlier, the deformation is minimal in the original model during pronation. The visualization

Table 5.3. Comparison of cycle-averaged vertical forces, powers, and vertical force to power ratios between the models in the 8th wingbeat period ($7.0 < t/T \leq 8.0$). The downstroke and upstroke fraction of vertical force ($F_{\mathrm{v,DS}} : F_{\mathrm{v,US}}$) during the 8th wingbeat period is also shown.

Model	$F_{\mathrm{v,ave}}$ (mN)	P_{ave} (mW)	$F_{\mathrm{v,ave}}/P_{\mathrm{ave}}$ (N/W)	$F_{\mathrm{v,DS}} : F_{\mathrm{v,US}}$ (%)
Original	22.1	79.9	0.276	72:28
Flat-max	16.2	72.5	0.223	73:27
Flat-ave	15.2	63.6	0.239	70:30
Flat-min	13.7	54.4	0.251	70:30

of the surface pressure at pronation ($t/T = 8.0$) resolved this paradox, at least partly. In the original model there are weak high and low pressure region on the dorsal surface (Fig. 5.11(A), upper model). The relatively strong low pressure regions are found on the ventral surface, which should have favorable effect because the bird is going to sweep the wing ventrally so the low pressure would help pulling the wing to the same direction as the birds will. In stark contrast, stronger pressures are observed on the both surfaces of the flat-ave wing model (Fig. 5.11, lower models). Both high and low pressure regions are found in both sides, but the low pressure region on the dorsal side is not only large but is locating away from the wingbase compared to the low pressure region on the ventral side. This should therefore result in a torque which is against of the birds preference. The exact cause of the drastic difference in the pressure contour between the models is unknown, but considering that both the wing shape and the wing velocity are not significantly different between the models, aerodynamic hysteresis including wing-wake interaction may well be involved in.

5.3.3 Near-field flow visualization

In this section, as preliminary results, some distinctive features depicted in the visualization of near-field wake and surface pressure are presented (Fig. 5.12). At mid-downstroke ($t/T = 7.24$), formerly formed leading-edge vortex (LEV) split into two (LEV1 and LEV2). In between these LEVs, a weaker contra rotating vortex is found (marked as CRV, counter rotating vortex in Fig. 5.12(A)), which should be corresponding to the smaller counter rotating vortex (SV) in the study by Harbig et al. (Harbig et al., 2013*a*,*b*) As the time advances ($t/T = 7.30$), the LEV1 further split into two and an additional CRV emerges (LEV3 and CRV2 in Fig. 5.12(B)). Adverse (from wingbase to wingtip) and inverse spanwise flows are found corresponding locations of LEV and CRV, respectively (not shown). It is also apparent that the both LEV and CRV contribute to the force generation via creating low pressure region just below the vortices. The dual or more LEVs were previously reported in insect (Srygley and Thomas, 2002) or insect-like flappers (Lu et al., 2006). Here I first time reported a hummingbird wing also exhibits such vortex structures. It can be seen, however, that the existence of these flow structures are not owning

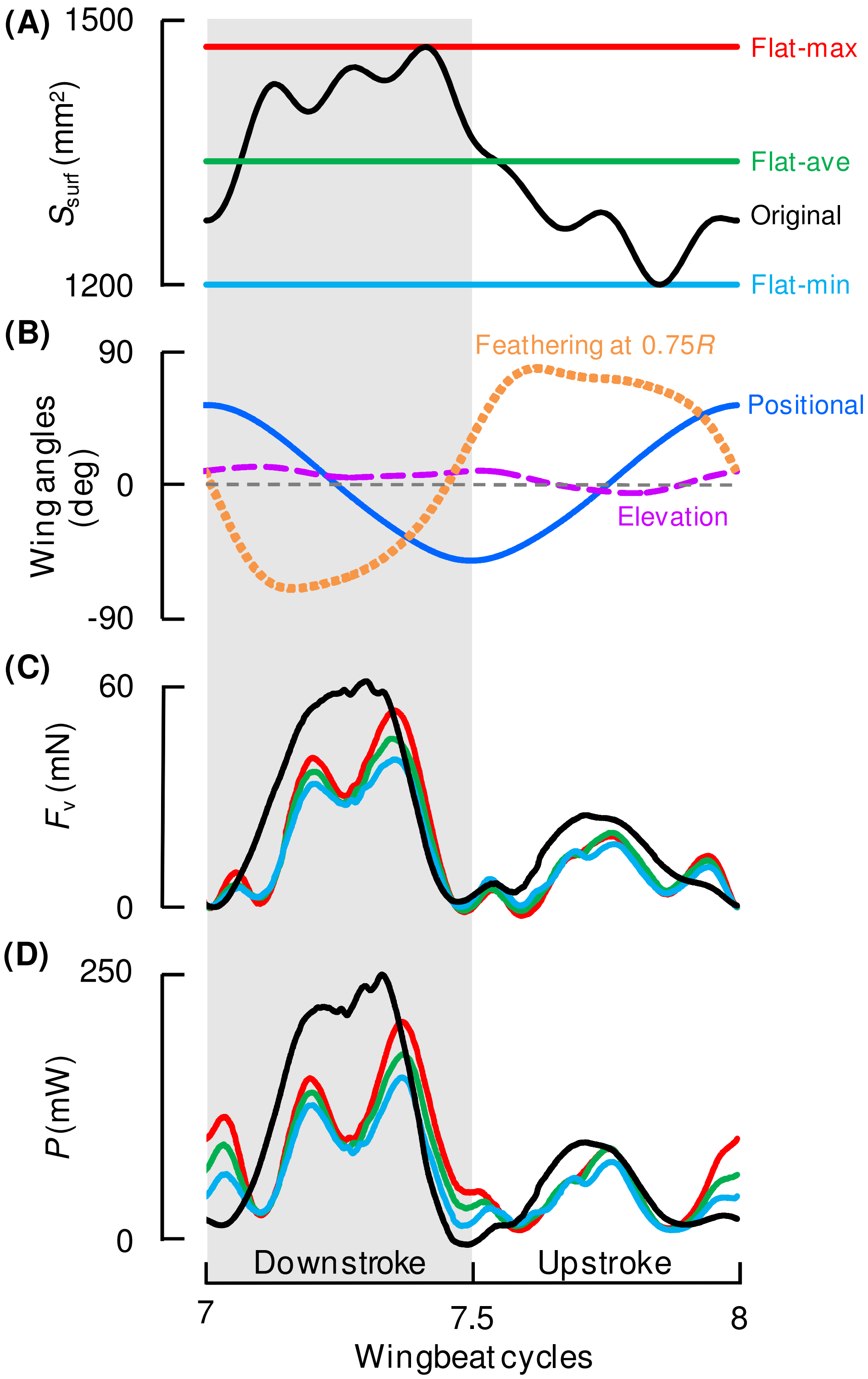

Figure 5.10. Instantaneous vertical force (C) and power (D) during 6th wingbeat period, along with wing area (A) and wing kinematics (B). Shaded region indicates downstroke.

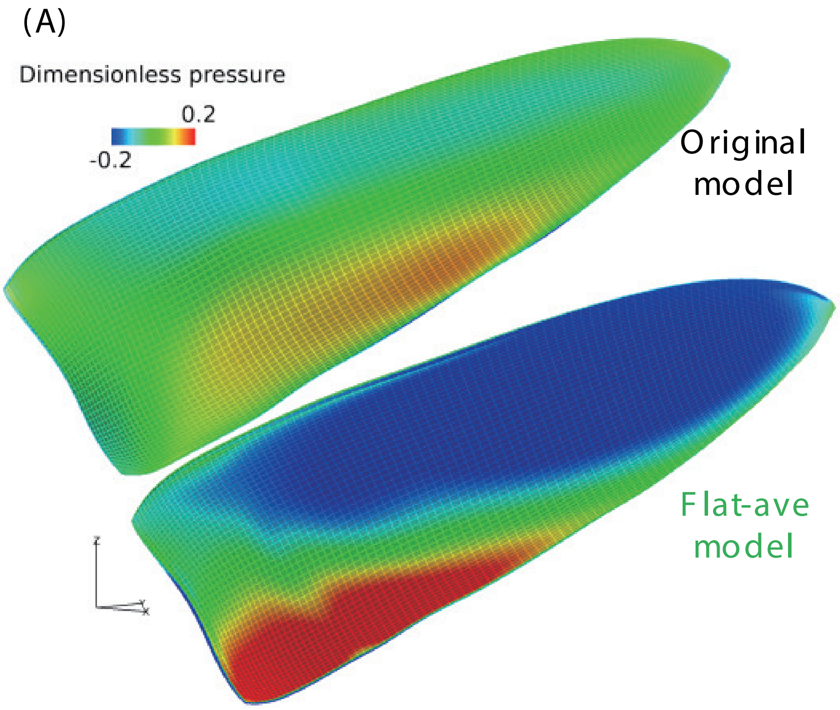

Dorsal (upper, inner) side

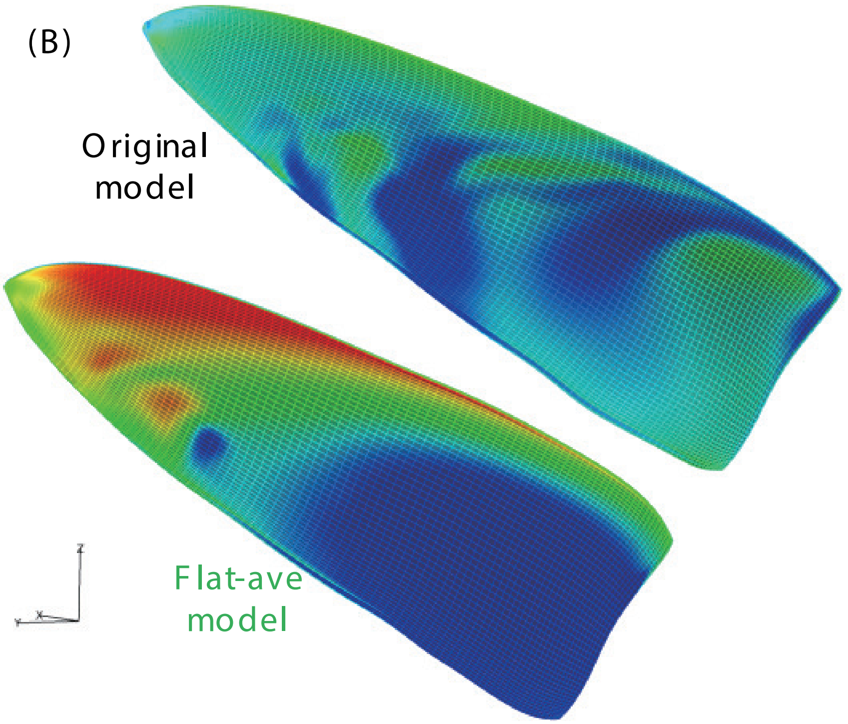

Ventral (lower, outer) side

Figure 5.11. Pressure contours on the wing surfaces at $t/T = 8.0$.

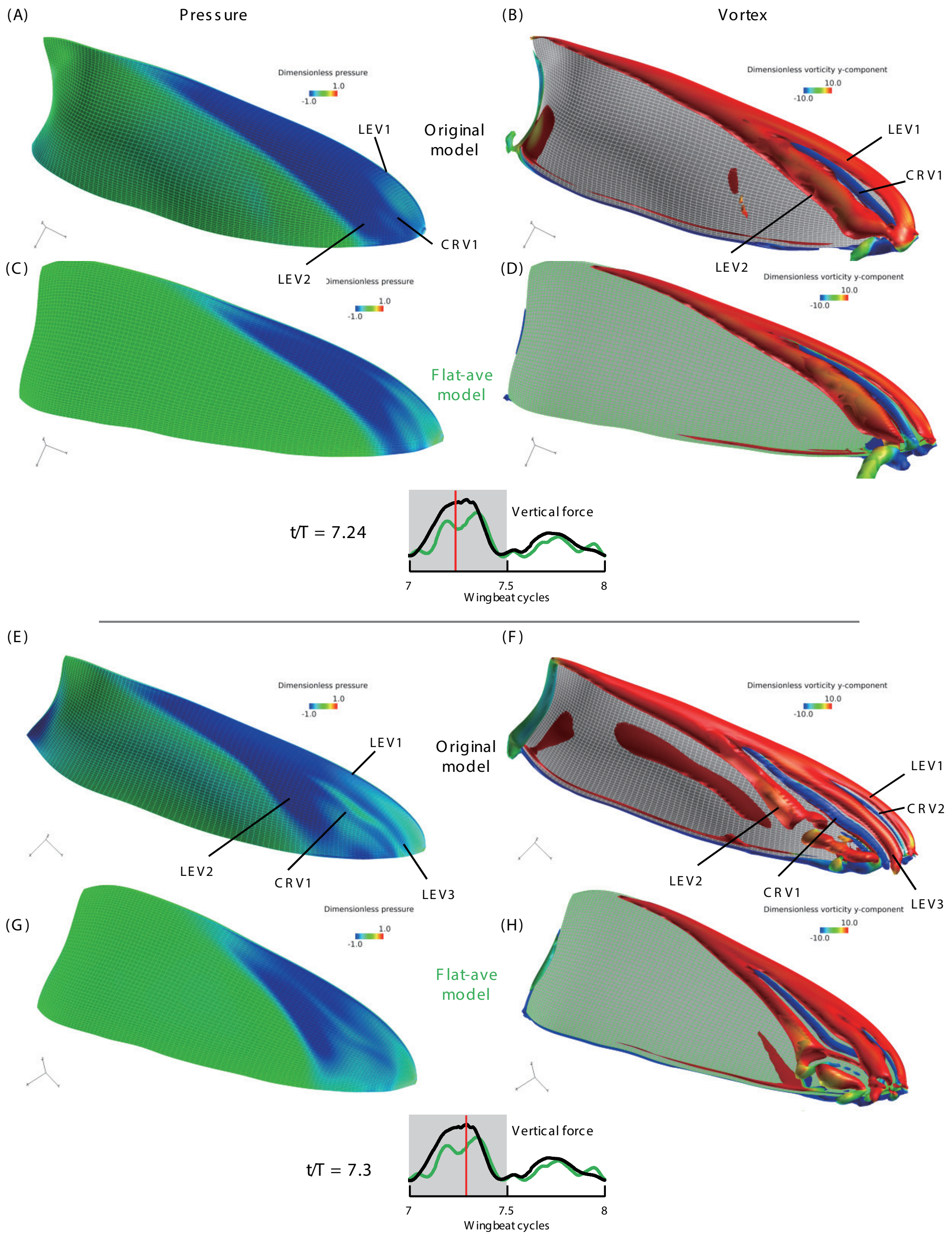

Figure 5.12. Comparison of near field flow fields in the original model and the flat-ave model at $t/T = 7.24$ (A-D) and $t/T = 7.30$ (E-H). (A), (B), (E) and (F) are the original model; (C), (D), (G) and (H) are the flat-ave model. In (A), (C), (E) and (G) dimensionless pressure on the dorsal (upper) surface of the wing are shown. In (B), (D), (F) and (H) Q criterion iso-surfaces at Q = 20 are shown, colored with y-component dimensionless vorticity. Note that y-direction in the Cartesian coordinates almost coincides with wingbase to wingtip direction at these time instances. LEV stands for leading-edge vortex; CRV stands for counter-rotating vortex.

to the wing deformation, because quite similar structures are found in the flat-ave model, although the magnitudes of the wakes are smaller.

5.4 Concluding remarks

We conducted a comparative study on the wing deformation with combination of experiment and numerical methods. The hummingbird wing exhibited substantial deformation during flapping. Specifically, wing area change was around 20 %, but is not accompanied by the variation in wing length, suggesting spreading of each feather. Also twist and resulting angle of attack, as well as camber at most of the spanwise locations seem to be favorable. These findings not only help understanding the bird flight more deeply, but could provide inspiration to the flapping wing flying machines (see e.g. Mahardika et al., 2011).

In the numerical simulation it was found the realistic, dynamically morphing wing outperforms not only in the magnitude of vertical force but more efficiently producing the force than the flat-plate models with a set of given wing kinematics. Flow visualization revealed a characteristic dual- and triple-LEV with counter rotating vortices in between them.

Caution should be taken, though, about the flat wing performance, because the selection of wing kinematics, especially feathering angle used in the present study was rather arbitrary. Although the decrease in the feathering amplitude for the flat wings, which corresponds to the increase in the geometrical angle of attacks during the strokes, would leads to the larger LEVs, it would also substantially increase the power necessary for producing such LEVs. Nevertheless, further investigations would be necessary for confidence.

The deforming wing model itself has a relatively large room, including wing-wing and wing-body interaction (this is currently underway), leading edge sharpness, wing thickness, surface roughness, or air-permeability. For instance, in the rotary wing experiments with a real and several model hummingbird wings, leading edge sharpness and surface properties significantly affected to the lift-to-drag ratio (Altshuler et al., 2004). It is possible these parameters affect in the flapping wings.

References

Altshuler, D. L., Dudley, R. and Ellington, C. P. (2004), 'Aerodynamic forces of revolving hummingbird wings and wing models', *J. Zool.* **264**(4), 327–332.

Harbig, R. R., Sheridan, J. and Thompson, M. C. (2013*a*), 'Relationship between aerodynamic forces, flow structures and wing camber for rotating insect wing planforms', *J. Fluid Mech.* **730**, 52–75.

Harbig, R. R., Sheridan, J. and Thompson, M. C. (2013*b*), 'Reynolds number and aspect ratio effects on the leading-edge vortex for rotating insect wing planforms', *J. Fluid Mech.* **717**, 166–192.

Le, T. Q., Truong, T. V., Park, S. H., Truong, T. Q., Ko, J. H., Park, H. C. and Byun, D. (2013), 'Improvement of the aerodynamic performance by wing flexibility and elytra-hind wing interaction of a beetle during forward flight', *J. R. Soc. Interface* **10**(85), 20130312.

Liu, H. (2009), 'Integrated modeling of insect flight: From morphology, kinematics to aerodynamics', *J. Comput. Phys.* **228**(2), 439–459.

Liu, H. and Aono, H. (2009), 'Size effects on insect hovering aerodynamics: an integrated computational study.', *Bioinspir. Biomim.* **4**(1), 015002.

Lu, Y., Shen, G. X. and Lai, G. J. (2006), 'Dual leading-edge vortices on flapping wings.', *J. Exp. Biol.* **209**, 5005–5016.

Mahardika, N., Viet, N. Q. and Park, H. C. (2011), 'Effect of outer wing separation on lift and thrust generation in a flapping wing system.', *Bioinspir. Biomim.* **6**(3), 036006.

Nakata, T. and Liu, H. (2012), 'Aerodynamic performance of a hovering hawkmoth with flexible wings: a computational approach.', *Proc. R. Soc. B* **279**(1729), 722–731.

Nakata, T., Liu, H., Tanaka, Y., Nishihashi, N., Wang, X. and Sato, A. (2011), 'Aerodynamics of a bio-inspired flexible flapping-wing micro air vehicle.', *Bioinspir. Biomim.* **6**(4), 045002.

Srygley, R. B. and Thomas, A. L. R. (2002), 'Unconventional lift-generating mechanisms in free-flying butterflies.', *Nature* **420**(6916), 660–664.

Tobalske, B. W. (2010), 'Hovering and intermittent flight in birds', *Bioinspir. Biomim.* **5**(4), 045004.

Tobalske, B. W., Warrick, D. R., Clark, C. J., Powers, D. R., Hedrick, T. L., Hyder, G. A. and Biewener, A. A. (2007), 'Three-dimensional kinematics of hummingbird flight', *J. Exp. Biol.* **210**, 2368–2382.

Warrick, D. R., Tobalske, B. W. and Powers, D. R. (2005), 'Aerodynamics of the hovering hummingbird', *Nature* **435**(7045), 1094–1097.

Wolf, M., Ortega-Jiménez, V. M. and Dudley, R. (2013), 'Structure of the vortex wake in hovering Anna's hummingbirds (Calypte anna)', *Proc. R. Soc. B* **280**, 20132391.

Young, J., Walker, S. M., Bomphrey, R. J., Taylor, G. K. and Thomas, A. L. R. (2009), 'Details of insect wing design and deformation enhance aerodynamic function and flight efficiency', *Science* **325**(5947), 1549–1552.

Zheng, L., Hedrick, T. L. and Mittal, R. (2013*a*), 'A multi-fidelity modelling approach for evaluation and optimization of wing stroke aerodynamics in flapping flight', *J. Fluid Mech.* **721**, 118–154.

Zheng, L., Hedrick, T. L. and Mittal, R. (2013*b*), 'Time-varying wing-twist improves aerodynamic efficiency of forward flight in butterflies', *PLoS One* **8**(1), e53060.

Chapter 6

Conclusions and future tasks

6.1 Concluding remarks

In the present paper, three different natures flyers (fruit fly, butterfly, and hummingbird) spanning a broad range of Reynolds number regime (order of magnitude from 10^2 to 10^4) in four different natural flight situations (turning, hovering near ground, takeoff, hovering midair for feeding) have been studied with the aid of computational fluid dynamics as well as high speed video cameras in the latter two situations.

From auto-stabilization simulation of fruit fly (Chapter 2), significant contribution of flapping counter torque (FCT) in yaw damping was confirmed, but the extent of which was found to be stronger than expected from a simpler blade-element computation. This deviation has partially resolved by examining the accurate condition of the blade-element method but not fully explained. The discrepancy between the current numerical simulation and observation suggests the existence of active control in the end phase of turning in the natural flight conditions, where translational degrees of freedom could lead to instability due to flapping counter force (FCF), which was supported by the instability in the other (roll and pitch) attitudes in the 6 DoF computation.

From ground effect simulation (Chapter 3), it was found that the body generates non-negligible amount of useful (vertical) aerodynamic force when hovering close to ground. The force augmentation is mainly due to the high pressure region below the body, which was confirmed via flow visualization and pressure contour of the body. The wings, rather unexpectedly, are almost unaffected by the ground at this height (distance from ground to wingbase is 0.8 times the wing length). The variation of the ground effect was also performed by changing the height. The results showed the coincidence with the curve from helicopter theory, which needs further examination.

From butterfly takeoff simulation (Chapter 4), it was found the leg thrust can reach up to 8 times larger vertical force compared to aerodynamic forces. In contrast, the presence of ground has almost no effect in aerodynamic forces. This illustrates little contribution from ground in at least certain types of rapid takeoff (escape takeoffs), i.e. if leg thrust is strong enough, there is no ground effect and possibly *vice versa*. Further examination of the dependency of ground effect to leg thrust strength is already underway as a collaboration study.

From wing deformation study of hummingbird hovering (Chapter 5), it is now clear the wings of a hummingbird do exhibit significant deformations not in wing length but in other morphological parameters. Specifically, the wing has substantial twist during flapping in the washout manner, with significant camber (chordwise bending). Surface area exhibited 20 % peak-to-peak variation, which is the result of spreading the feathers. A preliminary fluid dynamics simulation comparing real and flat wing models suggests the deformation can be energetically more efficient, while providing greater aerodynamic forces. It also confirmed the expected 70%:30% vertical force ratio during downstroke and upstroke, respectively.

The numbers obtained in the present studies might not always seem to be appealing enough at the first glance (e.g. +8.5% lift by fruit fly body in ground effect; +16% improvement in lift/power for a dynamically deforming wing over a flat wing in hummingbird). However, in the engineering context, 10% improvement in TSFC (thrust specific fuel consumption) on a gas turbine engine would be regarded as a huge leap. Also, considering the evolutionary path of the flight animals, even the slightest improvements can be beneficial in survival. Examples for such evolutionary benefit includes the famous Darwin's Finch (Grant and Grant, 2008).

6.2 Future directions

Numbers of issues related to flapping flight still remain to be unraveled. The consideration of external environments examined in this research are just a few of them. There could be several directions in the future study of animal flapping flights.

The deeper understandings of the hot topics including wing deformation or stability & control problems are still lacking. For example, our knowledge on how exactly the flying animals are transitioning between low and high speeds are far from complete, although there are several attempts being made (e.g. Isogai and Kawabe, 2010).

The multi-physics or multi-scale coupling may be the next step. The former includes the consideration of skeletomuscular system or physiological responses (e.g. visual or odor sensing, EMG recordings of muscle activity (e.g. Biewener, 2011), or visualizing thermoregulation via infra-red video (e.g. Ward et al., 1999; McCafferty et al., 2011), etc.) and combining them with the flapping flight models such as the one in our groups. The latter includes the elucidation of the microstructure or air-permeability effect on the boundary layer of the wing surface (see e.g. Altshuler et al., 2004; Bachmann et al., 2007; Ito, 2009; Eder et al., 2010; Elimelech and Ellington, 2013; Kovalev et al., 2014) or gaps between feathers (e.g. Inada et al., 2013).

Yet another direction is the collaboration between the slightly distant, possibly non-biomechanics biological research fields. This includes navigation (bio-logging the long range trip or migration with GPS and/or accelerometer, e.g. Sato et al., 2007; Watanabe et al., 2011) or evolution of flight but not necessarily restricted to them, for example, environmental problem could also be the target. One such example is the environmental assessment of the effect of wind turbines on the flying animals: not only birds but bats also are killed by wind turbines recently. Engineers are trying to solve this issue by altering wing turbine itself, but possibly biological researchers would be of great help by e.g. estimating the maneuverability and predicting the behavior.

Other examples include sound generation by feathers (e.g. Clark et al., 2011), flying in the rain (Ortega-Jiménez and Dudley, 2012*b*,*a*) or snow. For the latter I do not know of any experiment on insects or birds possibly because flapping wings do not seem to suffer from snow or ice. But considering icing is one of the most important problems in aviation (e.g. Air France Flight 447), elucidation of anti-ice/de-ice mechanisms in animals in general may be intriguing.

References

Altshuler, D. L., Dudley, R. and Ellington, C. P. (2004), 'Aerodynamic forces of revolving hummingbird wings and wing models', *J. Zool.* **264**(4), 327–332.

Bachmann, T., Klän, S., Baumgartner, W., Klaas, M., Schröder, W. and Wagner, H. (2007), 'Morphometric characterisation of wing feathers of the barn owl Tyto alba pratincola and the pigeon Columba livia', *Front. Zool.* **4**, 23.

Biewener, A. A. (2011), 'Muscle function in avian flight: achieving power and control', *Philos. Trans. R. Soc. B* **366**(1570), 1496–1506.

Clark, C. J., Elias, D. O. and Prum, R. O. (2011), 'Aeroelastic Flutter Produces Hummingbird Feather Songs', *Science* **333**(6048), 1430–1433.

Eder, H., Fiedler, W. and Pascoe, X. (2010), 'Air-permeable hole-pattern and nose-droop control improve aerodynamic performance of primary feathers', *J. Comp. Physiol. A* .

Elimelech, Y. and Ellington, C. P. (2013), 'Analysis of the transitional flow field over a fixed hummingbird wing', *J. Exp. Biol.* **216**, 303–318.

Grant, P. R. and Grant, B. R. (2008), *How and why species multiply: the radiation of Darwin's finches*, Princeton University Press.

Inada, Y., Watanabe, D. and Kurihara, J. (2013), 'Effect of Gap between Primary Feathers on Bending Moment of a Bird-like Assembled Wing', *J. Aero Aqua Bio-mechanisms* **3**(1), 8–12.

Isogai, K. and Kawabe, H. (2010), 'Transition Flight Simulation of Flapping-Wing Micro-Aerial Vehicle Using Aerodynamic Database', *Trans. Jpn. Soc. Aeronaut. Space Sci.* **53**(180), 138–146.

Ito, S. (2009), 'Aerodynamic Influence of Leading-Edge Serrations on an Airfoil in a Low Reynolds Number', *J. Biomech. Sci. Eng.* **4**(1), 117–123.

Kovalev, A., Filippov, A. E. and Gorb, S. N. (2014), 'Unzipping bird feathers.', *J. R. Soc. Interface* **11**(92), 20130988.

McCafferty, D. J., Gilbert, C., Paterson, W., Pomeroy, P. P., Thompson, D., Currie, J. I. and Ancel, A. (2011), 'Estimating metabolic heat loss in birds and mammals by combining infrared thermography with biophysical modelling.', *Comp. Biochem. Physiol. A* **158**(3), 337–345.

Ortega-Jiménez, V. M. and Dudley, R. (2012*a*), 'Aerial shaking performance of wet Anna's hummingbirds', *J. R. Soc. Interface* **9**(70), 1093–9.

Ortega-Jiménez, V. M. and Dudley, R. (2012*b*), 'Flying in the rain: hovering performance of Anna's hummingbirds under varied precipitation', *Proc. R. Soc. B* **279**(1744), 3996–4002.

Sato, K., Watanuki, Y., Takahashi, A., Miller, P. J. O., Tanaka, H., Kawabe, R., Ponganis, P. J., Handrich, Y., Akamatsu, T., Watanabe, Y., Mitani, Y., Costa, D. P., Bost, C.-A., Aoki, K., Amano, M., Trathan, P., Shapiro, A. and Naito, Y. (2007), 'Stroke frequency, but not swimming speed, is related to body size in free-ranging seabirds, pinnipeds and cetaceans', *Proc. R. Soc. B* **274**(1609), 471–477.

Ward, S., Rayner, J. M. V., MOLler, U., Jackson, D. M., Nachtigall, v. W. and Speakman, J. (1999), 'Heat transfer from starlings sturnus vulgaris during flight', *J. Exp. Biol.* **202**, 1589–1602.

Watanabe, Y. Y., Takahashi, A., Sato, K., Viviant, M. and Bost, C.-A. (2011), 'Poor flight performance in deep-diving cormorants', *J. Exp. Biol.* **214**, 412–421.

Appendix A

Fluid dynamics solver

A.1 Basic equations

The computational fluid dynamic method used in this study is a finite volume method-based Navier-Stokes solver specified for a multi-blocked, overset-grid system, which has been validated by showing various applications to insect flapping flights (Liu and Aono, 2009; Liu, 2005) as well as to a flapping wing micro air vehicle (Nakata et al., 2011). The governing equations are the three-dimensional, incompressible, unsteady Navier-Stokes equations written in strong conservation form for mass and momentum, with artificial compressibility method applied. The governing equation in dimensionless form is:

$$\int\limits_{V_{\mathrm{cv}}(t)} \frac{\partial \mathbf{q}}{\partial \hat{t}} \mathrm{d}V + \frac{\partial}{\partial t} \int\limits_{V_{\mathrm{cv}}(t)} \mathbf{Q} \mathrm{d}V + \oint\limits_{S_{\mathrm{cv}}(t)} (\mathbf{f} - \mathbf{Q}\mathbf{u}_{\mathrm{g}}) \cdot \mathbf{n} \mathrm{d}S = 0 \tag{A.1}$$

where

$$\mathbf{q}=\begin{bmatrix}u\\v\\w\\0\end{bmatrix},\ \mathbf{Q}=\begin{bmatrix}u\\v\\w\\p\end{bmatrix},\ \mathbf{f}=\begin{bmatrix}\mathbf{f}+\mathbf{f}_{\text{vis}}\\\mathbf{G}+\mathbf{G}_{\text{vis}}\\\mathbf{H}+\mathbf{H}_{\text{vis}}\end{bmatrix},\ \mathbf{F}=\begin{bmatrix}u^2+p\\uv\\uw\\\beta u\end{bmatrix},\ \mathbf{G}=\begin{bmatrix}vu\\v^2+p\\vw\\\beta v\end{bmatrix},\ \mathbf{H}=\begin{bmatrix}wu\\wv\\w^2+p\\\beta w\end{bmatrix},$$

$$\mathbf{F}_{\text{vis}}=-\frac{1}{\text{Re}}\begin{bmatrix}2\frac{\partial u}{\partial x}\\\frac{\partial u}{\partial y}+\frac{\partial v}{\partial x}\\\frac{\partial u}{\partial z}+\frac{\partial w}{\partial x}\\0\end{bmatrix},\ \mathbf{G}_{\text{vis}}=-\frac{1}{\text{Re}}\begin{bmatrix}\frac{\partial v}{\partial x}+\frac{\partial u}{\partial y}\\2\frac{\partial v}{\partial y}\\\frac{\partial v}{\partial z}+\frac{\partial w}{\partial y}\\0\end{bmatrix},\ \mathbf{H}_{\text{vis}}=-\frac{1}{\text{Re}}\begin{bmatrix}\frac{\partial w}{\partial x}+\frac{\partial u}{\partial z}\\\frac{\partial w}{\partial y}+\frac{\partial v}{\partial z}\\2\frac{\partial w}{\partial z}\\0\end{bmatrix} \tag{A.2}$$

Here, $V(t)$ is an arbitrary deformable control volume; $S(t)$ is the surface of the control volume; t is physical time; τ is pseudo time; $\mathbf{n}$ is the unit outward normal vector; u_{g} is the local velocity of the moving cell surface; u, v, and w are velocity components in the Cartesian coordinate system x, y and z; p is pressure; λ is the pseudo-compressibility coefficient; and Re is Reynolds number. Aerodynamic force and aerodynamic power (time rate of work done to the surrounding air by the flyer) for each wing and body are defined as (Liu, 2009):

$$\mathbf{F_{aero}}=\begin{bmatrix}F_{\text{x}}\\F_{\text{y}}\\F_{\text{z}}\end{bmatrix}=\sum_i^N(\mathbf{Flux}_{\text{invis}}+\mathbf{Flux}_{\text{vis}}),\ P=\sum_i^N(\mathbf{F_{aero}}\cdot\mathbf{v}_{\text{surf},i}) \tag{A.3}$$

where N denotes number of the cells on the surface of the wing or the body, $\mathbf{Flux}_{\text{invis}}$ and $\mathbf{Flux}_{\text{vis}}$ are the inviscid and viscous fluxes, respectively, and v_{surf} is the velocity of the cell face on the surfaces.

To evaluate how efficiently the flyer generates forces, the vertical force divided by aerodynamic power (both are averaged over one wingbeat cycle) is defined as vertical force-to-power ratio $F_{\text{z,ave}}/P_{\text{ave}}$, similarly as used by Zheng et al. (Zheng et al., 2013) on a numerical simulation of butterfly forward flight.

A.2 Modifications to the original solver

The core of the fluid dynamics solver used in the current paper is essentially the same as what Liu developed (Liu, 2009). Nevertheless, I, with the aid of the colleagues (Naoshi Nishihashi and Gao Na), introduced a few modifications, which are essential for the present paper and are explained in this section.

Instead of an O-O type spherical grid, a Cartesian grid is employed as the background (global) grid block, in which a body grid and two wing grids are immersed in. This has a few advantages over the spherical grid: it is convenient for introducing a virtual ground surface; the uniform grid spacing around the flyer's grid blocks (body and wings) can be used, enabling the grids less affected by the numerical diffusion; and there is no need of boundary connection, i. e. in an O-O grid system, one must 'connect' the first and last grid points (or cells) to achieve periodical boundary in the $i-$ and $j-$ directions, which requires additional treatment in those regions.

The Cartesian grid has the two regions: clustering region which has small, uniform grid spacing (i. e. small cubic cells) and the non-uniform spacing region. Usually the clustered region is placed in the middle of the domain, and the outer boundaries of any flyer blocks are immersed in this region to prevent the loss of accuracy during the interpolation between the local (flyer's) blocks and global (Cartesian) block.

During the coupling computation with the simplified rigid body dynamics (sRBD) solver, the flyer grid moves. To ensure the flyer grid blocks are always confined to the clustering region of the Cartesian grid block, the location of the flyer's center of mass is always tracked. When the deviation exceeds the uniform grid spacing (i. e. length of a side of the cube in the clustering region), the Cartesian grid is re-meshed. For example, if the clustering region in $i-$direction is from lth to mth cells (with uniform spacing $\mathrm{d}s$) and the movement of the flyer's center of mass from the last re-meshing in the $i-$direction exceeds $\mathrm{d}s$ (assuming that the direction is from lth cell to mth cells), the lth cells are removed and newer cells are generated just outside of the mth cells. The flow variables of the new cells are interpolated from the mth and $(m+1)$th cells. Currently the linear interpolation is used for simplicity. More rigorous methods can be used, but since these outer boundaries of the clustering regions (in the present example, lth or mth cells) should locate sufficiently far from the flyer's blocks, the error due to the selection of interpolation methods may not be as large. The similar 'watchings' are performed in $j-$ and $k-$ directions.

Another notable difference between the previous solver in the source-code level is that I migrated the code from FORTRAN 77 to Fortran 90 (with the aid from Naoshi Nishihashi). This is no minor change, because the adoption of module structure dramatically improves the subsequent integration of new features, which include not only rigid body dynamics & prescribed wing deformation in the current study (the latter was developed with Toshiyuki Nakata), but wing shape-optimizaion (by Naoshi Nishihashi), PID-control (by Gao Na), flexible dynamics solver (with Ryusuke Noda), or fluid-structure interaction (by Toshiyuki Nakata). Therefore, migration to Fortran 90 was the inevitable foundation for achieving the current, fruitful multi-physics flapping flight simulator.

Also several (what looks to be, at first glance) 'minor' bugs were fixed during the migration process.

For example, there was a slight asymmetry between right and left wings in the original code. The difference is so small that it does not affect any results or conclusion of the previous studies for tethered flight (e.g. Liu and Aono, 2009). However, it does have a detrimental effect when combined to dynamics solver, because the slightest asymmetry is usually amplified via positive feedback loop. For example, a simple hovering computation under the coupling of CFD and sRBD should result in the pitching instability (nose-up or nose-down divergence) but with the slight asymmetry in the CFD the insect went into the spiral mode. This was partly because the usual insect has lower moment of inertia in the roll axis in the body frame. Therefore sensitive to the sideways asymmetry. Another correction was made for the reproduction process of model wing grid kinematics for elevation (deviation) angle. Usually the amplitude of elevation angle is small therefore this has a minimal effect on the aerodynamic forces. Again, however, when it comes to free flight, the slight change in the aerodynamic torque accompanied with this could results in the difference in e.g. pitching attitude.

References

Liu, H. (2005), 'Simulation-Based Biological Fluid Dynamics in Animal Locomotion', *Appl. Mech. Rev.* **58**(4), 269–282.

Liu, H. (2009), 'Integrated modeling of insect flight: From morphology, kinematics to aerodynamics', *J. Comput. Phys.* **228**(2), 439–459.

Liu, H. and Aono, H. (2009), 'Size effects on insect hovering aerodynamics: an integrated computational study.', *Bioinspir. Biomim.* **4**(1), 015002.

Nakata, T., Liu, H., Tanaka, Y., Nishihashi, N., Wang, X. and Sato, A. (2011), 'Aerodynamics of a bio-inspired flexible flapping-wing micro air vehicle.', *Bioinspir. Biomim.* **6**(4), 045002.

Zheng, L., Hedrick, T. L. and Mittal, R. (2013), 'Time-varying wing-twist improves aerodynamic efficiency of forward flight in butterflies', *PLoS One* **8**(1), e53060.

Appendix B

Simplified rigid body dynamics solver

B.1 Basic equations of motion

Translational motion and attitude change are realized by solving the equations of motion for a rigid body. The flapping flyer, either insect, bird, or micro air vehicle with a body and two or more wings, is assumed to be a single rigid body. The flapping motion is not explicitly considered in the present solver. Instead, the location of the center of mass and the amount of moment of inertia tensol must be obtained it viatime averaging. This is why I call this a "simplified" rigid body dynamics (sRBD) solver. The strength of this method are the straightforward derivation and the easiness of implementation in programming.

The equations of motion of a single rigid body can be written as follows (Maeda et al., 2010):

$$M\dot{\mathbf{V}} = \mathbf{F}_{\text{aero}} + \mathbf{F}_{\text{grav}}, \tag{B.1}$$

$$\mathbf{J}'\dot{\boldsymbol{\Omega}}' + \tilde{\boldsymbol{\Omega}}'\mathbf{J}'\boldsymbol{\Omega}' = \mathbf{N}'_{\text{aero}}. \tag{B.2}$$

Eq. (B.1) is equations of translational motion and eq. (B.2) is equations of rotational motion, where M is total mass of the flyer (body mass + wing masses), $\mathbf{V} = [V_{\text{x}}, V_{\text{y}}, V_{\text{z}}]^T$ is flight velocity at the center of mass, $\mathbf{F}$ is applied (external) force, $\mathbf{J}' = [J'_{\text{x}}, J'_{\text{y}}, J'_{\text{z}}]^T$ is wingbeat cycle-averaged moment of inertia of the flyer, $\boldsymbol{\Omega}' = [\Omega'_{\text{x}}, \Omega'_{\text{y}}, \Omega'_{\text{z}}]^T$ is angular velocity, and $\mathbf{N}' = [N'_{\text{x}}, N'_{\text{y}}, N'_{\text{z}}]^T$ is aerodynamic torque. Note that the variables with primes are in the body frame, whereas those without primes are in the inertial (global) frame. The terms with dots are time derivatives. The tilde over the angular velocity term in Eq. (B.2) is an operator to create a 3×3 skew symmetric matrix from a 3×1 matrix:

$$\tilde{\boldsymbol{\Omega}}' = \begin{bmatrix} 0 & -\Omega'_{\mathrm{z}} & \Omega'_{\mathrm{y}} \\ \Omega'_{\mathrm{z}} & 0 & -\Omega'_{\mathrm{x}} \\ -\Omega'_{\mathrm{y}} & \Omega'_{\mathrm{x}} & 0 \end{bmatrix} . \tag{B.3}$$

The wingbeat cycle-averaged moment of inertia tensol is defined as

$$\mathbf{J}' = \begin{bmatrix} J'_{\mathrm{xx}} & J'_{\mathrm{xy}} & J'_{\mathrm{xz}} \\ J'_{\mathrm{yx}} & J'_{\mathrm{yy}} & J'_{\mathrm{yz}} \\ J'_{\mathrm{zx}} & J'_{\mathrm{zy}} & J'_{\mathrm{zz}} \end{bmatrix} \simeq \begin{bmatrix} J'_{\mathrm{x}} & 0 & 0 \\ 0 & J'_{\mathrm{y}} & 0 \\ 0 & 0 & J'_{\mathrm{z}} \end{bmatrix} . \tag{B.4}$$

Here, the off-diagonal terms are approximated as zero, which can be justified because they are usually more than one order of magnitude smaller when the body axes are selected as the body frame.

Usually the right hand sides of eqs. B.1 and B.2, the applied force and applied torque, are composed of aerodynamic and gravitational contributions, i.e.,

$$\mathbf{F} = \mathbf{F}_{\mathrm{aero}} + \mathbf{F}_{\mathrm{grav}} = \begin{bmatrix} F_{\mathrm{aero,x}} \\ F_{\mathrm{aero,y}} \\ F_{\mathrm{aero,z}} \end{bmatrix} + \begin{bmatrix} 0 \\ 0 \\ F_{\mathrm{grav,z}} \end{bmatrix} \tag{B.5}$$

and

$$\mathbf{N}' = \mathbf{N}'_{\mathrm{aero}} = \begin{bmatrix} N'_{\mathrm{aero,x'}} \\ N'_{\mathrm{aero,y'}} \\ N'_{\mathrm{aero,z'}} \end{bmatrix} \tag{B.6}$$

where $\mathbf{F}_{\mathrm{aero}}$ and $\mathbf{F}_{\mathrm{grav}}$ are aerodynamic and gravitational forces and $\mathbf{N}'_{\mathrm{aero}}$ aerodynamic torque. The aerodynamic force and torque are computed in and transferred from the flow solver. The gravitational force is $F_{\mathrm{grav,z}} = -Mg$ where g is gravitational acceleration (on Earth surface g is set as 9.80665 or more simply as 9.81; by reducing g one can handily perform free flight in orbit or on another celestial object). Note by definition the sum of torques due to gravitational acceleration around center of mass become zero. In Chapter 2 the applied forces and torque are as shown here, but in Chapter 4 there are additional forces and torque are introduced for takeoff simulation.

B.2 Coupling

Before solving eqs. (B.1) and (B.2), gravitational acceleration g (normally set as 9.80665 m/s^2), total mass M, and wingbeat cycle-averaged moment of inertia $\mathbf{J}'$ must be given *a priori*. The aerodynamic force $\mathbf{F}$ and aerodynamic torque $\mathbf{N}$ must be computed in and transferred from the flow (CFD) solver. By solving eqs. (B.1) and (B.2), the flyer's velocity $\mathbf{V}$ and angular velocity $\boldsymbol{\Omega}'$ are obtained.

For coupling with the CFD solver, the position and the attitude of the flyer are also necessary. To obtain them, accompanying equations must be solved. The translational equation is

$$\dot{\mathbf{R}} = \mathbf{V} \tag{B.7}$$

and the rotational equation is

$$\dot{\mathbf{E}} = \frac{1}{2}\mathbf{S}^T\boldsymbol{\Omega}' \tag{B.8}$$

where $\mathbf{E} = [\varepsilon_0, \varepsilon_1, \varepsilon_2, \varepsilon_3]^T$ is a set of unit quaternion (also known as Euler parameters) and S is the matrix

$$\mathbf{S} = \begin{bmatrix} -\varepsilon_1 & \varepsilon_0 & \varepsilon_3 & -\varepsilon_2 \\ -\varepsilon_2 & -\varepsilon_3 & \varepsilon_0 & \varepsilon_1 \\ -\varepsilon_3 & \varepsilon_2 & -\varepsilon_1 & \varepsilon_0 \end{bmatrix}. \tag{B.9}$$

The system of equations for time-marching are:

$$\frac{\mathrm{d}}{\mathrm{d}t_{\mathrm{dyn}}} \begin{bmatrix} R_{\mathrm{x}} \\ R_{\mathrm{y}} \\ R_{\mathrm{z}} \end{bmatrix} = \begin{bmatrix} V_{\mathrm{x}} \\ V_{\mathrm{y}} \\ V_{\mathrm{z}} \end{bmatrix}, \tag{B.10}$$

$$\frac{\mathrm{d}}{\mathrm{d}t_{\mathrm{dyn}}} \begin{bmatrix} V_{\mathrm{x}} \\ V_{\mathrm{y}} \\ V_{\mathrm{z}} \end{bmatrix} = \begin{bmatrix} F_{\mathrm{x}} \\ F_{\mathrm{y}} \\ F_{\mathrm{z}} \end{bmatrix} \tag{B.11}$$

for translational motion and

$$\frac{\mathrm{d}}{\mathrm{d}t_{\mathrm{dyn}}}\begin{bmatrix}\varepsilon_0\\ \varepsilon_1\\ \varepsilon_2\\ \varepsilon_3\end{bmatrix}=\frac{1}{2}\begin{bmatrix}-\varepsilon_1\Omega'_{\mathrm{x}}-\varepsilon_2\Omega'_{\mathrm{y}}-\varepsilon_3\Omega'_{\mathrm{z}}\\ \varepsilon_0\Omega'_{\mathrm{x}}-\varepsilon_3\Omega'_{\mathrm{y}}+\varepsilon_2\Omega'_{\mathrm{z}}\\ \varepsilon_3\Omega'_{\mathrm{x}}+\varepsilon_0\Omega'_{\mathrm{y}}-\varepsilon_1\Omega'_{\mathrm{z}}\\ -\varepsilon_2\Omega'_{\mathrm{x}}+\varepsilon_1\Omega'_{\mathrm{y}}+\varepsilon_0\Omega'_{\mathrm{z}}\end{bmatrix}, \tag{B.12}$$

$$\frac{\mathrm{d}}{\mathrm{d}t_{\mathrm{dyn}}}\begin{bmatrix}\Omega'_{\mathrm{x}}\\ \Omega'_{\mathrm{y}}\\ \Omega'_{\mathrm{z}}\end{bmatrix}=\begin{bmatrix}[(J'_{\mathrm{y}}-J'_{\mathrm{z}})\Omega'_{\mathrm{y}}\Omega'_{\mathrm{z}}+N'_{\mathrm{x}}]/J'_{\mathrm{x}}\\ [(J'_{\mathrm{z}}-J'_{\mathrm{x}})\Omega'_{\mathrm{z}}\Omega'_{\mathrm{x}}+N'_{\mathrm{y}}]/J'_{\mathrm{y}}\\ [(J'_{\mathrm{x}}-J'_{\mathrm{y}})\Omega'_{\mathrm{x}}\Omega'_{\mathrm{y}}+N'_{\mathrm{z}}]/J'_{\mathrm{z}}\end{bmatrix} \tag{B.13}$$

for rotational motion.

The common fourth-order Runge-Kutta scheme is used for temporal integration. No iteration between CFD and sRBD solvers was employed, because the time step in the dynamics solver $\mathrm{d}t_{\mathrm{dyn}}$ is very small compared to the time step $\mathrm{d}t$ in the fluid solver (more than ten times smaller).

For flow field computation, flier grids in the inertial frame are necessary. For this purpose, a transformation matrix using unit quaternions $\underset{\mathrm{b}\to\mathrm{g}}{\mathbf{C}}$ is used. Let the position of a grid point in the body frame and in the inertial frame be $\mathbf{R}'_{\mathrm{grid}}$ and $\mathbf{R}_{\mathrm{grid}}$, respectively. Then,

$$\mathbf{R}_{\mathrm{grid}}=\underset{\mathrm{b}\to\mathrm{g}}{\mathbf{C}}\,\mathbf{R}'_{\mathrm{grid}}+\mathbf{R} \tag{B.14}$$

where

$$\underset{\mathrm{b}\to\mathrm{g}}{\mathbf{C}}=\begin{bmatrix}\varepsilon_0^2+\varepsilon_1^2-\varepsilon_1^2-\varepsilon_3^2 & 2(\varepsilon_1\varepsilon_2-\varepsilon_3\varepsilon_0) & 2(\varepsilon_1\varepsilon_2-\varepsilon_3\varepsilon_0)\\ 2(\varepsilon_1\varepsilon_2+\varepsilon_3\varepsilon_0) & \varepsilon_0^2-\varepsilon_1^2+\varepsilon_1^2-\varepsilon_3^2 & 2(\varepsilon_2\varepsilon_3-\varepsilon_1\varepsilon_0)\\ 2(\varepsilon_1\varepsilon_3-\varepsilon_2\varepsilon_0) & 2(\varepsilon_2\varepsilon_3+\varepsilon_1\varepsilon_0) & \varepsilon_0^2-\varepsilon_1^2-\varepsilon_1^2+\varepsilon_3^2\end{bmatrix}. \tag{B.15}$$

Further details can be found in Maeda et al., 2010.

References

Maeda, M., Gao, N., Nishihashi, N. and Liu, H. (2010), ‘A Free-Flight Simulation of Insect Flapping Flight’, *J. Aero Aqua Bio-mechanisms* **1**(1), 71–79.